Master's thesis

NTNU
Norwegian University of Science and Technology
Faculty of Information Technology and Electrical Engineering
Department of Electric Power Engineering

Egil Viken

Towards Energy Management of an MMC With PV and BESS

Design, Control and Operation Under Power Mismatches

Master's thesis in Energy and Environmental Engineering
Supervisor: Gilbert Bergna-Diaz
June 2020

NTNU
Norwegian University of
Science and Technology

Egil Viken

Towards Energy Management of an MMC With PV and BESS

Design, Control and Operation Under Power Mismatches

Master's thesis in Energy and Environmental Engineering
Supervisor: Gilbert Bergna-Diaz
June 2020

Norwegian University of Science and Technology
Faculty of Information Technology and Electrical Engineering
Department of Electric Power Engineering

NTNU
Norwegian University of
Science and Technology

Preface

This thesis is the final requirement for acquiring a M.Sc at the Norwegian University of Science and Technology (NTNU) and marks the end of the 5-years M.Sc programme Energy and Environmental Engineering. It is a research project conducted for the Department of Electrical Power Engineering, NTNU, Trondheim, with Associate Professor Gilbert Bergna-Diaz as main supervisor and Dr. Raymundo E. Torres-Olguin as co-supervisor. The research is the result of the work done in two separate semesters from August 2019 to June 2020. In the first semester a specialization project was done to learn the necessary prerequisites for the thesis while in the second semester the research as presented in this thesis was completed. The specialization project resulted in a report [1].

The thesis is part of the project PVBESS developed by "The Norwegian Programme for Research Cooperation with India" abbreviated INDNOR. The Indian government has set a goal to increase its solar energy generation with 100 GW installed power by the year 2022. To facilitate this installation, countries like Norway can be of help by giving financial advice, provide services and contribute to the operation of the solar power plants. PVBESS is a 3-year bilateral project between SINTEF Energy and NTNU on the Norwegian side, and Indian Institute of Technology (IIT) on the Indian side. This project is funded by the Research Council of Norway. There are also two industrial partners in Norway that are involved: Equinor and Saga Energy. This project focuses on the implementation of a modular multilevel converter (MMC) for integration of large scale PV together with battery energy storage systems (BESS). The ambition is that the inherent features of the MMC and proper power sharing and voltage balancing with the BESS will lower the initial capital investments and operation costs compared to traditional solutions.

Acknowledgement

First of all, I want to thank my supervisors for guiding me through this thesis and the end chapter of my academic studies. I will like to thank main supervisor Gilbert Bergna-Diaz for his expertise on modular multilevel converters, a topic that seems to never leave you and probably never will. I also appreciate how elegantly you was able to explain methods and topics, never skimming the surface, but striving to provide a deeper understanding and intuition. However, what I appreciate the most was the time you put down to convey it often adding humorous remarks. Furthermore, I would like to thank my co-supervisor Raymundo E. Torres-Olguin for both his organizational and supporting abilities. Thanks for always being accessible and ready to help despite this spring's circumstances. Thanks for somehow always managing to mention new ideas that would get me out of the rut. Specifically, I will like to thank you for being a good listener and the time spent on helping me create a well-structured thesis.

I will also like to thank the people closest to me. Thanks to all my friends for reminding me on all the transient time-variant things that generates power to my life in completely different ways. I will also like to thank my family for the constant support during my studies and in particular for the warm embrace I got when I was forced to come home like the prodigal son during the Corona-virus outbreak. I think more than one fatted calf was slain, but then again I do not think that is more than we usually eat. And to my older brother, which of course bore no hard feelings because he never does, bringing only laughter and a great selection of beer every Friday evening. Last, but not least, thanks to my girlfriend for encouraging me all the numerous times I hit the wall (otherwise known as "mastersmeller") and for being the only true power couple.

June 2020, Trondheim Egil Viken

Abstract

Spatially distributed, decentralized small power units, often known as distributed energy resources (DERs), are getting more and more connected to the grid. This is mostly driven by the need for greener energy, flexible grids and an increased interest for microgrids. The intrinsic behavior of the DERs, however, makes them negatively impact the grid and thus new ways to interface them are constantly investigated.

Two popular DERs are PV arrays and battery storages. PV arrays are one of the fastest growing DERs and the PV plants are getting increasingly larger due to economics of scale. This requires a larger sized interface which is both costly and demanding for the interfacing converters. Additionally, larger plants struggle to extract the maximum available power since they are controlled by centralized maximum power point trackers (MPPT). The size also accentuate the impact of the PV intermittency which creates a need for stabilizing resources. One popular resource is the battery energy storage system (BESS), but also this resource must be properly grid-connected.

A new, promising grid interface for DERs is the modular, multilevel converter (MMC). This converter can connect PV arrays in each of the submodules which enables individualized MPPTs for each PV array. Moreover, the MMC can without transformers create medium-high voltages and has an outstanding ability to control internal power flows. The control features are important to handle any power mismatches that can occur between the submodules. For example, the PV arrays can receive different amounts of irradiances which makes the submodule produce unequal amounts of power.

Extensive research is conducted on how the MMC can internally handle the power mismatches. Several techniques for mitigating the imbalances have been found that use components in the internal circulating current or use the BESSs to compensate the power differences. The BESSs can simultaneously be used for grid ancillary services as well. However, adding DERs that can act as loads can create mixed power flows in the MMC, that is, there can exist both positive and negative submodules power flows in the MMC. The mixed power flows can be hard to control internally. In fact, these mixed conditions is not yet documented or analyzed in the literature.

The contribution of this thesis is to make the first effort towards a general energy management system (EMS) for DERs such as PV arrays and BESSs by describing and analyzing the mixed power flows in a grid-connected MMC. An MMC model with the existing and most effective power mismatch compensation techniques from the literature is used to interface the DERs. The PV array and BESS are controlled in a submodule designed specifically for interfacing the DERs. Scenarios with different power mismatches are simulated to evaluate the MMC performance using key performance indicators and to identify converter deficiencies. Recommended guidelines for energy management systems are drawn based on the result of the simulations. Mixed power flows between the submodules of an arm are in general found to be disadvantageous and should be avoided.

Sammendrag

Antallet mindre, desentraliserte kraft enheter i fordelingsnettet, bedre kjent som distribuerte energi ressurser (DER), vokser kraftig. Grunnene for veksten skyldes et behov for grønnere energi, fleksibilitet i nettet og en økt interesse for mikronett. De iboende egenskapene i DERer, derimot, kan ha mange negative konsekvenser for nettet og derfor forskes det stadig på nye måter å koble dem til nettet på som kan redusere de negative påvirkningene.

To populære DERer er solceller og batterilagre. Solceller er en av de raskest voksende DERene i verden og solcelleanlegg blir stadig større på grunn av stordriftsfordeler. Dette krever en større dimensjonering av nettilkoblingen til solcelleanleggene som både kan være kostbart og krevende for omformerne i tilknytningspunktet. I tillegg sliter store solcelleanlegg med å hente all den tilgjengelige kraften siden desentraliserte sporingsmetoder for maksimal effektproduksjon (MPPT) krever mye kraftelektronikk. Anleggets størrelse øker også påvirkningen av solcellenes varierende kraftproduksjon noe som øker behovet for stabiliserende kilder. En mye brukt stabiliserende kilde er batterilagringssystemer (BESS), men også de må kobles til nettet på en hensiktsmessig måte.

En ny og lovende teknologi for nettilknytning av DERer er den modulære multinivå omformeren (MMC). Denne omformeren kan koble til solcellepanelene via hver av modulene i MMCen. Dette gjør at tilpassede MPPTer kan bli gitt for hver av solcellepanelene. Dessuten, MMCen kan enkelt lage høye spenninger uten transformatorer og har en fremragende egenskap til å kontrollere indre effektstrømmer. Kontrollegenskapene er viktige for å håndtere effektforskjeller som kan oppstå i omformeren. For eksempel kan solcellepanelene i to forskjellige moduler produserer ulike effekter på grunn av forskjelling solinnstråling på panelene.

Det er mye forsket på hvordan MMCen kan håndtere effektforskjellene internt. Flere måter for å redusere forskjellene er funnet. De mest effektive bruker komponenter i den sirkulerende strømmen i MMCen eller de installerer BESSer som kan ta eller gi effekt for å minimere effektforskjellene. BESSene kan også brukes til tjenester for nettet som å balansere nettet gjennom spenningsregulerende eller effektytende tjenester. Derimot, siden DERer som BESSene kan fungere som laster, kan det oppstå blandet effektstømmer i MMCen som kan være vanskelige å balansere. Disse blandede effektstrømmene hvor noen moduler gir effekt, mens andre tar effekt, har enda ikke blitt dokumentert eller analysert.

Denne masteroppgaven bidrar med å legge grunnlaget for et generelt energistyringsystem for DERer slik som solceller og BESSs ved å beskrive og analysere en blandet effektflyt i en nettilkoblet MMC. En MMC-model med de eksisterende minimeringsteknikkene for effektforskjeller i MMCer er brukt for koble solcellene og batteriene til nettet. Solcellene og batteriene er kontrollert av kraftelektronikk i modulene. Scenarier med ulike effektforkjeller er simulert for å vurdere MMCens ytelse ved bruk av definerte ytelsesfaktorer og for å identifisere opphavet til eventuelle uønskede egenskaper. Generelle betraktninger for eneristyringssystemer med disse DERene er så formulert basert på resultatet i simuleringene. Generelt er blandede effektstrømmer dårlige for ytelsen av MMCen og bør unngås.

Contents

List of Figures

List of Tables

Chapter 1

Introduction

The purpose of this chapter is to provide a motivation for the thesis, describe its goal and objectives, limit the scope of the research, highlight the thesis' contributions and outline its contents.

1.1 Motivation

1.1.1 The Green Transition

The principles for connecting energy resources to the grid are changing drastically with the transition to the modern power grid. Traditionally, the main power sources in the grid have been large, centralized generation units. The conventional generation units, based on synchronous generators, are all synchronized at the same frequency and are characterized by a high inertia which assist the frequency deviations when the power balance between the generation and consumption changes in the grid. In other words, the conventional power generation helps stabilize the grid. Since the centralized generation units use a very mature technology, integration of these units to the grid is also well-documented.

However, the energy resources for most of the conventional generation units are petroleum-based and with the global aims of reducing emissions of greenhouse gases and providing future energy security by minimizing dependency on storage resources, more renewable energy has been connected to the grid. These energy resources fall under the category distributed energy resources (DERs) since the energy they provide is harvested from several small, spatially distributed resources. Connecting DERs to the grid, however, poses a new set of problems due to their intrinsic characteristics: they (I) are scattered spatially, (II) have an intermittent behavior and (III) a low inertia, and (IV) produces maximum power at frequencies different from the grid frequency or at varying frequencies. This means that the conventional centralized approach cannot be used, that the grid is more prone to stability issues and that more power electronic interfaces are necessary.

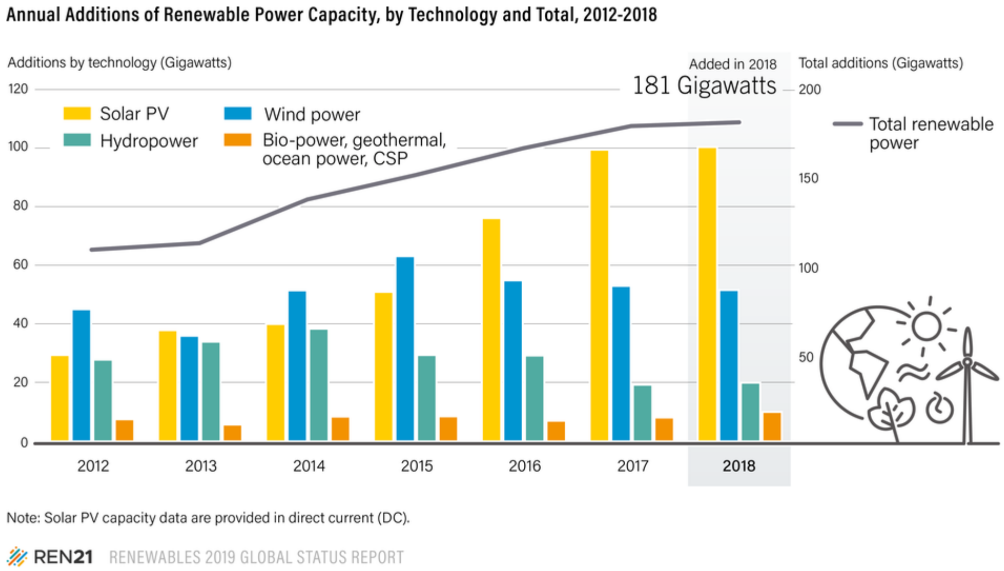

Figure 1.1: Annual additions of power capacity for different renewable energy resources [2]

One of the fastest growing DERs is the solar PV. The energy resource has been popular because its energy is accessible almost everywhere, the price per PV panel has steadily decreased and it has arguably a little visual impact on the environments. The popularity of PV generation is demonstrated by the steady increase in installed capacity as seen in Figure 1.1. The figure shows that PV plants comprised the majority of the additional installation of renewable energy resources in 2018 by being 55 % of the new installed renewable capacity. It has also been the fastest growing DER for 3 years in a row [2].

The increased penetration of PV generation leads to more notable PV-specific phenomena in the grid, for example, producing what is known as duck curves for highly PV-integrated grids as shown in Figure 1.2. The figure shows the demand, the PV generation and the net demand on a specific day in 2016, California, which is known for its high penetration of PV power. The net demand is the sum of the demand and DER generation and it is seen to resembles a duck shaped graph. This is because of high PV generation during the afternoon that subsequently reduces in the evening when the residential loads increases. This leads to high ramping in the net demand that causes frequency variations in the grid.

An essential part of the integration of PV arrays is, therefore, to install resources that can compensate the power variations. Such a technology could be the battery energy storage systems (BESS) which also is a type of DER. By charging and discharging the BESS during periods of high and low PV generation respectively, the BESS is peak-shaving the net demand and reducing the fluctuations. The load-leveling reduces the necessary amount of installed capacity as well as the need for expensive, fast acting generation units is reduced.

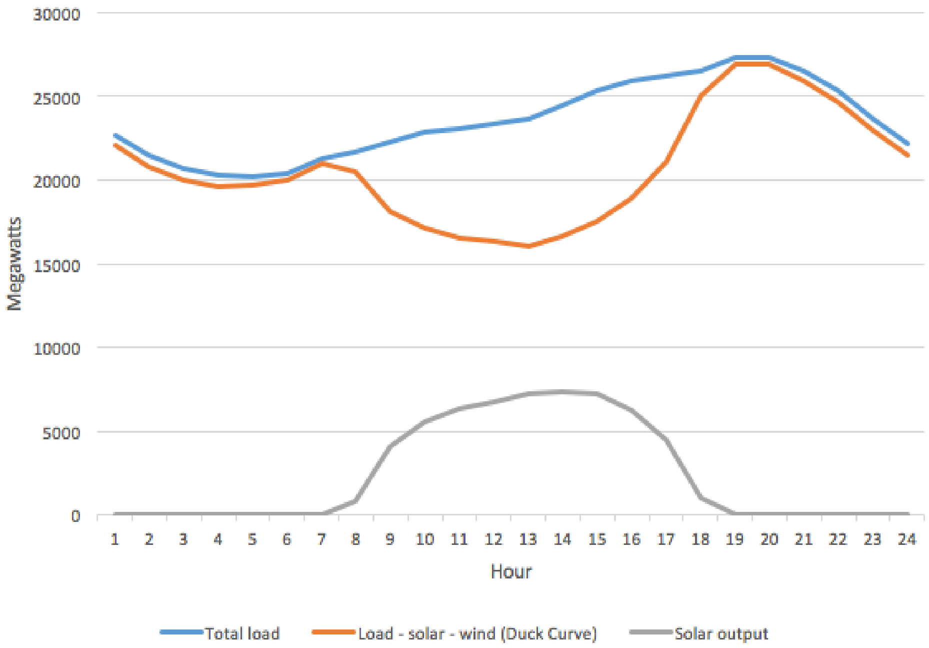

Figure 1.2: The demand, PV generation and net demand (duck curve) of the Californian grid during October 22, 2016 [3]

1.1.2 Issues With Grid-Connected PV Power

Commercial PV plants must be grid-connected through a power electronic interface. To make solar PV competitive with other energy resources, the cost of every kilowatt generated from the PV plant must be reduced. An integral part of this reduction comes from having converters that are cheap, reliable and efficient. Furthermore, to make sure that the PV arrays produce the maximum power possible, they must provide maximum power point tracking (MPPT) for the panels. However, only one MPPT can be set by each converter.

PV plants can be grid-connected through either a centralized converter interface or a distributed converter interface. Common for both types is that they have to convert DC current coming from the PV panels into AC for the grid. However, the converter types differ based on the number of conversion stages used in this process. Different types of converter interfaces are shown in Figure 1.3. If all the PV panels first are connected and then converted from DC to AC in only one converter, the converter interface is centralized as in interface A. In contrast, sometimes the PV panels are connected into separate strings which are individually connected to a common DC-bus before the common DC source is converted to AC. The conversion is then done in multiple steps and since the conversion steps can be scattered spatially these converter interfaces are called distributed. The most common distributed converter interface is the multi-string interface shown in interface B in Figure 1.3.

Traditionally, the most used converter has been the centralized converter because of its

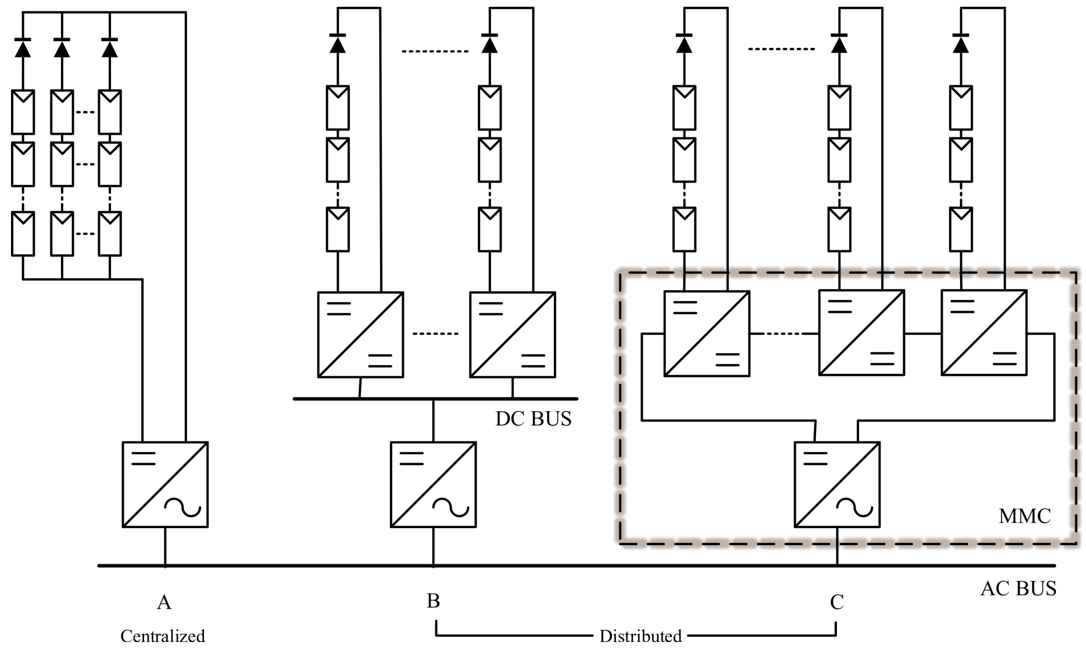

Figure 1.3: Centralized and decentralized converter interfaces for PV power.

simplicity and low prices. The centralized converters are also more efficient because they have fewer conversion stages. On the other hand, they produce more harmonic content, the design is not flexible and they harvest less energy than the distributed converters [4]. Reduced harvesting comes as a consequence of the converter control capability which normally is able to maintain only one MPPT. Therefore, if there are different conditions for the PV panels such as if there are local shades or old, degraded panels, the centralized converter is unable to adjust to the panels' individual MPPT. In comparison, the distributed converter is more granular as indivual MPPTs for each array can be provided, leading to higher energy harvesting.

One emerging issue is that PV plants is constantly increasing in size due to economics of scale. This increases the total power production and makes medium-voltage grid-connection the most preferred option. However, the voltages produced by the PV plants typically goes up to only 1000 V for safety reasons. Therefore, the voltage produced must be amplified by the converter interface. The amplification, however, is not straightforward for the traditional two-level converters [5] because of: (I) the low standard rating for semi-conducting materials lying between 0.6-3.3 kV, (II) increased losses and complexity in series connected semiconductors and (III) high frequency switching losses.

Thus, there is a need for alternative interfaces that can handle both multiple MPPTs and voltage amplification to medium-high voltages. A simple alternative is to use the multi-string interface with a large line-frequency transformer to amplify the voltage after the converters, but this increases the volume and weight of the plant [6]. Systems for creating medium-high DC voltages exist [7], but quickly becomes complex and hard to control. A promising solution seems to use a transformer-less multilevel converter as illustrated in interface C. This converter can series connect PV-interfacing submodules to synthesize AC medium-high voltages and each voltage level can be adjusted to fit individual MPPTs.

The biggest issue of grid-connected DERs using multilevel converters is to handle unbalanced power generation within the converter. Different irradiances and temperatures between the string-connected submodules may cause uneven production of power. The multilevel converter must therefore be able to internally distribute the generated power to produce a balanced grid current. Moreover, this balancing must be done without affecting the grid performance. Due to these control challenges the most suitable multilevel converter may be the modular multilevel converter (MMC) because of its superior capability to control internal power flows. It is also shown to have the best efficiency for higher medium-high voltages (≥13.8kV) compared to the much used cascaded H-bridge converter [8].

One possible method to connect the PV strings is to directly connect them to the capacitors of the submodules [9, 10]. By using a balancing algorithm in the MMC to properly insert the capacitors, they can be charged to the necessary voltages for MPPT. The benefit of direct connection is that less semiconductors are needed which reduces losses and control complexity. However, it comes at the cost of less controllability. Since uneven irradiance will demand different maximum power points (MPPs), the total arm voltages will become unequal. This can be compensated by a redundant submodule as in [9] that can alleviate the missing voltage, but this increases the amount of components in the MMC without adding more power to the grid.

A more common approach is to connect the PV strings using interfacing converters. The interfacing converters can be used to set the MPPT so that the submodule capacitors can remain fixed. This makes the converter design easier. The connection of several PV systems has been implemented using interfacing converters [11–13], but how they manage the uneven generation differ between them. Reference [11] adjusts the phase voltage to provide a balanced grid-power, but the range of the adjustment is limited and does not work for large imbalances. A very effective method using circulating currents to counter the imbalances is proposed in [12] and is also used in [13]. The methods developed makes the MMC very capable of handling power imbalances due to uneven PV generation.

1.1.3 MMC As Interface For DERs

Additional functionality can be implemented by connecting energy storage systems such as BESSs together with the PV arrays. The BESSs can either be connected in separate submodules or in a hybrid submodule system with the PV strings. The BESS can contribute either by ancillary services to the grid or by aiding the converter operation. Reference [14] uses a hybrid submodule to provide peak-shaving of the generated PV power. Reference [15], on the other hand, uses dedicated BESS submodules to minimize the power mismatch between the MMC arms. This reduced the necessary balancing circulating currents and gave a higher converter efficiency.

The BESS power commands in [13, 14] are controlled by a properly designed energy management system (EMS). Common for both the EMSs used, however, is that they rely on a smoothly distributed power generation. This is not guaranteed when storage technologies are introduced since the power in a submodule might be consumed rather than generated when the BESS inevitably must be charged. Reference [16] addresses this issue for a distributed MMC infrastructure for charging of electric vehicles. They show that by injecting second harmonic injections into the circulating current, an arbitrarily number of submodules can be fully loaded without causing converter instabilities. The paper, however, does only focus on submodules having the same power direction, that is mixed power flows where there are charging submodules and discharging submodules simultaneously in the MMC were not investigated. Consequently, there does not exist any studies on a general MMC EMS for grid-connected DERs with mixed power flows.

1.2 Goal and Objectives

This thesis is the first step towards a general EMS for grid-connected DERs. Its goal is to analyze the MMC's ability to grid-connect DERs through submodules with power mismatches and mixed power flows. In short, this is referred to in this thesis as an analysis of the connectivity of the DERs in the MMC. Three main objectives must be reached to fulfill the goal:

- Create an MMC model and provide an MMC analysis.
- Create a submodule to interface a PV array and a BESS.
- Create scenarios for the submodule and MMC model.

The chapters 2, 3 and 4 are dedicated to each of these objectives respectively. The criteria for the objectives are specified in the following.

The MMC model must be able to represent the converter during internal power mismatches. This requires a complete state-space representation of the converter dynamics and a close description of the submodule balancing algorithm. The frequency components of the converter variables should be elaborated upon for a deeper analytical insight. This makes it easier to describe the necessary actions to compensate the power mismatches and the subsequent consequences for the internal states of the converter.

The submodule topology must be properly designed, modeled and sized since PV arrays and BESSs can be interfaced in many ways. A general topology of an MMC submodule with these elements are showed in Figure 1.4. The figure shows a circuit with full controllability, that is, converters interconnecting both DERs. These converters must provide galvanic isolation, set the MPPT for the PV array, stabilize the common DC voltage and control the battery power flow. However, it must be investigated if a simpler submodule circuit with fewer converters can provide the same tasks. If so, the converters must be properly modeled and sized. Models describing the behavior of the DERs must also be provided.

The scenarios must both verify the behavior of the MMC and find the operating limits for the internal power mismatches. This is achieved if the different mismatch types are individually treated and analyzed. The scenarios should constantly increase the complexity and demand for the MMC balancing to locate the operating limits using the existing imbalance compensation techniques.

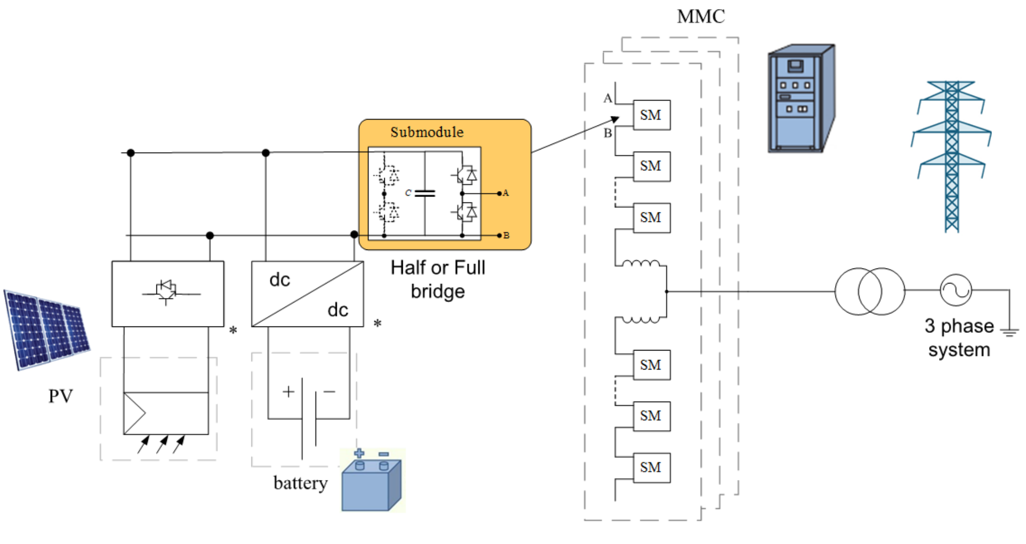

*interface has to be developed during the project

Figure 1.4: A general topology for interfacing a PV and BESS in an MMC submodule.

1.3 Scope

Assumptions are made to limit the complexity and to stay relevant to the topic:

- Only the already existing MMC compensation techniques for power mismatches are considered.
- The second harmonic injections for submodule balancing are manually injected without attention to the optimal injection magnitude and phase.
- The submodule model does only consider the slow dynamics of the submodule. This means that switching actions and transient events in the DERs are neglected.
- All system information is considered available and globally accessible. Specifically, the state of charge in the batteries are considered to be known accurately and operating procedures to estimate them are overlooked.
- All temperature effects on the DERs are neglected.

1.4 Contributions

The main contributions of this thesis are highlighted below:

- A complete description of an interface for grid-connected PV arrays and BESSs using an MMC.
- An analysis of an MMC for all possible power mismatch scenarios.
- The identification of the operating limits for a grid-connected MMC using the existing power mismatch compensation techniques.
- The description of a general MMC EMS for grid-connected PV arrays and BESSs.
- A design of a submodule circuit for control of PV and BESS power flows.
- The formulation of steady-state time-invariant solutions for a single-phase dual active bridge converter using DQZ transformation and a virtual phase.
- A simpler derivation of the harmonic distribution in the Σ-Δ MMC variables.

1.5 Structure of the Thesis

The thesis is divided into five chapters. Chapter 1 has focused on giving the proper motivation for the thesis and an introduction to the topic. It has also set the goal, limited the scope and highlighted the main contributions.

Chapter 2 is about the modeling of an MMC and its operation during power mismatches. The chapter covers the fundamentals of the MMC and describes the submodule balancing algorithm. An arm averaged state-space representation of the MMC is developed which is converted into the more popular Σ-Δ notation. Several analytical tools are described that illustrate the properties of the Σ-Δ notation. The power mismatch types are introduced and the existing compensation methods for mitigating them are described. Finally, a base model of an MMC for treating unbalanced power generation is presented and verified through simulations.

The MMC submodule is designed, modeled and sized in Chapter 3. First, the desired structure of the submodule circuit is outlined. Then each circuit element in the submodule is independently modeled: the PV array, the BESS and the converters. The DERs are modeled to only include the slow dynamics and the converters are represented by their steady-state time-invariant representations. The circuit control is then derived consisting of a perturb and observe MPPT for the PV arrays and a simple power control loop with saturation limits for the BESS. Finally, all the components of the submodule is sized to the rated submodule power.

The connectivity of the DERs is investigated in Chapter 4 using several power mismatch scenarios. First, a general EMS for PV and BESSs is described and some specific EMS examples are provided. Then the connectivity is evaluated in the system level by simulating the MMC and using power references to represent the submodules. The submodules power flows are set to the rated values to limit-test the connectivity. Rated power flows are also simulated in the submodule model to investigate the consequences of delivering rated power flows. The MMC performance is assessed with key performance indicators and the MMC operation for each power mismatch case is analyzed.

The last chapter, Chapter 5, ends the thesis. First, the main conclusions of the thesis are summarized. Then possible future extensions are presented. It is proposed to research more on the submodule balancing to provide better guidelines for mixed power flows. It is also proposed to developed a steady-state MMC model which can be more suited for MMC energy management analysis.

Chapter 2

The Modular Multilevel Converter

This chapter gives a description of the MMC converter and a model for analyzing power mismatches. Initially, the MMC topology is described and basic functionality is introduced. Then a state-space representation of the converter is derived using an averaged arm model. This representation is converted to the more convenient Σ-Δ notation and useful analytical insights are developed. Finally, the MMC's compensation methods for internal power mismatches are derived and a simulation of the MMC converter is done to verify the compensation controller.

2.1 Introduction

The modular multilevel converter (MMC) is an emerging converter known for its modularity, low THD and high efficiency. The superior performance of the MMC comes from its topology which consists of distinguishable submodules that can be connected in series. The number of submodules, each providing a certain voltage step, are kept high to provide multiple voltage levels for the MMC output. As a consequence, a high resolution output voltage can be created with a low harmonic content and reduced need for filtering. Furthermore, the partitioning of the output voltage into smaller steps allows for submodule components with much lower ratings and higher efficiencies. Consequently, the MMC is easily scaled for high power applications without increasing complexity.

The MMC was originally presented in 2003 [17] and has since then gained a lot of interest in the scientific community. Due to its scalability it was originally proposed, and later also the preferred choice, for high voltage direct-current applications (HVDC). However, it has since been proven viable for many other applications [18] such as in variable-speed drives, flexible AC transmission systems (FACTS) and for connecting distributed energy resources (DERs) to the grid. It is in the last of these applications that the MMC can utilize its unique modularity for independent control of the DERs and simple scalability for producing medium-high voltages. Specifically, DERs such as PV arrays can harvest the maximum available power through locally adapted MPPTs for each submodule.

The complexity of grid-connected DERs in MMCs lies in the control. When DERs are given individual maximum power points, power can be produced unevenly within the MMC. Depending on the imbalances created, different balancing currents are needed to prevent unstable converter voltages. At the same time, these currents should not affect the grid. Moreover, they should be minimized to preserve a high converter efficiency.

The goal of this chapter is to model an MMC and look at how the unbalanced power generation can be handled within the converter. First, the fundamentals of the MMC converter is presented and specific details for grid-connected MMCs without DC links are introduced. Secondly, different modeling approaches for the MMC are mentioned before a derivation using average arm modeling is done to make an averaged dynamic state-space representation. Next, this representation is converted into the more convenient Σ-Δ representation and practical analytical tools for the Σ-Δ representation is derived. The tools are to provide a deeper understanding of the MMC operation which are necessary for understanding the compensation techniques for power mismatches that are presented at the end of the chapter. Finally, an MMC simulation model using these techniques are presented and the compensation controller is verified through simulations.

2.2 Fundamentals of the MMC

2.2.1 General MMC Topology

The structure of the most common and general three-phase MMC, known as the double-star-configured MMC [19], but hereby referred to as the MMC, consists of three parallel phases between a common DC and AC link as seen in Figure 2.1. The components of each phase, referred to as a leg, is divided into two similar branches called arms. Each arm consists of N series connected submodules together with an arm resistance R (not shown in Figure 2.1) and inductance L. Each phase is then connected to a filter with a filter inductance L_f for removing unwanted harmonics.

The content of each submodule can be designed independently. In HVDC applications, a submodule most often consists only of a half-bridge and a capacitor. Sometimes the half-bridge is replaced by a full-bridge, but the submodules are empty otherwise. However, adding more components in parallel with the capacitor is possible as long as the power generation or consumption of the new components are taken care of. How the submodule is designed and how it handles these power flows is described in the next chapter. The interface of the submodules, the half-bridge, is fairly common for all applications and serves the function of either inserting or bypassing the submodule. This basic submodule operation is described below.

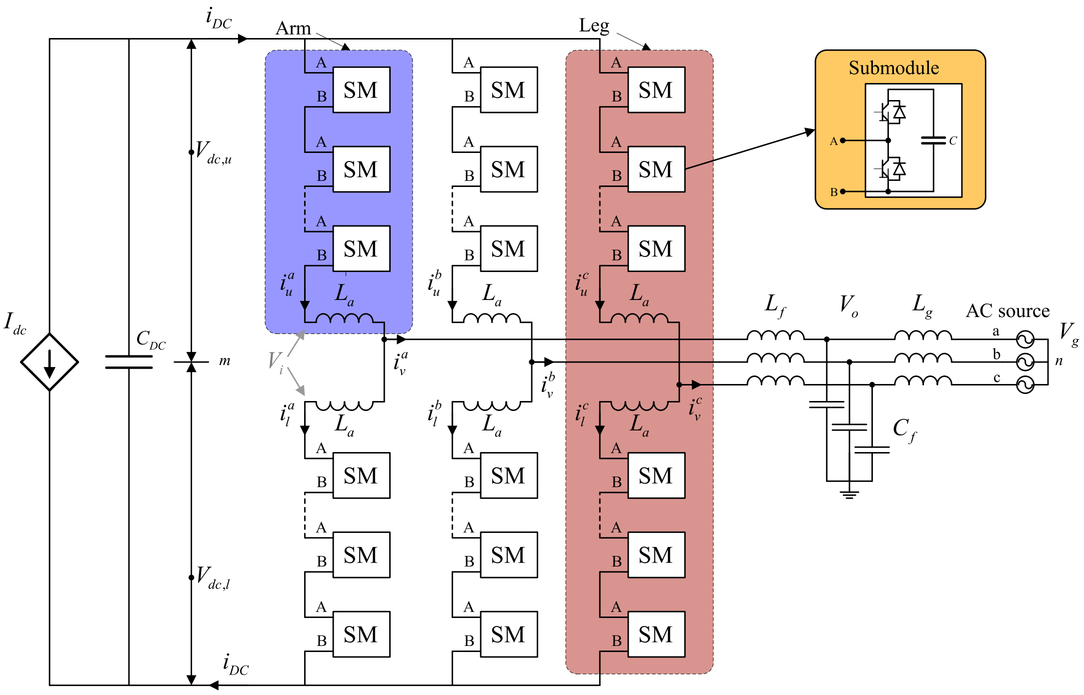

Figure 2.1: Topology of an MMC.

2.2.2 Basic Submodule Operation

The submodule can be inserted or bypassed with the half-bridge as seen in Figure 2.2. The half-bridge, shown in Figure 2.2a, consists of two switches Q1 and Q2 and an anti-parallel diode D1 and D2 respectively. If Q1 is turned on while Q2 is kept off, the current will go as indicated with the orange lines in Figure 2.2b. The current going into the submodule goes through the capacitor and the submodule is referred to as inserted. The orange lines apply for both when $i_{arm} > 0$ and when $i_{arm} < 0$ indicating that the capacitor can be both charged and discharged. On the other hand, turning Q2 on while keeping Q1 off results in the current flow of the orange lines in Figure 2.2c. The current into the submodule does not go through the capacitor irrespective of the current direction and hence this mode is referred to as bypassed. Together these modes form the basis of regulating the capacitor voltages of the submodules.

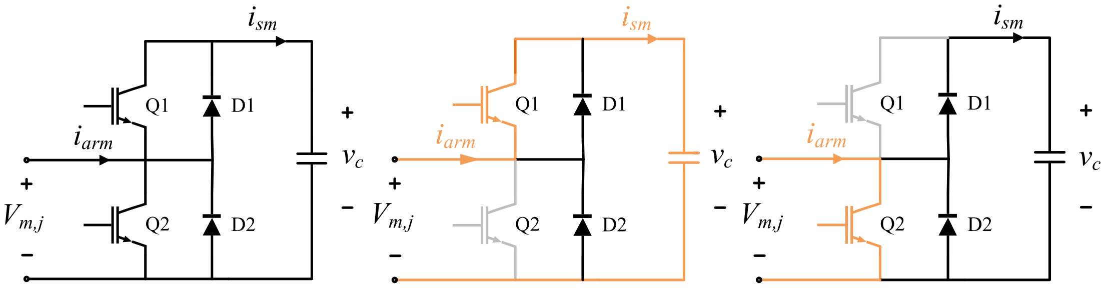

(a) Submodule interface (b) Inserted (c) Bypassed

Figure 2.2: Topology of a half-bridge submodule and the possible submodule modes.

2.2.3 Submodule Capacitor Voltage Balancing

As the submodules are inserted or bypassed in the operation of the MMC, the capacitor voltage of each submodule will change accordingly. If these voltages are not controlled the total arm voltages will differ from each other causing unbalanced grid currents and, eventually, instabilities in the converter. An algorithm for controlling the submodule capacitor voltages is therefore necessary.

The most basic balancing algorithm, as presented in the original paper about MMC [17], creates equal submodule voltages by prioritizing the submodules with the largest deviances from the reference voltage. This is achieved by making a sorted list of all the submodule voltages every instant the inserted submodules are to be determined. If the current i_{arm}, as indicated in Figure 2.2, is positive, inserted submodules will be charged. For a positive i_{arm} the submodules with the lowest voltage in the list are be inserted. Conversely, if i_{arm} is negative, the submodules with the highest capacitor voltages are inserted so that these capacitors are discharged.

In most cases the capacitor voltage balancing algorithm is assumed ideal. This is justified by having a very fast balancing algorithm so that the capacitor voltages can be assumed equal at the time scale of the MMC dynamics. The drawbacks of the fast algorithm are high switching losses and a high computational load. There exist more advanced methods to insert the submodules that provide lower switching frequencies by accepting higher deviances between the submodule voltages. For example, in [20], reduced switching is accomplished by only adding to or removing from the already inserted submodules to acquire the desired number of inserted submodules. That is, if N_{new} is the new number of submodules to be inserted and N_{old} was the old number, instead of inserting N_{new} new submodules every instant, only the difference in the numbers $N_{new} - N_{old}$ are inserted or removed. To reduce complexity however, an ideal balancing algorithm is assumed in the MMC modeling of this thesis.

2.2.4 MMCs for Grid-Connected DERs

MMCs with DERs connected to the MMC submodules do not need a DC link capacitor. Normally, for example in all HVDC applications, the DC link is important for transferring power from the DC side. As will be derived later, this means that the arm voltage must contain both a DC and fundamental component in phase with the grid. However, all the DERs are connected through the submodules and therefore no power needs to be provided through the DC link. Since the DC link is not needed as an interface for DC power, it can be removed to save cost. Nevertheless, the MMC must still run as if the DC link voltage was present, that is, it must produce both the DC and the fundamental component in the arm voltages. Therefore, if the upper and lower arm voltages are summed together there will still be a DC voltage in the sum. This voltage is referred to as the virtual DC voltage in this thesis.

2.3 Arm Averaged Model of the MMC

The MMC in its entirety consists of many components such as switches with highly nonlinear behaviors. For that reason, different modeling approaches exist depending on if a fast or accurate model is desired. The most accurate model, referred to as the high-fidelity model, uses detailed models for all the components and their connections. The problem with these models is that the computational load is increasing rapidly with the number of submodules.

A normal approach is to use simplified models for computationally easier simulations. A more efficient method to model the MMC is to model each switch with and ON/OFF resistance: when the switch is ON the resistance is small representing a short-circuit, and when the switch is OFF the resistance is large representing an open-circuit. However, more common is to model the MMC analytically by replacing the submodules with controlled voltage sources. A controlled voltage source can be used for every submodule or one can be used as an equivalent for the entire arm. If these sources are averaged over one period by using continuous circuit variables, the model is called an Arm Averaged Model (AAM). Because of its ease of implementation and sufficient accuracy AAM is used in this thesis.

2.3.1 Lumping Into Arm Equivalents

The arm averaged model is an MMC modeling technique which uses averaged controlled voltages sources to represent each of the MMC arms. The method is fast and has a good accuracy. However, this comes at the cost of the information that is lost by treating the submodules of each arm collectively. Instead of representing each modulated submodule voltage $v_{m,j}$ with an individual capacitor voltage $v_{c,j}$ and submodule insertion index n_j for submodule j, as in (2.1):

$$v_{m,j} = n_j v_{c,j} \tag{2.1}$$

each arm is represented with a modulated equivalent voltage v_m^k, a normalized modulation index n^k and equivalent voltage v_c^k for all the capacitors of an arm as in (2.2):

$$v_m^k = n^k v_c^k \tag{2.2}$$

In (2.2) the superscript k denotes either L or U whether the equation refers to the lower or upper arm respectively. The normalized modulation index can be a variable ranging from 0 to 1 depending on the number of inserted submodules and the number of total submodules N as in:

$$n^k = \frac{\sum_{j=1}^{N} n_j}{N} \tag{2.3}$$

The variable n^k can be assumed continuous if N is high enough. The equivalent voltage v_c^k is simply the sum of all the capacitor voltages:

$$v_c^k = \sum_{j=1}^{N} v_{c,j} \tag{2.4}$$

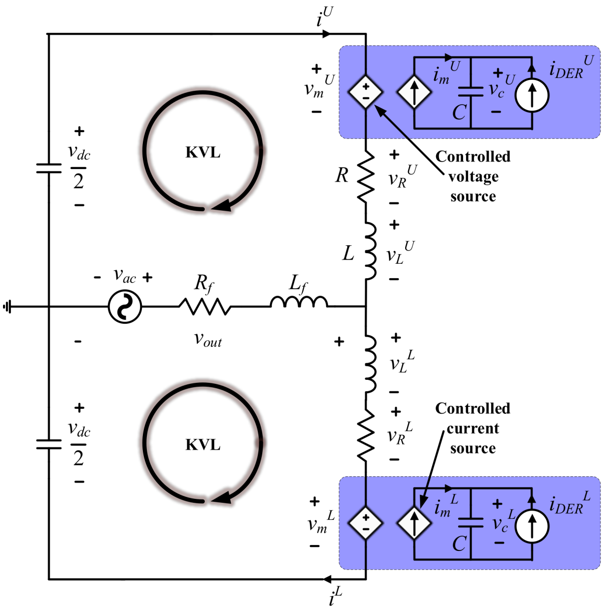

Figure 2.3: 1-phase arm averaged model of an MMC.

which make up the voltage of an equivalent capacitor C that is the series connection of all the submodule capacitors C_{sm}:

$$C = \frac{C_{sm}}{N} \tag{2.5}$$

Similarly, as with the modulated voltage v_m^k, the modulated current i_m^k through the equivalent capacitor is modulated from the arm current i^k as in:

$$i_m^k = n^k i^k \tag{2.6}$$

Finally, the currents coming from each submodule, i_{sm}, is aggregated to a common submodule current i_{DER} which represents the combined current from all submodules:

$$i_{DER}^k = \sum_{j=1}^{N} i_{sm,j} \tag{2.7}$$

The resulting equivalent circuit of the MMC for one phase is shown in Figure 2.3. Here the virtual DC link voltage have been divided in two separate capacitors to easier show the neutral of the DC side. Moreover, a filter resistance R_f has been included for the sake of completeness. Apparent from the figure, each arm can be represented as a modulated voltage source in series with the arm inductor and a modulated current source in parallel with an equivalent arm capacitor and submodule current source. By looking at the Kirchhoff's voltages laws (KVL) indicated in Figure 2.3 and neglecting the resistances, an expression for the modulation indexes of the upper and lower arms in steady-state can be obtained:

$$n^U = \frac{1}{2} - \hat{n}cos(\omega t) \tag{2.8}$$

$$n^L = \frac{1}{2} + \hat{n}cos(\omega t) \tag{2.9}$$

The modulation is seen to create a DC and a fundamental component. In (2.8) and (2.9) the only control objective of the MMC is to create a pure sinusoidal grid voltage, that is, no control terms for other purposes such as for example harmonic rejection are included. This is what is known as direct modulation. It is a type of modulation known as uncompensated modulation [21] which is when the modulation indexes are generated by using constant values for the equivalent capacitor voltages. Compensated modulation uses oscillating voltages as is the case if, for example, measured values of the capacitor voltages are used. Compensated modulation is generally more effective as it compensates the effects caused by the nonlinear product in the modulated arm voltages, but here direct modulation is used to focus on the fundamentals of the MMC operation.

A state-space representation of the converter can now be formulated based on the equivalent arm model. The rest of this section shows how this representation is obtained by looking at the dynamics of the voltage across the arm inductor and the current through the equivalent capacitor.

2.3.2 Voltage Dynamics of the Arm Inductor

The voltage dynamics of the upper and lower arm inductor of a phase are found by using the KVLs as indicated in Figure 2.3. The output voltage of the MMC is treated as a single voltage v_{out}. This makes it possible to decouple the upper and lower variables in the state equations at the cost of neglecting the dynamics of the output filter. First, for the upper loop:

$$L\frac{di^U}{dt} = \frac{v_{dc}}{2} - Ri^U - v_m^U - v_{out} \tag{2.10}$$

where v_{dc} is the virtual DC link voltage. Similarly, for the lower loop:

$$L\frac{di^L}{dt} = \frac{v_{dc}}{2} - Ri^L - v_m^L + v_{out} \tag{2.11}$$

2.3.3 Current Dynamics of the Equivalent Arm Capacitor

The current dynamics of the upper and lower equivalent capacitors are found by Kirchhoff's current law (KCL). Beginning with the upper capacitor circuit gives:

$$C\frac{dv_c^U}{dt} = n^U i^U + i_{DER}^U \tag{2.12}$$

Then for the lower capacitor circuit:

$$C\frac{dv_c^L}{dt} = n^L i^L + i_{DER}^L \tag{2.13}$$

Together (2.10)-(2.13) make up the state-space representation for the MMC.

2.4 Σ-Δ State-Space Representation

The state-space representation obtained in the previous section is not the optimal representation for MMC analysis and control. A more suited representation is the Σ-Δ notation that is introduced in this section. This is a commonly adopted notation and the one used here is based on the definitions set in [22]. The notation brings several advantages: (I) it allows for the dynamics of the filter to be included and conveniently lumped together with the arm inductors without affecting the decoupling of the Σ and Δ variables, (II) it decouples the internal and outer MMC dynamics and (III) it gives variables with fewer frequency components. The last two advantages provides one of the many analytical tools that is examined closer in the next section. The first advantage is evident from the formulation of the state-space representation in Σ-Δ notation which is derived immediately below.

The formulation starts by defining the Σ-Δ variables. These variables replace the the previous variables with the sum (Σ) and difference (Δ) of the upper and lower variables. The new variables are shown in Table 2.1. The new variables are not only convenient computationally, but gives descriptive physical interpretations as well. By examining Figure 2.3, it can be observed that i^Δ is simply the grid current while i^Σ can be interpreted as the common-mode current of the upper and lower arms. In the literature this current is known as the circulating current. To conveniently transfer (2.10)-(2.13) to Σ-Δ state-space representation the equations are manipulated as follows.

Transferred variables	Σ-variable	Δ-variable
Modulation voltages	$v_m^\Sigma = \frac{v_m^U + v_m^L}{2}$	$v_m^\Delta = \frac{-v_m^U + v_m^L}{2}$
Arm currents	$i^\Sigma = \frac{i^U + i^L}{2}$	$i^\Delta = i^U - i^L$
Submodule currents	$i_{DER}^\Sigma = \frac{i_{DER}^U + i_{DER}^L}{2}$	$i_{DER}^\Delta = i_{DER}^U - i_{DER}^L$
Capacitor voltages	$v_c^\Sigma = \frac{v_c^U + v_c^L}{2}$	$v_c^\Delta = \frac{v_c^U - v_c^L}{2}$
Modulation indexes	$n^\Sigma = n^U + n^L$	$n^\Delta = n^U - n^L$

Table 2.1: Definition of MMC variables in Σ-Δ notation.

2.4.1 Voltage Dynamics in Σ-Δ Notation

Initially, the voltage v_{out} in (2.10) and (2.11) is expanded to include the filter dynamics using the new definition of the grid current:

$$L\frac{di^U}{dt} = \frac{v_{dc}}{2} - Ri^U - v_m^U - v_{ac} - L_f\frac{di^\Delta}{dt} - R_f i^\Delta \tag{2.14}$$

$$L\frac{di^L}{dt} = \frac{v_{dc}}{2} - Ri^L - v_m^L + v_{ac} + L_f\frac{di^\Delta}{dt} + R_f i^\Delta \tag{2.15}$$

The derivation for the voltage dynamics in Σ notation are started by adding together (2.14) and (2.15):

$$L\frac{d}{dt}(i^U + i^L) = v_{dc} - R(i^U + i^L) - (v_m^U + v_m^L). \tag{2.16}$$

From (2.16) it can be observed that the Σ variables can be readily inserted giving:

$$2L\frac{di^\Sigma}{dt} = v_{dc} - 2Ri^\Sigma - 2v_m^\Sigma \tag{2.17}$$

which, divided by 2, gives:

$$L\frac{di^\Sigma}{dt} = \frac{v_{dc}}{2} - Ri^\Sigma - v_m^\Sigma \tag{2.18}$$

Similarly, Δ variables are introduced by subtracting (2.15) from (2.14):

$$L\frac{d}{dt}(i^U - i^L) = -R(i^U - i^L) - (v_m^U - v_m^L) - 2v_{ac} - 2L_f\frac{di^\Delta}{dt} - 2R_f i^\Delta \tag{2.19}$$

Again, by inserting Δ variables, the new equation becomes:

$$L\frac{di^\Delta}{dt} = -Ri^\Delta - 2v_m^\Delta - 2v_{ac} - 2L_f\frac{di^\Delta}{dt} - 2R_f i^\Delta \tag{2.20}$$

Dividing (2.20) with 2 and sorting (2.20) gives:

$$(\frac{L}{2} + L_f)\frac{di^\Delta}{dt} = -(\frac{R}{2} + R_f)i^\Delta + v_m^\Delta - v_{ac} \tag{2.21}$$

Now lumping the circuit impedances into $L_{eq} = \frac{L}{2} + L_f$ and $R_{eq} = \frac{R}{2} + R_f$ gives the Δ equation:

$$L_{eq}\frac{di^\Delta}{dt} = -R_{eq}i^\Delta + v_m^\Delta - v_{ac} \tag{2.22}$$

2.4.2 Current Dynamics in Σ-Δ Notation

The derivation for the current dynamics in Σ notation is started by adding together (2.12) and (2.13):

$$C\frac{dv_c^U}{dt} + C\frac{dv_c^L}{dt} = n^U i^U + n^L i^L + i_{DER}^U + i_{DER}^L \tag{2.23}$$

Now, based on the definitions in Table 2.1, the upper and lower arm currents can be described as:

$$i^U = i^\Sigma + \frac{i^\Delta}{2} \tag{2.24}$$

$$i^L = i^\Sigma - \frac{i^\Delta}{2} \tag{2.25}$$

Inserting (2.24) and (2.25) in (2.23) gives after some sorting:

$$C\frac{d(v_c^U + v_c^L)}{dt} = (n^U + n^L)i^\Sigma + (n^U - n^L)\frac{i^\Delta}{2} + i_{DER}^U + i_{DER}^L \tag{2.26}$$

Then using the Σ-Δ notations for the submodule current, modulation indexes and capacitor voltage sum given in Table 2.1 gives:

$$C\frac{dv_c^\Sigma}{dt} = n^\Sigma i^\Sigma + n^\Delta \frac{i^\Delta}{2} + 2i_{DER}^\Sigma \tag{2.27}$$

The derivation for the current dynamics in Δ notation is similar. Equation (2.13) is subtracted from (2.12), the upper and lower arm definitions of (2.24) and (2.25) are inserted together with the definitions of the submodule current difference, the modulation indexes and the capacitor voltage differences from Table 2.1, giving:

$$C\frac{dv_c^\Delta}{dt} = n^\Delta i^\Sigma + n^\Sigma \frac{i^\Delta}{2} + i_{DER}^\Delta \tag{2.28}$$

2.4.3 Summary of the Σ-Δ State-Space Representation

All the state-space equations in Σ-Δ notation are repeated in (2.29)-(2.32) for a better overview:

$$L\frac{di^\Sigma}{dt} = \frac{v_{dc}}{2} - Ri^\Sigma - v_m^\Sigma \tag{2.29}$$

$$L_{eq}\frac{di^\Delta}{dt} = -R_{eq}i^\Delta - v_m^\Delta - v_{ac} \tag{2.30}$$

$$C\frac{dv_c^\Sigma}{dt} = n^\Sigma i^\Sigma + n^\Delta \frac{i^\Delta}{2} + 2i_{DER}^\Sigma \tag{2.31}$$

$$C\frac{dv_c^\Delta}{dt} = n^\Delta i^\Sigma + n^\Sigma \frac{i^\Delta}{2} + i_{DER}^\Delta \tag{2.32}$$

2.5 Σ-Δ Analytical Tools

It has already been mentioned that one of the benefits of the Σ-Δ notation compared to the upper-lower notation is that the Σ-Δ variables contain fewer frequency groups. Specifically, it is reported in the literature that during normal operation of the MMC the harmonic components will be distributed in a specific way: the circular current will only contain even-ordered harmonics while the grid current will only contain odd-ordered harmonics. This fact is rigorously proven for the circulating current in [23] and indicated, due to a circular dependence, for the grid current in [24]. However, these authors spend a lot of time deriving the sizes of all the different components and therefore the analysis provided is cumbersome.

Consequently, a more intuitive derivation based on cancellations in the modulation products is outlined below that also shows the interaction of the harmonics between the circulating currents and the grid currents as reported in [25]. Insightful observations of the MMC are discovered throughout the derivation which can be used as analytical tools later in this thesis. This section is therefore both a derivation of the frequency distribution in the Σ-Δ variables as well as the unraveling of these insights: decoupled driving voltages, necessary current components, circular dependence in the arms and, in itself, frequency distribution in the Σ-Δ variables.

2.5.1 Decoupled Driving Voltages

One of the benefits of the Σ-Δ notation is that it is more convenient from a control perspective. Both the conventional upper-lower and the Σ-Δ state-space representation has decoupled differential equation, but the Σ-Δ notation has a more usable interpretation. Each arm contains current components that affects both the MMC and the grid, but the Σ and Δ currents affects them only independently. Consequently, the Σ-Δ notation decouples the inner and outer dynamics of the MMC while the upper-lower notation only decouples the arms of one leg.

In addition, the Σ-Δ notation can be used for an illustrative circuit interpretation. Equation (2.29) and (2.30) can each be interpreted using KVLs as a circuit with a voltage source which drives a current through an impedance as shown in Figure 2.4. These sources, hereby referred to as the driving voltages, are v_m^Σ and v_m^Δ and the impedances consists of the inductances, L or L_{eq}, and resistances, R or R_{eq}. The circuit representation of the inner dynamics, v_m^Σ, consists of a DC source with value $\frac{v_{dc}}{2}$ while the outer dynamics, v_m^Δ, contain a sinusoidal source with value v_{ac}. These voltages reflects the actual voltage sources in the system. These interpretations are convenient because, by KVL, the harmonic components of the currents must come from the driving voltages. In other words, the interpretation dictates that the current must have the same components as the driving voltages.

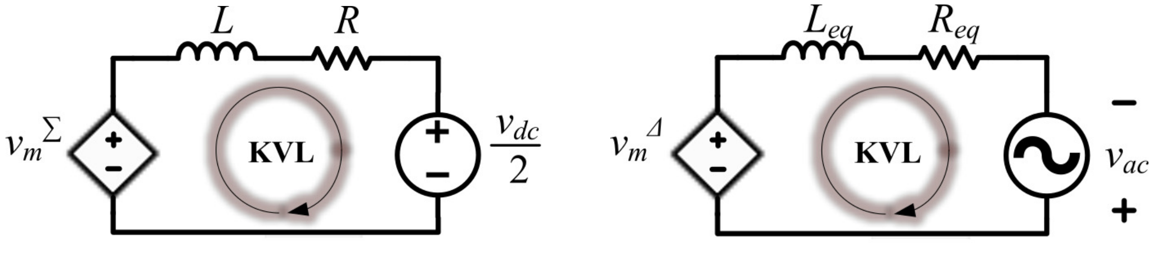

(a) Inner dynamics (b) Outer dynamics

Figure 2.4: Circuit interpretation of the inner and outer dynamics of the MMC.

2.5.2 Necessary Current Components

The arm current components can roughly be divided into two groups: the components necessary for the operation of the MMC and the harmonics that are caused as a consequence of these components. There are only two necessary harmonic components of the arm currents in an ideal, general and balanced MMC [26]: a fundamental frequency component necessary to support the output grid current and a DC component necessary for supporting power transfer between the DC and AC link. These are provided by the grid and the circulating current respectively. For MMCs without a common DC link, however, the DC component is not present. However, it is included here to make a general analysis. In the literature a significant second order harmonic is also often reported. However, this harmonic component is only one of the many harmonics that occur as a consequence of the necessary components. The reason it is mentioned is due to the significant size it has compared to the other higher-ordered harmonic components.

2.5.3 Circular Dependence In the Arms

Higher-ordered harmonics are created due to a circular dependence between the arm currents and the capacitor voltages [24, 27]. This circular dependence can be explained by beginning with the arm current. The modulation of the arm current make up the capacitor current as shown in (2.6) and repeated below for convenience:

$$i_m^k = n^k i^k \tag{2.33}$$

This current affects the arm capacitor voltage through the impedance Z of the equivalent capacitor C:

$$v_c^k = Z n^k i^k \tag{2.34}$$

This voltage is again modulated as in (2.2). With the expression for the capacitor voltage in (2.34), the modulated voltage becomes:

$$v_m^k = (n^k)^2 Z i^k \tag{2.35}$$

As seen in (2.35) the arm voltage v_m^k is directly depending on the arm current i^k through a modulation product and an impedance. The impedance has only a scaling effect on the arm current. Therefore, the only source for new harmonics in the arm voltage can be from the modulation products. Using the expressions for the modulation indexes derived in (2.8) and (2.9) the combined effect of the modulation can be expressed as:

$$(n^U)^2 = \frac{1}{4} - 2\hat{n}cos(\omega t) + \hat{n}^2 cos^2(\omega t) \tag{2.36}$$

$$(n^L)^2 = \frac{1}{4} + 2\hat{n}cos(\omega t) + \hat{n}^2 cos^2(\omega t) \tag{2.37}$$

In general two cosine terms with frequency m and n can be expanded using the identity:

$$cos(m\omega t)cos(n\omega t) = \frac{1}{2}(cos((m-n)\omega t) + cos((m+n)\omega t) \tag{2.38}$$

Expanding the squared cosine terms in (2.36) and (2.37) using (2.38) with $m = 1$ and $n = 1$ and sorting them give:

$$(n^U)^2 = \frac{2\hat{n}^2 + 1}{4} - 2\hat{n}cos(\omega t) + \frac{\hat{n}^2}{2}cos(2\omega t) \tag{2.39}$$

$$(n^L)^2 = \frac{2\hat{n}^2 + 1}{4} + 2\hat{n}cos(\omega t) + \frac{\hat{n}^2}{2}cos(2\omega t) \tag{2.40}$$

Equation (2.39) and (2.40) show that the modulation signals have three frequency components: a DC, a fundamental and a second ordered harmonic component. Interestingly, all the even-ordered components (the DC and second ordered harmonic) between the upper and lower modulation indexes are identical and with the same polarity while the odd-ordered fundamental harmonic have identical terms, but with the opposite polarities. This will later show to be an important property for the distribution of the harmonic content in the MMC.

The circular dependence can now be described using the expressions for the modulation products. If the arm current is assumed to have an nth harmonic $i_n^k = \hat{i_n}cos(n\omega t)$, the arm voltages will contain, due to the modulation products, harmonics of nth, (n±1)th and (n±2)th orders as dictated by the identity of (2.38). Since the arm voltages, by the definition of Table 2.1, make up the driving voltages, these harmonics will propagate into the driving voltages as well. The driving voltages will then propagate these harmonics into both the circulating and grid current, in other words, back into the arm currents. These new arm current components are then modulated into even higher-ordered harmonics creating a cycle that produces infinitely many higher-ordered harmonics from any initial frequency components.

2.5.4 Harmonic Distribution in Σ-Δ Variables

The harmonic distribution in the Σ-Δ variables can now be derived. The components will be found by looking at the components in the modulated arm voltages using (2.35). Additionally, since the driving voltages of the circular current and the grid current are decoupled, it is meaningful to analyze the effect of each current individually taking advantage of the superposition principle.

Distribution in Σ Variables

Beginning with the Σ variables, the influence of the circulating current and the grid current is sorted into two different voltage sum parts:

$$v_m^\Sigma = v_{m,\Sigma}^\Sigma + v_{m,\Delta}^\Sigma \tag{2.41}$$

The voltage sum caused by the circulating current, $v_{m,\Sigma}^\Sigma$, is found by substituting i^k with i^Σ in (2.35). It can be noted from (2.24) and (2.25) that i^Σ have the same polarities in the expression of the arm currents. Therefore, due to cancellations, this voltage becomes:

$$v^{\Sigma}_{m,\Sigma} = Z((n^U)^2 + (n^L)^2)i^{\Sigma} \tag{2.42}$$

where the sum of the upper and lower modulation products are:

$$(n^U)^2 + (n^L)^2 = \frac{2\hat{n}^2 + 1}{2} + \hat{n}^2 cos(2\omega t) \tag{2.43}$$

As seen by (2.43), the sum of the modulation products only consists of even-ordered harmonics. Therefore, if the circulating current only consists of even-ordered harmonics, only even-ordered harmonics will be produced in $v^{\Sigma}_{m,\Sigma}$. Conveniently, the only necessary component of the circular current are the even-ordered DC component.

On the other hand, the grid current i^{Δ} have the opposite polarities in (2.24) and (2.25). The voltage sum influenced by the grid current, $v^{\Sigma}_{m,\Delta}$, found by substituting i^k with i^{Δ} in (2.35) therefore becomes:

$$v^{\Sigma}_{m,\Delta} = Z((n^U)^2 - (n^L)^2)\frac{i^{\Delta}}{2} \tag{2.44}$$

where the difference of the upper and lower modulation products are:

$$(n^U)^2 - (n^L)^2 = -4\hat{n} cos(\omega t) \tag{2.45}$$

As seen by (2.45), the difference of the modulation products only consists of an odd-ordered harmonic. Therefore, if the grid current only consists of odd-ordered harmonics, only even-ordered harmonics will be in $v^{\Sigma}_{m,\Delta}$. Conveniently, the only necessary component of the grid current is the odd-ordered fundamental frequency component.

To sum up, if only the necessary components are produced by the MMC controller, the voltage sum v^{Σ}_m will only contain even-ordered harmonics. The voltage sum, being the driving voltage of the circulating current, will only inflict even-ordered components in the circulating current. These even components can, by the circular dependence, only produce even components in the voltage sum. Consequently, *all Σ variables will only have even-ordered harmonic components when the controller produces the necessary harmonic components.* This is true as long as there are no disturbances causing even-ordered harmonics in the grid current or odd-ordered harmonics in the circulating current.

Distribution in Δ Variables

The same analysis can be done for the voltage difference v^{Δ}_m. It can be divided into two parts depending on the source of the current:

$$v^{\Delta}_m = v^{\Delta}_{m,\Sigma} + v^{\Delta}_{m,\Delta} \tag{2.46}$$

where the parts are given by:

$$v^{\Delta}_{m,\Sigma} = Z((n^U)^2 - (n^L)^2)i^{\Sigma} \tag{2.47}$$

$$v^{\Delta}_{m,\Delta} = Z((n^U)^2 + (n^L)^2)\frac{i^{\Delta}}{2} \tag{2.48}$$

It can be seen that the voltage influenced by the circulating current, $v^{\Delta}_{m,\Sigma}$, now consists of the difference in the modulation products, $(n^U)^2 - (n^L)^2$, while the voltage influenced by the grid current, $v^{\Delta}_{m,\Delta}$, is modulated by the sum of the modulation products, $(n^U)^2+(n^L)^2$. Evidently, they have switched places compared to parts in the voltage sum.

As a result, both voltages will only produce odd-ordered harmonics if the arm currents contains only the necessary components. The voltage difference v^{Δ}_{m}, being the driving voltage of the grid current, will only inflict odd-ordered components in the grid current. These odd components can, by the circular dependence, only produce odd components in the voltage difference. Consequently, *all Δ variables will only have odd-ordered harmonic components when the controller produces the necessary harmonic components.* This is true as long as there are no disturbances causing even-ordered harmonics in the grid current or odd-ordered harmonics in the circulating current.

The conclusion of the analysis is summed up in Table 2.2. The upper-lower arm current variables contain both the circulating current and the grid current and have therefore both odd- and even-ordered harmonics. Thus, it is shown that the Σ-Δ notation has fewer frequency components in its variables compared to the upper-lower notation.

	Σ variables	Δ variables
Harmonic components	even	odd
Assumption: no components of ...	odd	even

Table 2.2: Main conclusions from the frequency distribution analysis.

2.6 MMC Imbalances

Power mismatches are the most important event to handle when MMCs are to be used for grid-connected DERs. Previously, the MMC has been most common in HVDC applications where the converter is situated between two balanced power sources: the grid and a common constant DC bus. However, characteristic for DERs is that the power produced most likely will differ between each resource because of the environmental or loading conditions. As a consequence, the power produced in the MMC will differ between the arms and, if no countermeasures are taken, the voltages and output currents of the MMC will become unbalanced.

In this thesis an MMC model developed by SINTEF is used to simulate the connection of DERs. The power mismatch compensation techniques used in this model are based on the analysis of Soong and Lehn [12] which divides the mismatches into three cases depending on where the power and voltage differences appear:

- **Phase imbalance**: an imbalance between the phases of the MMC. This imbalance is also referred to as a horizontal imbalance since the imbalances occur horizontally in the MMC topology.
- **Arm imbalance**: an imbalance between two arms of a MMC leg. This imbalance is also referred to as a vertical imbalance since the imbalances occur vertically in the MMC topology.
- **Submodule imbalance**: an imbalance between the submodules of an MMC arm. This imbalance is also referred to as intra-arm imbalances.

The definitions are beneficial because each case must be handled by a corresponding current component to balance the MMC. All the cases can also occur at the same time and then all the current components must be implemented. All these imbalances are covered in the scenarios in Chapter 4 where the MMC operation is evaluated. The necessary compensating methods for each of these imbalances are derived below.

The capacitor voltages are the states that needs to be balanced for all the power mismatch types. In principle, only a DC component changes steady-state values permanently. Thus, it should be investigated what current components create DC components in the capacitor voltages. The analysis must look at the steady-state DC values of (2.31) and (2.32). Furthermore, the current should be a circulating current to reduce the impact on the grid. In the following analysis the grid current i^{Δ} is assumed purely sinusoidal and the upper and lower modulation indexes are assumed perfectly out of phase so that n^{Σ}=1 and n^{Δ}=$\hat{n}cos(\omega t)$. Based on this, (2.31) and (2.32) are repeated below with the assumed modulation indexes inserted:

$$C\frac{dv_c^{\Sigma}}{dt} = i^{\Sigma} + \hat{n}cos(\omega t)\frac{i^{\Delta}}{2} \tag{2.49}$$

$$C\frac{dv_c^{\Delta}}{dt} = \hat{n}cos(\omega t)i^{\Sigma} + \frac{i^{\Delta}}{2} \tag{2.50}$$

From these equations the necessary circulating current components to compensate the power mismatches can be derived.

2.6.1 Phase Imbalance

A phase imbalance occur when a leg produce more or less power, P_{leg}, than the other two phases. An equalizing power flow must then be supplied from the other phases or else the phase voltages, that is the voltage sums v_c^{Σ}, will not match the other phases when balanced current is extracted from the MMC. Based on the average power produced in the phases, P_{avg}, the balancing current for compensation of phase power mismatches, i_{dc}^{Σ}, should have a size corresponding to [13]:

$$i_{dc}^{\Sigma} = \frac{P_{avg} - P_{leg}}{v_{dc}} \tag{2.51}$$

This current has the subscript *dc* because it must be a DC current. This can be seen from an analysis of the frequency components of (2.49). The DC component in the circulating current contributes with a controllable DC component in the first term of (2.49). Moreover, the component does not affect the DC value of the voltage differences v_c^Δ in (2.50) since it is multiplied with a sinusoidal modulation index. The DC component of the phases must sum to zero for a link-less MMC, but this is automatically achieved since the components are calculated using the average phase power.

2.6.2 Arm Imbalance

When one arm produce more power than the other arm of the same leg the voltage difference v_c^Δ increases. The current component to balance this power difference cannot be DC or else it would interfere with the phase balancing. Therefore, a fundamental frequency component of the circulating current, i_ω^Σ, is chosen. The first product of (2.50) creates a DC term (and a second order harmonic) that can be used to balance v_c^Δ. At the same time the fundamental frequency component does not produce any DC terms in (2.49).

In contrast to i_{dc^Σ} more effort must be done to force the sum of each phase's i_ω^Σ to zero. Since the components must be unbalanced phasors to compensate the power mismatches, it is convenient to formulate i_ω^Σ in symmetrical components. The current components can then be forced to zero by setting the zero-sequence currents to zero. The circulating current's fundamental frequency component can then be formulated with only their positive and negative sequence components:

$$i_{a,\omega}^\Sigma = \hat{i}_\omega^p cos(\omega t + \gamma^p) + \hat{i}_\omega^n cos(\omega t + \gamma^n) \tag{2.52}$$

$$i_{b,\omega}^\Sigma = \hat{i}_\omega^p cos(\omega t + \gamma^p - \frac{2\pi}{3}) + \hat{i}_\omega^n cos(\omega t + \gamma^n + \frac{2\pi}{3}) \tag{2.53}$$

$$i_{c,\omega}^\Sigma = \hat{i}_\omega^p cos(\omega t + \gamma^p + \frac{2\pi}{3}) + \hat{i}_\omega^n cos(\omega t + \gamma^n - \frac{2\pi}{3}) \tag{2.54}$$

where γ represents a possible phase delay of the positive sequence, γ^p, or negative sequence, γ^n, and $\hat{i}_\omega^p$ and $\hat{i}_\omega^n$ represents the positive and negative sequence current amplitude respectively.

The symmetrical current references can be found from the arm power difference P^Δ in each phase. If (2.52)-(2.54) are multiplied with the positive sequence grid voltage $v^\Delta = \hat{v}cos(\omega t)$ and averaged over a full period, the power differences can be expressed as:

$$P_a^\Delta = \frac{\hat{v}\hat{i}_\omega^p}{2} cos(\gamma^p) + \frac{\hat{v}\hat{i}_\omega^n}{2} cos(\gamma^n) \tag{2.55}$$

$$P_b^\Delta = \frac{\hat{v}\hat{i}_\omega^p}{2} cos(\gamma^p) + \frac{\hat{v}\hat{i}_\omega^n}{2} cos(\gamma^n - \frac{2\pi}{3}) \tag{2.56}$$

$$P_c^\Delta = \frac{\hat{v}\hat{i}_\omega^p}{2} cos(\gamma^p) + \frac{\hat{v}\hat{i}_\omega^n}{2} cos(\gamma^n + \frac{2\pi}{3}) \tag{2.57}$$

Similarly, expressions for the reactive power Q_x of phase x can be derived. However, since only four variables are unknown, only four equations are needed and therefore the reactive power equations are summed and set to zero to maximize efficiency [12]:

$$\sum_{a,b,c} Q_x^{\Delta} = -\frac{3}{2}\hat{v}\hat{i}_{\omega}^{p} sin(\gamma^{p}) \tag{2.58}$$

It most be noted that inflicting odd harmonic components in the circulating current, such as the fundamental frequency component, will generate significantly more harmonic content in the arm currents as discussed in the previous section. A third harmonic suppressing controller can then be viable as done by Soong and Lehn [12].

2.6.3 Submodule Imbalance

If a submodule produces more or less power than the other submodules of the same arm, the voltage of that submodule will deviate from the other. Normally, this deviation is compensated by the freedom of selecting which submodules to be inserted provided by the balancing algorithm as described in Section 2.2. Sometimes, however, the balancing algorithm is not sufficient to remove the excess power produced. Three possible reasons for balancing deficiencies related to the arm current is mentioned here and illustrated in Figure 2.5. The figure shows the arm currents in blue and the arm voltages with stippled red lines. The deficiencies are explained by assuming that the submodules are generating submodules, in other words, they need to be discharged:

- **Current magnitude deficiency:** The submodule balancing may fail because the arm currents are too small to provide the necessary power flow in the submodule capacitor. This is referred to as a current magnitude deficiency. As seen in Figure 2.5a, the current magnitude deficiency is characterized by a small arm current and, as a consequence, the generated power from the submodule is more than the arm current can manage to remove.
- **Current offset deficiency:** The current magnitude might be sufficient, but it could be offset by a large DC component in the arm current. This makes the arm current either predominantly positive or negative depending on the offset. This deficiency is unwanted since it reduces the freedom of selection for the balancing algorithm. For example, as seen in Figure 2.5b, the arm current is predominantly positive and, therefore, only a small discharging power can be provided.
- **Current phase deficiency:** The phase of the current relative to the arm voltage might impact the balancing. Many submodules need to be inserted when the arm voltages are high to provide enough voltage steps for the output voltage. Consequently, the effect of the arm current during high arm voltages are amplified. Therefore, when the arm current is in phase with the arm voltage, as seen in Figure 2.5c, the arm current is positive when many submodules needs to be inserted and

negative when few are needed. The effect is that discharging of submodules are less prioritized than charging.

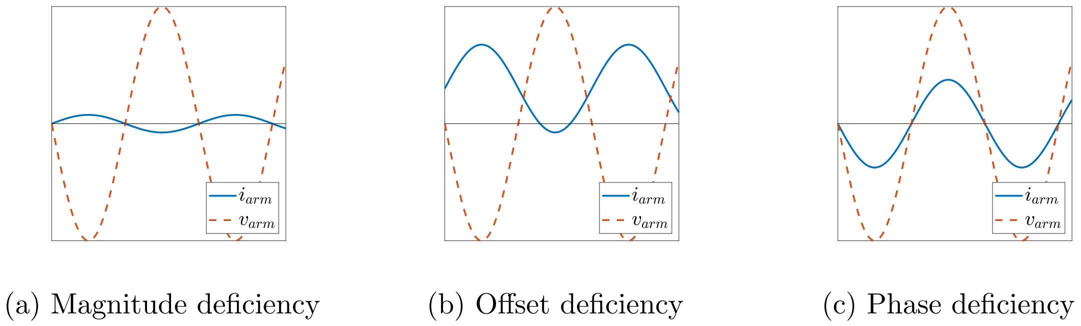

(a) Magnitude deficiency (b) Offset deficiency (c) Phase deficiency

Figure 2.5: Three submodule balancing deficiencies in the arm current.

Since the balancing algorithm is prone to deficiencies, a necessary condition for the stability of a generating submodule should be formulated. The power from the submodule can at most be removed if the submodule is inserted during only negative arm currents. The maximal discharging power P^k_{max} for a given arm current during a period T is:

$$P^k_{max} = \frac{1}{T}\int_0^T v_{sm}\min\{i^k, 0\}dt \tag{2.59}$$

If this power is less than the power from the submodule, the submodule voltage will rise and cause unstable growth. A necessary condition for the maximum discharging power is that:

$$P^k_{max} \geq |\frac{P_{DER}}{v_{sm}}| \tag{2.60}$$

If the power flow is not sufficient, the arm current needs to be boosted. The arm current can be boosted by injecting a second ordered harmonic component in the circulating current. The component will not influence the grid since it is a circulating current. Furthermore, it will not influence the other balancing methods since it is second-ordered. The size of the current component can remove the current magnitude deficiency and reduce the effect of current offset deficiency. In addition, it oscillates fast enough to minimize current phase deficiency since the injection can be both positive and negative during high arm voltages.

Since an additional current component increases the current size, it should be minimized in order to improve efficiency. However, its necessary size depends on the initial size of the arm current, the number of submodules to be inserted and the power flow from all the submodules. It is therefore hard to calculate. However, a sufficient condition for the arm current is found [16] by considering no mixed power flows and constant submodule voltages. The sufficient size of the second harmonic injection is found in the worst-case scenario by assuming that the arm current is negligible. This corresponds to the situation where only one submodule in the entire MMC is producing rated power. Then the arm current does not have to support the grid current and there are negligible power mismatches which means negligible compensating currents. In this scenario the arm current is approximately a pure second harmonic sinusoidal and its amplitude must satisfy [16]:

$$|i_{2\omega}^{\Sigma}| \geq \frac{\pi}{4\sqrt{3}} \frac{1}{v_c^k} \tag{2.61}$$

This conditions may, however, not be sufficient because of DC offset deficiency, mixed power flows and competing submodules. If only phase a is producing no power except from one rated submodule and the other phases are producing rated power, large DC compensating currents will flow from the other phases to provide internal power balancing. These current will shift the arm current to become more positive. This complicates the discharging of the rated submodule in phase a which needs negative current to discharge. Furthermore, if it is allowed for mixed power flows, all the other submodules of phase a might be consuming power. This further increases the internal power differences and the necessary DC compensating currents will become even larger. Finally, if more generating submodules are present they must compete for the possibility to be inserted when the arm current is negative. Admittedly, the conditions for discharging of submodules will be better when more generating submodules are inserted, but no argument is made to explain if this effect is greater than the competing submodule effect. The submodule balancing is, therefore, closely examined when the connectivity of the MMC is tested in Chapter 4.

2.7 MMC Base Model

The MMC base model used in this thesis is a model made by SINTEF originally proposed as an infrastructure for large-scale integration of wireless electric vehicle charging [16]. It consists of an MMC model that can be represented as both an arm averaged model and a detailed switching model. The MMC values used in the model are based on the MMC prototype built in the SINTEF testing facilities; a prototype developed by scaling a reference model of an HVDC-MMC lying between France and Spain [28]. The values are shown in Table 2.3.

MMC parameters	Values
Cells per arm	12
DC voltage	700 V
Rater power	60 kVA
Rated submodule current	83.2 A
Submodule capacitance	15 mF
Arm inductance	1.5 mH
Grid voltage	400 V

Table 2.3: MMC parameters used for simulations

The submodules of each arm in the base model is represented by a submodule capacitance and a submodule power reference. The power reference corresponds to the amount of power drawn by any electric vehicle that might be connected, but the submodule itself is otherwise independent of the specific content of each submodule. Since the power reference can serve as an abstraction of any power source in the submodule, the model is capable of representing any generalized grid-connected DERs. In this thesis, the power reference will correspond to the power produced by a PV array and a battery storage, that is, a power flow going mostly out of each submodule. The modifications of the MMC model by SINTEF to the base model for this thesis are, therefore, only done to the submodule power references.

2.7.1 Control Strategy of the MMC Base Model

The MMC base model uses a control strategy as shown in Figure 2.6. In general, the balancing of the MMC voltages are maintained in the orange blocks by computing the necessary arm current references to achieve the proper balancing. The necessary driving voltages to produce these currents are then calculated by the purple grid current and circulating current controllers. Finally, these driving voltages are implemented in the MMC by finding the corresponding modulation indexes and gating signals in the teal boxes.

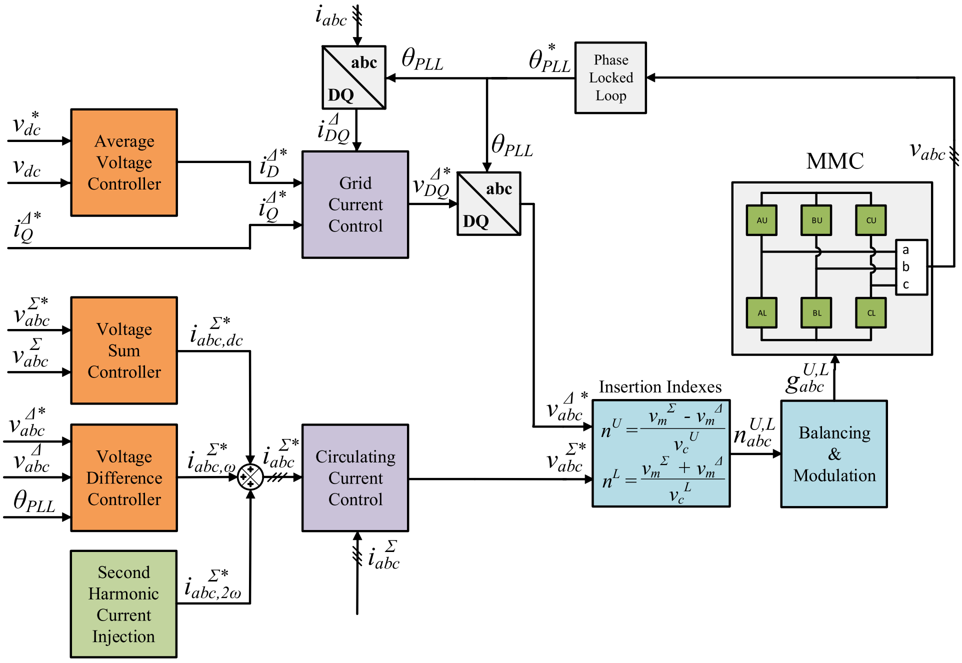

Figure 2.6: Controller for the MMC base model (adapted from [16])

The modulation indexes are determined through compensated modulation of the measured arm voltages. From the definition of the modulated arm voltage in Table 2.1, a set of modulation indexes for the upper and lower arm can be generated from:

$$n^U = \frac{v_m^\Sigma - v_m^\Delta}{v_c^U} \tag{2.62}$$

$$n^L = \frac{v_m^\Sigma + v_m^\Delta}{v_c^L} \tag{2.63}$$

From these modulation indexes the appropriate gating signals g according to the balancing algorithm are created and sent to the submodule switches.

The current controllers are implemented with standard PI blocks. The grid current controller is implemented in DQ-space with an angle θ_{PLL} created from a phase-locked loop (PLL). This is because the reference created from the average voltage controller is a constant value. This constant value i_D^Δ is the output of a PI block in the average voltage controller that forces the average arm voltage to a given virtual DC voltage. The circulating controller, however, is implemented with a PI block in *abc*-space since the circulating current references are sinusoidal. These references are the superposition of the necessary harmonics components to mitigate power mismatches. These are generated from the voltage sum controller, voltage difference controller and the second harmonic current injection as described in the previous section. The second harmonic injection is not calculated in this thesis, but is set manually for each specific case.

2.7.2 Validation of the MMC Base Model

The MMC base model was validated with generating submodules. This was mainly because the original model only was used for loading submodules, but also to demonstrate in this thesis that the model works as it should. The model was validated by step changes in the MMC during rated conditions to test each of the orange labeled controllers:

- **Average voltage controller:** a step from 1 to 1.1 p.u. in the virtual DC voltage.
- **Voltage sum controller:** a step from 1 p.u. to 0.5 p.u. in the power generated in each of the phase c arms.
- **Voltage difference controller:** a step from 1 p.u. to 0.5 p.u. in the power generated in all of the lower arms.

The benefit of testing these controllers was that if the given references were met, it implicitly demonstrates that the grid and circulating current controllers also function as desired. All the step changes were given after 1 second to let the initial transients settle and a second harmonic component of 0.45 p.u. was always injected. The resulting waveforms are shown in Figure 2.7. It must be noted that the voltage sums in Figure 2.7c are filtered with a low-pass filter with a time constant of 0.02 seconds to better visualize the waveforms.

The simulations shows that the controllers are capable of maintaining their references without affecting the grid performance. Figure 2.7a, 2.7c and 2.7e shows that the voltages initially deviates from the references, but also that the references are met before 1.4 seconds. At this time the grid currents in all the cases are shown to be largely unaffected as seen in the Figure 2.7b, 2.7d and 2.7f. This demonstrates that the MMC is capable of providing balanced power to the grid in all the cases.

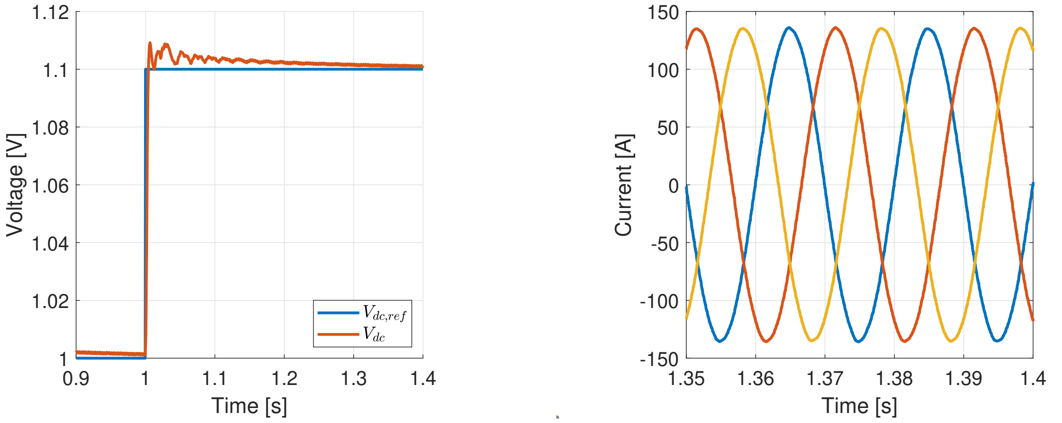

(a) v_{dc} and its reference

(b) i^{Δ} after a step in the virtual DC voltage

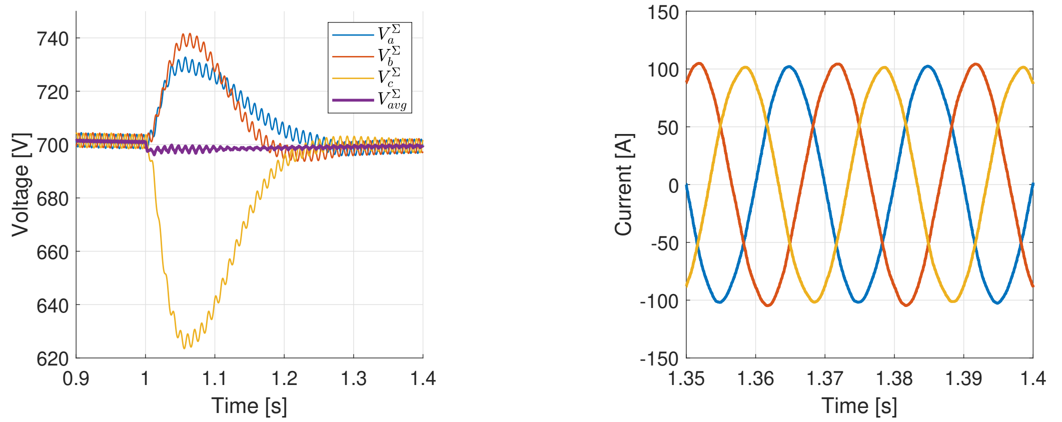

(c) The filtered v_m^{Σ} and their average value

(d) i^{Δ} after a step in the phase c power

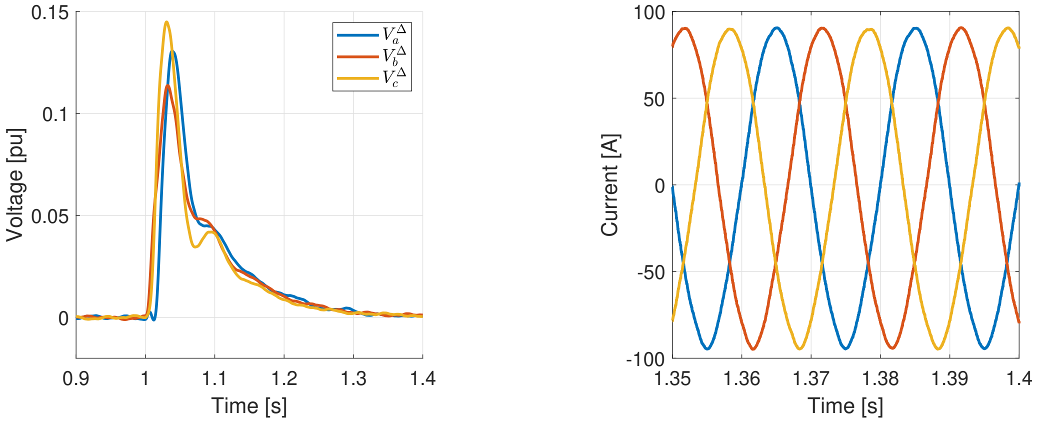

(e) v_m^{Δ} for all the phases

(f) i^{Δ} after a step in the lower arm powers

Figure 2.7: Verification of the power mismatch mitigating controllers in the MMC base model

Chapter 3

The MMC Submodule

In this chapter the submodule topology for interfacing the DERs is developed. The design is based on the discussion in [1], but some changes are applied to improve the submodule operation. First, each of the submodule components are modeled to representing the slow dynamics of the components. Then, the control strategy for the PV array and BESS is developed. Lastly, the components are sized to fit the ratings of the submodule.

3.1 Introduction

The MMC submodule is the characteristic component of the MMC. In fact, the design of each submodule is what separates the objective of two different MMCs. Due to the modular structure of the converter, each of the submodules can be designed almost independently. As a consequence, the design of a submodule can be chosen relatively freely. A justified design based on a thorough analysis of the submodule components is therefore important. This chapter is about making such a design to create an MMC submodule model suitable for controlling the power flow of a PV and BESS.

Most of the submodule modeling was done in the specialization project [1] leading to this thesis. For completeness and possible inability to access the original report, the same presentation is given here. However, the presentation here will also include some adjustments that are done based on the results found in the specialization project. Since most of the presentation is based on the specialization project, the author finds it most practical to repeat large parts of the presentation and add the descriptions of the adjustments where necessary. The specific adjustments done in this thesis are described in Section 3.2. The parts taken from the specialization project are mostly unchanged except for changes done to some of the language and notation to fit the context of this thesis.

The modeling of the submodule is outlined as follows. To begin with the necessary components and structure of the submodule is determined based on requirements necessary for reaching the MMC overall objective. Moreover, the adjustments of the original modeling is presented. A model for each of the components are then discussed and presented individually. Next, the control method for the power flow in the submodule is derived. Finally, the section is completed by sizing the submodule components.

3.2 Design of Submodule

The contents of the MMC submodule are determined based on the control objective of the MMC in general and requirements set to ensure a desired MMC operation. The overall objective of the MMC in this thesis is to interface PV arrays and BESSs. For the MMC to achieve this objective, the submodule must fulfill the following requirements:

- The submodule must be able to extract the maximum power from the PV array for a given irradiance.
- The submodule must include a storage with a controllable power flow and state-of-charge.
- The submodule must have a galvanic isolation between the power generated from the PV array and the output of the module.

In the original modeling of the submodule these requirements led to a submodule design as shown in Figure 3.1. This design fulfilled all the requirements as listed above: (1) maximum power could be obtained through maximum power point tracking in the boost converter, (2) the battery energy storage system (BESS) provided a storage which could be charged or discharged with the dual active bridge (DAB) and (3) galvanic isolation was provided by the transformer in the DAB which ensured safe conditions for the PV arrays and separate grounds for each submodule.

It was noted in the specialization project that, even though the design fulfilled the requirements, it was prone to large current fluctuations. This vulnerability appeared as a consequence of how the power flow to the BESS was controlled. The BESS equivalent model, which will be derived in Section 3.4, consists of a controlled voltage source and a series resistance as shown in Figure 3.1 to highlight the current fluctuation issue. Since the boost converter was set to control the PV power flow, the only option for controlling the battery power flow was through the DAB. The DAB could, by regulating the DC link voltage, affect the voltage difference across the series resistance to control the BESS current. However, since the series resistance of a BESS has a very low, fixed resistance, large fluctuations in the BESS current would occur even for small variations in the DC link voltage. Such variations were indeed shown to occur in the DC link voltage because of the DAB control method used.

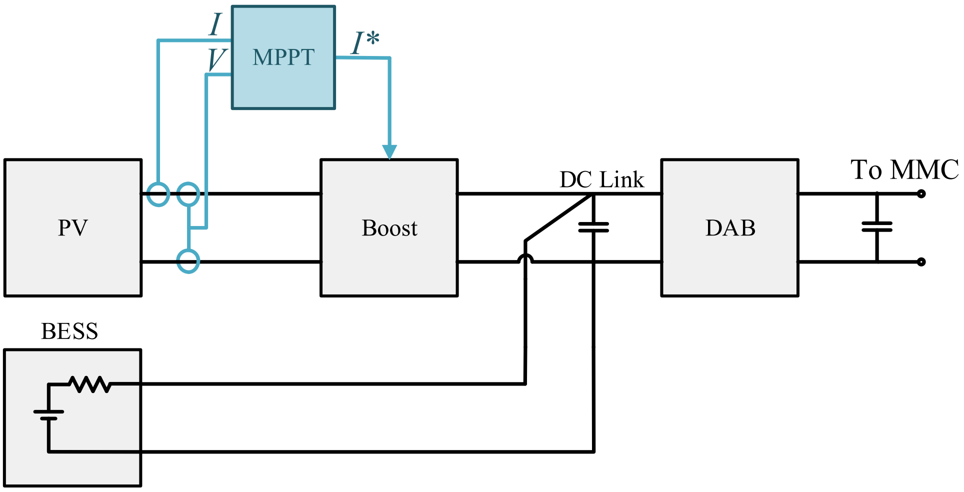

Figure 3.1: Design of the submodule as presented in the specialization project.

3.2.1 Additions To the Specialization Project

A modified design of the submodule is used in this thesis which removes the issue of large current fluctuations. The modified design is shown in Figure 3.2. From the figure it can be observed that the only difference from the submodule of Figure 3.1 is the placement of the boost converter. It is now used to interface the BESS instead of the PV.

The modified submodule must be controlled differently compared to the original submodule. First of all, the boost converter is now used to determine the current of the BESS. Since the power can go both to and from the BESS, the boost converter must be bidirectional. Regarding the PV, the power flow is controlled by the DAB through the DC link voltage. The maximum power point tracking algorithm will essentially be the same as in the original submodule except that the power tracking variable is now the PV terminal voltage instead of the PV current.

The analysis of the DAB converter has to be extended. In the modified submodule design the DC link voltage is expected to vary more when used to control the PV compared to controlling the BESS. Therefore, an analysis of the DAB operating regions and the DAB parameters must be done. In addition, the dynamics on the MMC side of the DAB must be developed. These dynamics were originally overlooked by assuming the submodule capacitor to be an ideal voltage source. This voltage source must be replaced by the original capacitor and the current dynamics must be derived.

To sum up, several adjustments and additions regarding the MMC power flow and DAB analysis must be done compared to the specialization project. The resulting simulation model can be found in Appendix C.1 and C.2. The contributions in this thesis complementing the specialization project are:

- Extending the boost converter analysis to include bidirectional flow.
- Changing the maximum power point tracking algorithm to be determined by the

PV array voltage instead of the current.

- Extending the modeling of the DAB converter by replacing the ideal voltage source with a capacitor.
- Examining the operating region of the DAB converter and the DAB parameters.

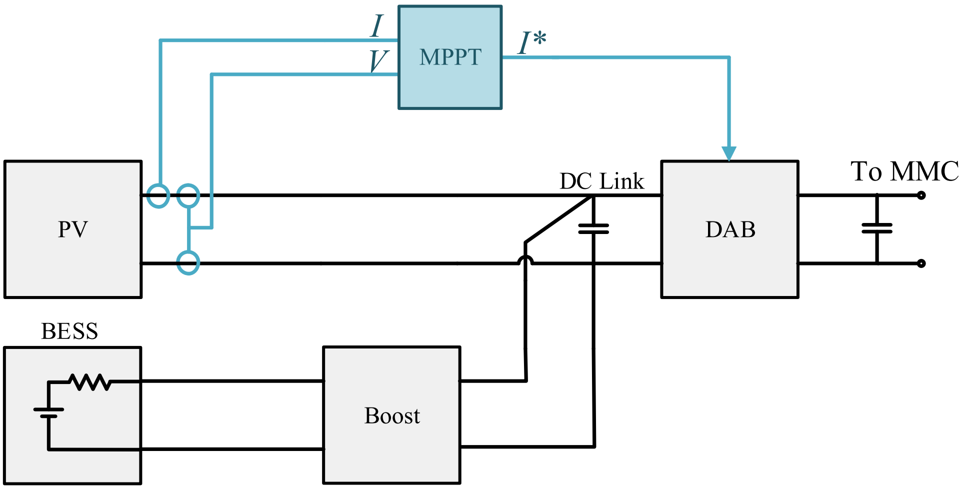

Figure 3.2: The modified submodule design used in this thesis

3.3 Modeling of PV Array

A PV cell, similarly to a diode, is created by connecting two semiconductors together that is doped to have either excess negative or positive carriers. Diffusion makes charged carriers along the border of the conductors to cross and recombine, leaving behind a charged field called a PN junction. One cell does not give the desired electric field and therefore N_{cell} cells are connected in series to create a PV panel. In addition, the panels itself can be series or parallel connected to create PV arrays. This is to further increase the voltage and current out of the PV plant.

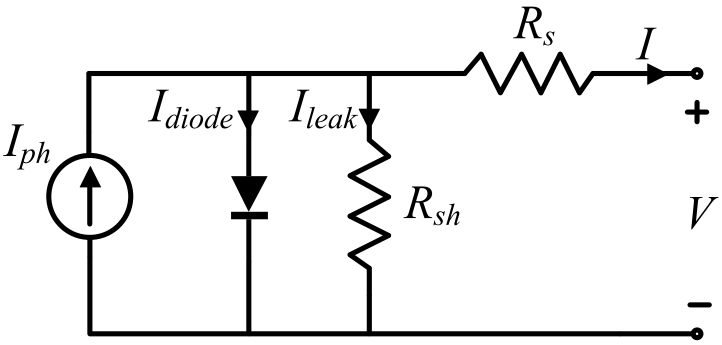

Figure 3.3: Equivalent model of a PV panel.

If all the cells are assumed to be identical, the PV panel can be modeled as shown in Figure 3.3. This is the most acknowledged model of a PV panel and it consists of four elements: a current source, a diode, a shunt resistor and a series resistor. These elements model different phenomena of the PV panel; they model respectively the photon current I_{ph}, the diode current I_{diode}, the leakage current I_{leak} and the internal losses. Each of the three first phenomena contributes with a term in the equation for the current I out of the panel:

$$I = I_{ph} - I_{diode} - I_{leak} \tag{3.1}$$

3.3.1 Photon Current

The photon current is the current produced when photons from incident light excite electrons in the PN junction of the PV cell. The junction pushes the electrons into the neutral zone and, if connected to a circuit, through a loop to be recombined on the other side of the PN junction. When the PV panel is short-circuited (SC), the first term I_{ph} dominates the other two terms so that $I \approx I_{ph} = I_{sc}$. I_{sc} is measured in tests with standard test conditions (STC) of $G_0 = 1000\ \frac{W}{m^2}$ and $T_0 = 25\ {}^oC$ and can be found in data-sheets provided by the manufacturers. However, deviances from the standard conditions can also be accounted for. When the irradiance on the cell increases, so does the number of photons that are excited. The photon current is therefore proportional to the irradiance G on the panel. In addition, changes in the temperature can be accounted for by a temperature correcting coefficient α that sets the percentage difference of I_{sc} per change of temperature ΔT. Consequently, the photon generated current can be calculated as in (3.2):

$$I_{ph} = \frac{G}{G_0} I_{sc}(1 + \alpha \Delta T) \tag{3.2}$$

3.3.2 Diode Current

As the voltage across each PV cell increases, the cell, which acts as a diode, is forward biased. The excited electrons can then cross the PN junction rather than the external loop, resulting in a reduction of current out of the cell. This current greatly depends on the voltage V_d across the diode. This voltage can be deduced from the total panel voltage V, panel current I and panel series resistance R_s assuming identical cells:

$$V_d = \frac{V + IR_s}{N_{cell}} \tag{3.3}$$

Several other parameters as the temperature T in kelvin, the diode ideality factor n, electron charge q, Boltzman constant k and saturation current I_s also determines the diode current as seen in (3.4).

$$I_{diode} = I_s(e^{\frac{q(V+IR_s)}{N_{cell}kTn}} - 1) \tag{3.4}$$

The diode factor n is a factor to compensate for the deviances from the ideal diode model, specifically, for the recombination losses in the depletion region [29]. n is normally a value between 1 and 2 depending on the semiconducting material.

Some models proposes to add two parallel diodes which can produces a sharper “knee”. This “knee” refers to the bend in the curve of the IV-characteristics similar to the bend as seen around 8 to 9 V in Figure 3.4a. Materials with such characteristics, like poly-crystalline silicon, can be modeled more accurately [30] using this method. The two-diode model is more accurate during low irradiance as well [31]. However, the model is made more complex as two more parameters, the I_s and n of the second diode, are added. Since this level of accuracy is not needed, the model proposed here only uses one diode.

3.3.3 Leakage Current

Some of the current generated may leak through the cell. To account for this effect a panel shunt resistor R_{sh} is added. The leakage current is then:

$$I_{leak} = \frac{V + IR_s}{R_{sh}} \tag{3.5}$$

3.3.4 Characteristics of a PV Array

As seen for the photon current, the environmental conditions will influence the model. In all, five parameters are affected by the irradiance and temperature: I_{ph} as described above, but also R_s, R_{sh}, n and I_s. However, for simplicity, the temperature effect in this thesis is neglected. The temperature dependence shown in (3.2) has therefore no real impact on the model and is included only for illustrative purposes.

The total equation determining the IV-characteristics of an PV array is:

$$I = \frac{G}{G_0} I_{sc}(1 + \alpha\Delta T) - I_s(e^{\frac{q(V+IR_s)}{N_{cell}kTAn}} - 1) - \frac{V + IR_s}{R_{sh}} \tag{3.6}$$

It can be noted that this equation is highly non-linear and that a closed-form formulation of either the array voltage or current is not possible. However, if the effects of R_{sh} are neglected by setting R_{sh} to infinity, a closed-form formulation for the PV voltage can be obtained. It was therefore investigated in the specialization project if such an equation would significantly reduce the computational time without sacrificing too much accuracy. The IV- and power characteristics for both the full and simplified PV array model in Figure 3.4 show that the differences were small. On the other hand, it was discovered that the reduced computational time of the simplified model was negligible and therefore the full model was preferred.

The characteristics of Figure 3.4 helps visualize the three components of the PV current and the control philosophy for the PV array. The PV current as shown in (3.1) is a

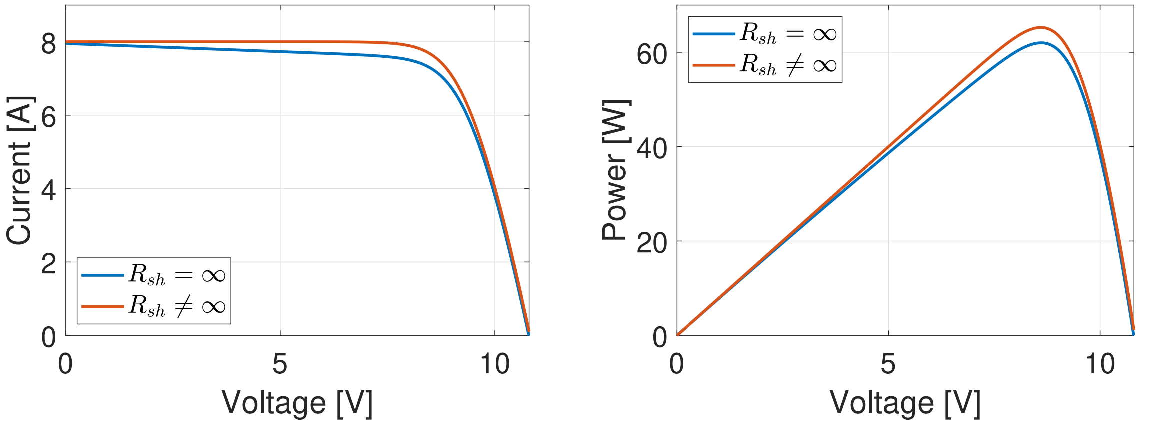

(a) IV-characteristics of the full and simplified PV model.

(b) Generated power for the full and simplified PV model.

Figure 3.4: Comparison between full and simplified PV model.

superposition of three currents where the last current, I_{leak}, is negligible. The PV current in Figure 3.4 is, therefore, seen to be the constant photon current superimposed with the negative of the well-known IV characteristics of a diode. Furthermore, Figure 3.4b shows that there exists only one voltage for which the power is maximum. Therefore, by controlling this voltage, the controller will be able to extract the maximum power. This is the principle behind the maximum power point tracking algorithm which will be described later.

3.4 Modeling of Battery

There are mainly three types of battery models [32]: the electrochemical, the mathematical and the electrical. The first of these models, the electrochemical, studies properties on a small scale by describing the flow of mass, energy and momentum of each particle as a consequence of the chemical reactions. Both kinetics and thermodynamics are needed to model the battery behavior, and the result is a system of coupled partial differential equations that must be solved in both time and space [33]. These equations can provide local temperatures and concentrations, and macroscopic values as voltage and current can be obtained by integration. This type of model is very complex and time consuming and provides a depth of information that is not needed for this thesis.

The second type of battery model is the mathematical models. These models uses empirical equations and stochastic approaches to predict battery parameters. The models can often be abstract, that is, the parameters do not always relate directly to physical properties. In addition, the accuracy of the modeling is only 5-20% [32].

The last alternative is the electrical models. The electrical models use standard electrical circuit elements to represent the battery behavior. The simplest circuit is a Thevenin equivalent circuit, that is, an open-circuit voltage with a series resistance. Often a parallel RC network is added in series as well to better reflect the transient behavior of the battery. These models are more familiar for electrical engineers and more compatible with electrical simulation programs, but remain rudimentary if not modified to include the effect of regular factors that affect the battery behavior. These factors will be described in the next section. The electrical battery model is preferred in this thesis because it is simple to implement and the necessary adjustments will be implemented to give the desired accuracy.

3.4.1 Battery Factors

The main factors that affect the battery behavior are summarized in Figure 3.5. The energy extracted from a given state of charge until the battery is empty, that is the usable capacity, can decline under certain conditions. It can be seen from the figure that four factors reduce the usable capacity: (a) increased number of discharge cycles, (b) temperature decrease, (c) increased discharge current and (d) long storage times. The figure further shows in the graph (e) that the amount of charge left in the battery, known as the state of charge (SOC), determines the open-circuit voltage of the battery. Finally, (f) demonstrates how a step change in the current create a transient dynamics in the battery voltage.

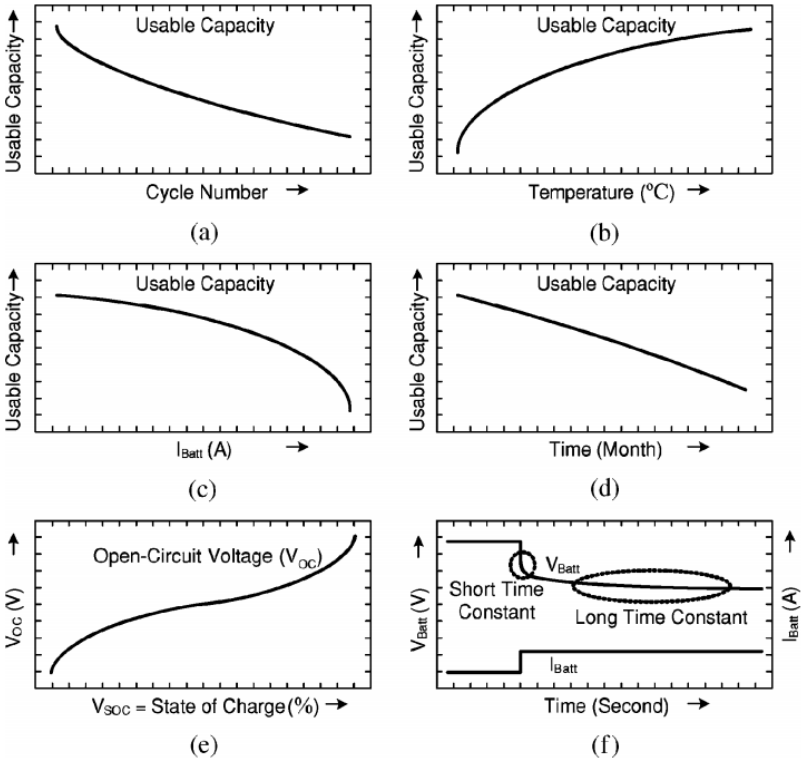

Figure 3.5: Factors affecting the battery behavior [32]

.

Many of the battery factors are disregarded since the electrical model is designed for energy management purposes. This means that some aspects of the battery behavior can be overlooked as they are not relevant for the time scale in this thesis. Compared to the slow dynamics of the energy management, the transient behavior associated with disturbances and switching from the converters are disregarded as they can be assumed to have reached steady-state. On the other hand, factors that change the usable capacity, like repeated discharge cycles and self-discharging, happens too slow to be noticeable during the energy management of a couple of discharges. In many ways, this thesis finds itself between the cost related decisions of the long time scale and the technical and safety related decisions of the short time scale. Furthermore, to reduce the complexity, temperature dependence and discharge current magnitude effects are neglected.

The battery model in this thesis includes, therefore, only the correct open-circuit voltage according to the SOC. This kind of model is similar to the generic battery model found in the Simulink library [34]. Moreover, the data necessary to implement the Simulink battery model can easily be extracted from the discharge curves provided by the manufacturers. As a consequence, the battery model in this thesis is based on the one in Simulink to ease the validation of the implemented model.

3.4.2 Battery Model

The battery model in this thesis consists of an open-circuit voltage V_{OC} and a series internal resistance R_b in a topology as shown in Figure 3.6. This is similar to the topology in [35] and the following modeling is based on the derivations from this paper. As Figure 3.6 shows, the internal resistance is always kept constant while the open-circuit voltage is varied from its equilibrium value, E_0, according to the SOC.

The SOC can be calculated by what is known as Coulomb counting. This method calculates the SOC based on the charge leaving or entering the battery. The charge, being the integral of the current, is found by measuring the current going through the battery. With this method the SOC is given by:

$$SOC = 1 - \frac{\int idt}{Q} \tag{3.7}$$

Discharge Model

The SOC influences the V_{OC} in three ways: voltage changes in the exponential zone, the polarization voltage and the polarization resistance. Each of these effect influence the discharge curve as shown in Figure 3.7 where a full battery has been discharged with a constant discharge current I_{dis} of 1 A. They are represented by individual terms in the equation for the open-circuit voltage:

$$V_{OC} = E_0 - K\frac{Q}{Q-it}it - K\frac{Q}{Q-it}i^* + Ae^{-Bit} \tag{3.8}$$

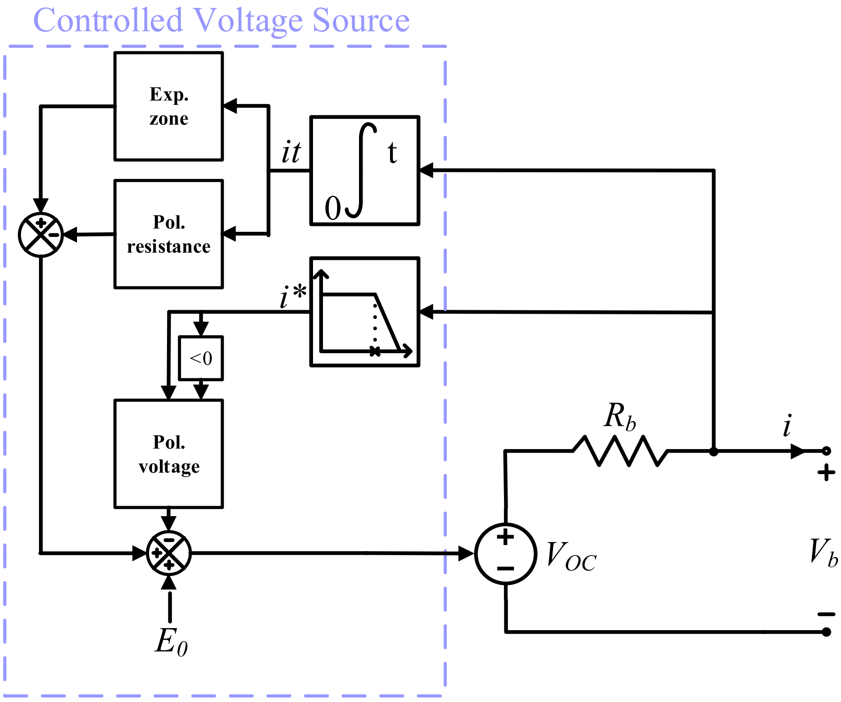

Figure 3.6: Battery model with the control system for the correct open-circuit voltage (adapted from [35])

The exponential zone is occurring only close to full SOC. It depends on the battery type and therefore a battery type must be selected. In this thesis a lithium-ion battery is chosen. The open-circuit voltage is then rising exponentially as full SOC is approached as shown in the yellow area of Figure 3.7. The characteristics of the voltage rise are determined by the constants A and B.

The last two terms originate from polarization effects. Polarization are any effects that reduce the open-circuit voltage from its equilibrium value. The polarization terms both consist of a polarization constant K and the maximum battery capacity Q, and are inversely proportional to the charge left in the battery. However, they are separated because the resistance term is proportional to the instantaneous, filtered current i^* while the voltage term is proportional to the amount discharged from the battery, it. The current must be filtered to remove algebraic loops in Simulink and can be achieved by a low-pass filter. Experimental results have shown that a low-pass filter with a time constant of 30 seconds fits most batteries. The Simulink battery model, however, used a time constant of 10 second and therefore this time constant is adopted in this thesis.

Charge Model

The equation given for V_{OC} above applies for discharging of the battery only and must be slightly modified to fit the charging mode. In real batteries, the polarization resistance increases slowly towards the fully charged state. Then, when the battery is close to the full SOC, it sharply increases like in (3.9):

$$R_{pol,ch} = K\frac{Q}{it} \tag{3.9}$$

In practice, the resistance never becomes infinity, but displays a behavior like in (3.9) that is shifted by 10% of the battery capacity. The polarization resistance during charging then becomes:

$$R_{pol,ch} = K\frac{Q}{it + 0.1 \cdot Q} \tag{3.10}$$

Summary of Batter Model

To summarize, the battery terminal voltage during charging V_{ch} and discharging V_{dis} are given by (3.11) and (3.12) respectively:

$$V_{ch} = E_0 - K\frac{Q}{Q - it}it - K\frac{Q}{it + 0.1Q}i^* + Ae^{-Bit} - iR_b \tag{3.11}$$

$$V_{dis} = E_0 - K\frac{Q}{Q - it}it - K\frac{Q}{Q - it}i^* + Ae^{-Bit} - iR_b \tag{3.12}$$

Finally, a battery alone does not give the required characteristics needed in power systems. Multiple batteries are therefore connected together into battery systems. Connecting batteries in series increase the terminal voltage of the battery system, while connecting them in parallel increases the current and the total capacity. If the system consists of N_{bp} and N_{bs} parallel and series connected batteries and the variables i, i^* and it now is denoting the total battery system current, the battery system voltage $V_{b,dis}$ for discharge is given by:

$$V_{b,dis} = N_{bs}\left(E_0 - K\frac{Q}{QN_{bp} - it}(it + i^*) + Ae^{-\frac{Bit}{N_{bp}}} - i\frac{R_b}{N_{bp}}\right) \tag{3.13}$$

Similar changes apply for the terminal voltage in the charging mode. Before the equations can be applied, the parameters in the equations have to be determined.

3.4.3 Parameter Extraction

The four model parameters E_0, K, A and B need to be calculated based on points on the discharge curve as seen in Figure 3.7. In all three points with 5 associated real parameters are used: the fully charged state (A: V_{full}), the end of the exponential zone (B: V_{exp}, Q_{exp}) and the end of the nominal zone (C: V_{nom}, Q_{nom}). Internal resistance R_b, battery capacity Q and discharge current i are also needed for the calculations, and can be found in the tables of battery data-sheets.

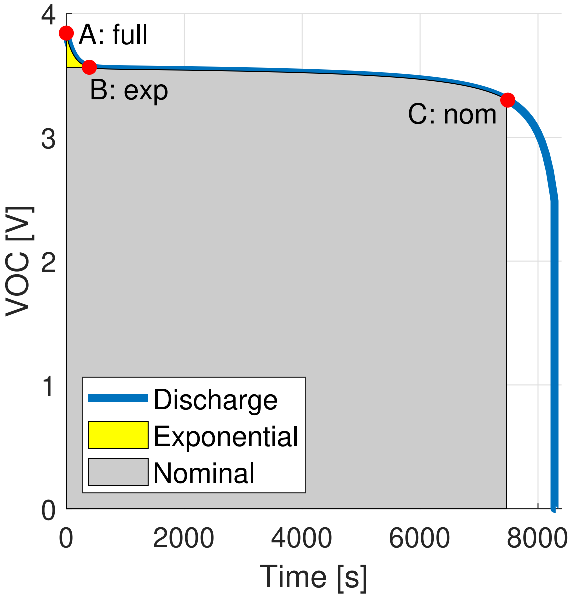

Figure 3.7: Discharge curve of the battery model.

For the fully charged state, extracted current it and the filtered current, i^*, is 0. Therefore, V_{full} can be given by:

$$V_{full} = E_0 - iR_b + A \tag{3.14}$$

At the end of the exponential zone, B can be approximated by $3/Q_{exp}$ since the exponential is close to zero ($e^{-3} = 0.04979$) after 3 time constants. Thus, B is given by:

$$B = 3/Q_{exp} \tag{3.15}$$

Furthermore, since the filtered current has reached steady-state, V_{exp} can be given by:

$$V_{exp} = E_0 - K\frac{Q}{Q - Q_{exp}}(Q_{exp} + i) + Ae^{-\frac{3}{Q_{exp}}Q_{exp}} \tag{3.16}$$

Finally, by using the end of the nominal zone to formulate (3.17):

$$K = \frac{Q - Q_{nom}}{(Q_{nom} + i)Q}(E_0 - V_{nom} - iR_b + Ae^{-BQ_{nom}}) \tag{3.17}$$

the equations (3.14), (3.16) and (3.17) can be used to find A, E_0 and K.

3.5 Modeling of Boost Converter

Compared to the modeling done in the specialization project, the boost converter in this thesis is adapted to apply for bidirectional operation. First of all, the direction of the boosting is determined. The converter is set to boost the DC link voltage to a higher voltage on the BESS side of the converter. This is to increase the terminal voltage of the BESS and lower the BESS current which is better for the operation of the BESS. Then, the diode of the standard boost converter is replaced by a switch which is turned on complementary to the existing switch. This enables the current to flow in both directions. To be able to control the voltage on the battery side of the converter, an extra capacitor is inserted. The resulting topology with two switches and their anti-parallel diodes as shown in Figure 3.8 is then capable of bidirectional power flow [36, 37].

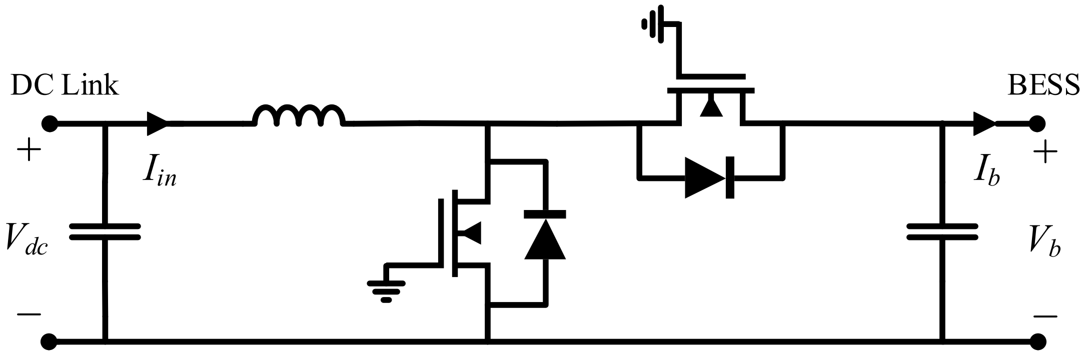

Figure 3.8: Topology of the bidirectional boost converter.

An average dynamic model of the bidirectional boost converter can be formulated [38]. Nevertheless, since only the relation between the input and output of the convert is interesting for the energy management studies in this thesis, the details of the analysis is omitted here. A more thorough analysis can be found in the specialization project. Instead, the power balance between the DC side input power P_{in} and battery side output power P_b is used to relate the input and output quantities:

$$P_{in} = V_c I_{in} = V_b I_b = P_b \tag{3.18}$$

where V_{dc} is the DC link voltage, I_{in} is the current from the DC link to the boost and V_b and I_b is battery terminal voltage and current respectively.

3.6 Modeling of Dual Active Bridge Converter

The dual active bridge topology is shown in Figure 3.9. It shows a transformer with two adjacent full-bridges. One of the bridges is connected to the submodule capacitor C_{sm} with voltage v_c while the other is connected to the DC-link capacitor C_{dc} with voltage V_{dc}. The current to the battery and the PV, the source current, is commonly denoted i_R while the current to the submodule is denoted i_{sm}.

The topology is simplified as seen in Figure 3.10. First of all, the turns ratio of the transformer is assumed to be 1:1. Secondly, the transformer is replaced by a coil resistance R and leakage inductor L. The iron core and magnetization losses are neglected. Finally, the full-bridges are replaced by binary switches. The operation of the full-bridge can only give two discrete outputs: either full capacitor voltage or neutral ground. By consecutive switching by the full-bridges, the average voltage must, therefore, be between

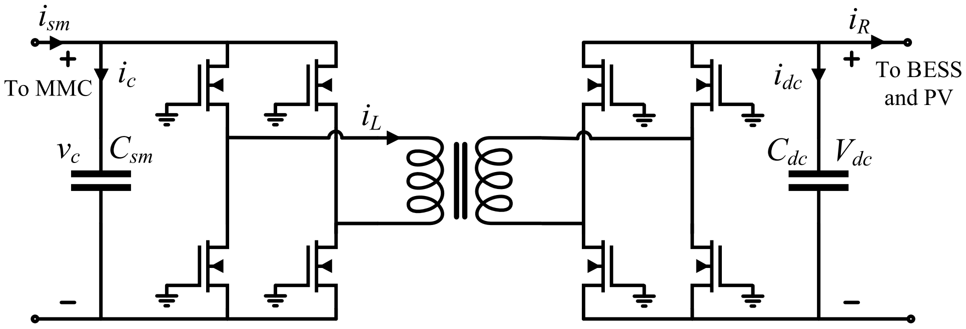

Figure 3.9: Topology of a DAB converter.

v_c (or v_{dc}) and 0 V. The new circuit elements can transfer power by DC, but a real transformer cannot. As a consequence, the inductor current must by converted to AC, but the capacitor voltage on either side of the DAB is only DC. Hence, the modulation index must be a sinusoidal variable:

$$s_i = \hat{S}sin(\omega t) \tag{3.19}$$

with an amplitude $\hat{S} \in [0, 1]$. Here the index i denotes either the modulation index of the full-bridge connected to the output capacitor ($i = 1$) or the modulation index of the full-bridge connected to the DC-link capacitor ($i = 2$).

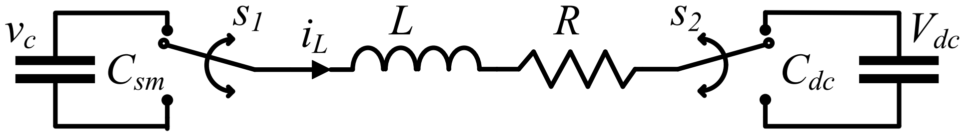

Figure 3.10: Simplified topology of a DAB converter

3.6.1 Dynamic DAB Equations

The model is now suited for formulating the dynamic equations of the converter. An equation for the inductor voltage can be formulated with the Kirchhoff's voltage law using the modulation indexes:

$$v_L = L\frac{di_L}{dt} = v_c s_1 - V_{dc}s_2 - Ri_L. \tag{3.20}$$

The same can be done for the current of the DC-link capacitor and submodule capacitor, but with Kirchhoff's current law:

$$i_{dc} = C_{dc}\frac{dV_{dc}}{dt} = s_2 i_L - i_R \tag{3.21}$$

$$i_c = C_{sm}\frac{dv_c}{dt} = -s_1 i_L + i_{sm} \tag{3.22}$$

The steady-state equations can now be obtained from (3.20)-(3.22). However, if the dynamic equations are set to zero, the solution will not be time-invariant. This is because both the modulation indices and the inductor current are sinusoidal variables. As a consequence, the derived dynamic equations must be altered to find time-invariant steady-state solutions.

3.6.2 Time-Invariant Steady-State Equations

A common method for creating time-invariant variables from three-phase systems is by the direct-quadrature-zero (DQZ) transform as described in appendix A. This transformation transfers three 120° phase-shifted variables from the time-domain into three constants in the DQZ-space. In most cases the system is symmetric so that the zero component is zero. The zero component of the DQZ transformation is, therefore, often excluded. However, a restriction of the DQZ transformation is that it can only be applied to 3-phase systems. Therefore, it cannot be directly applied to the DAB converter because it has only one phase. On the other hand, the transformation can be applied if imaginary systems consisting of virtual phases are introduced.

A virtual phase of a system is an identical, but imaginary, phase of a system that is phase-shifted by a specific angle to the phase of a real system. The virtual phase is used only for modeling purposes and is in theory separated from the circuit of the real converter model. That is, the phases should not be interconnected or the the addition of the non-existing model, that is the virtual phase, will influence the model of the real system.

It is not necessary to create two virtual phases to get the variables in DQ space. A "short-cut" can be made by creating only a 90° phase-shifted virtual phase. The rotational transform can then be applied directly, that is, the Clarke transform can be omitted. Let the real phase be denoted α and the virtual phase be denoted β. The resulting system is shown in Figure 3.11.

The general phasor X can be expressed for the real and virtual phase as:

$$X^{\alpha} = |x| sin(\omega t). \tag{3.23}$$

$$X^{\beta} = |x| sin(\omega t + 90) = |x| cos(\omega t), \tag{3.24}$$

where $|x|$ is the magnitude and ω is the angular frequency of the phasor. The phasor for both systems can also be given in vector notation as in:

$$X^{\alpha\beta} = [X^{\alpha}, X^{\beta}]^T. \tag{3.25}$$

The rotational transform must be so that the phasors are transferred to constant values without changing the magnitude of the phasors. A transform fulfilling these criteria is

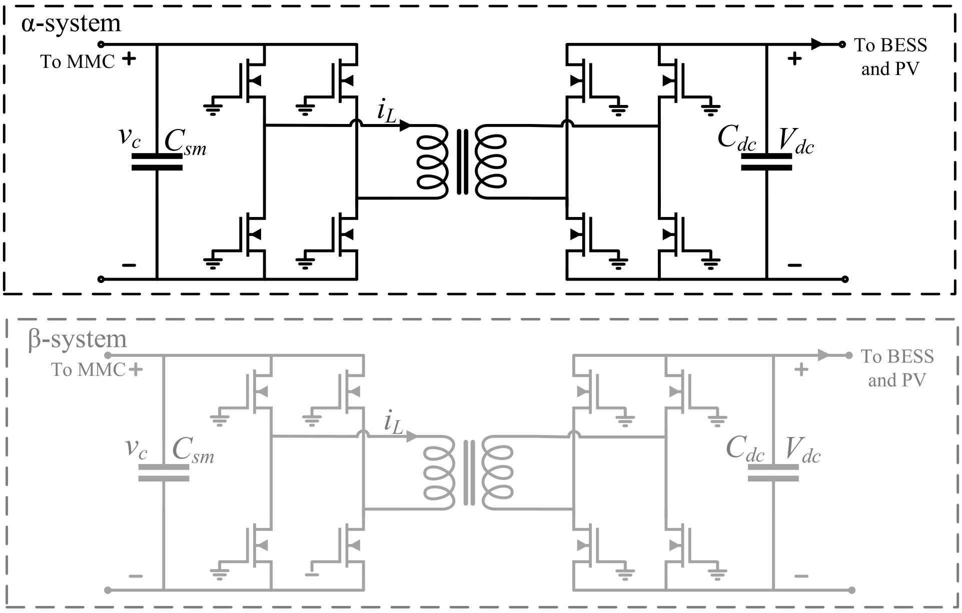

Figure 3.11: The resulting system of a real and virtual phase of a DAB.

the transform T as given in (3.26):

$$\begin{bmatrix} X^D \\ X^Q \end{bmatrix} = T \begin{bmatrix} X^\alpha \\ X^\beta \end{bmatrix} = \begin{bmatrix} sin(\omega t) & cos(\omega t) \\ -cos(\omega t) & sin(\omega t) \end{bmatrix} \begin{bmatrix} X^\alpha \\ X^\beta \end{bmatrix} \tag{3.26}$$

Equation (3.27) gives the inverse transform T^{-1}:

$$\begin{bmatrix} X^\alpha \\ X^\beta \end{bmatrix} = T^{-1} \begin{bmatrix} X^D \\ X^Q \end{bmatrix} = \begin{bmatrix} sin(\omega t) & -cos(\omega t) \\ cos(\omega t) & sin(\omega t) \end{bmatrix} \begin{bmatrix} X^D \\ X^Q \end{bmatrix} \tag{3.27}$$

The dynamic equations can then be transferred to DQ-space.

Time-Invariant Inductor Dynamics

First, equation (3.20) is formulated for both α and β and joined to a single equation using the vector notation given in (3.25):

$$L\frac{d}{dt}i_L^{\alpha\beta} = v_c s_1^{\alpha\beta} - V_{dc}s_2^{\alpha\beta} - Ri_L^{\alpha\beta} \tag{3.28}$$

The expression for the phasors given in (3.27) is then inserted in (3.28). The resulting equation is given in (3.29):

$$L\frac{d}{dt}i_L^{DQ} = v_c s_1^{DQ} - V_{dc}s_2^{DQ} - Ri_L^{DQ} - LT\frac{d}{dt}(T^{-1})i_L^{DQ} \tag{3.29}$$

As seen in (3.29), the transformation to DQ-space introduces a new term that creates a coupling between the dynamic equations. Solving this term gives:

$$LT\frac{d}{dt}(T^{-1}) = \omega L \begin{bmatrix} 0 & 1 \\ -1 & 0 \end{bmatrix} \tag{3.30}$$

The inductor equations in DQ-space then becomes:

$$L\frac{d}{dt}i_L^D = v_c s_1^D - V_{dc}s_2^D - Ri_L^D - \omega L i_L^Q \tag{3.31}$$

$$L\frac{d}{dt}i_L^Q = v_c s_1^Q - Vdcs_2^Q - Ri_L^Q + \omega L i_L^D \tag{3.32}$$

Time-Invariant Capacitor Dynamics

Then, the capacitor equations are treated. Transforming directly (3.21) and (3.22) with the transform T does not produce a time-invariant solution. This is because the terms with the modulation index and inductor current, for example $s_2 i_L$, are a product between two phasors. As seen in (3.33), this product creates a DC term and a term with twice the frequency, f, and phase-shift, θ, of the phasors in the DAB. Since the equation consists of two different frequencies (DC and $2f$), the rotational transform cannot provide time-invariant solutions. Hence, one of the frequencies must be removed.

$$s_2 i_L = |s_2||i_L|sin^2(\omega t + \theta) = \overbrace{\frac{|s_2||i_L|}{2}}^{\text{DC}} - \overbrace{\frac{|s_2||i_L|}{2}sin(2\omega t + 2\theta)}^{\text{2nd harmonic}} \tag{3.33}$$

The second harmonic can be removed by adding the capacitor currents for the real and virtual phase. The real phase has a phase-shift of $2\theta^\alpha = 0°$ while the virtual phase has a phase-shift of $2\theta^\beta = 180°$. When added together the second harmonics are completely out of phase thereby canceling each other. The resulting capacitor currents sums are denoted i_{dc}^σ and i_c^σ and given by (3.34) and (3.35) respectively:

$$i_{dc}^\sigma = i_{dc,c}^\alpha + i_{dc,c}^\beta = C_{dc}\frac{dV_{dc}^\alpha}{dt} + C_{dc}\frac{dV_{dc}^\beta}{dt} = s_2^\alpha i_L^\alpha + s_2^\beta i_L^\beta - 2i_R \tag{3.34}$$

$$i_{sm}^\sigma = i_{sm,c}^\alpha + i_{sm,c}^\beta = C_{sm}\frac{dv_c^\alpha}{dt} + C_{sm}\frac{dv_c^\beta}{dt} = -s_1^\alpha i_L^\alpha - s_1^\beta i_L^\beta + 2i_{sm} \tag{3.35}$$

Finally, the phasors can be converted to vector notation and transferred to DQ-space as seen in (3.36) and (3.37):

$$i_{dc}^\sigma = (s_2^{\alpha\beta})^T \cdot i_L^{\alpha\beta} - 2i_R = (T^{-1}s_2^{DQ})^T \cdot T^{-1}i_L^{DQ} - 2i_R \tag{3.36}$$

$$i_{sm}^\sigma = -(s_1^{\alpha\beta})^T \cdot i_L^{\alpha\beta} + 2i_{sm} = -(T^{-1}s_1^{DQ})^T \cdot T^{-1}i_L^{DQ} + 2i_{sm} \tag{3.37}$$

The resulting equations for the capacitor currents are given in (3.38) and (3.39):

$$i_{dc}^\sigma = (s_2^{DQ})^T \cdot i_L^{DQ} - 2i_R = s_2^D i_L^D + s_2^Q i_L^Q - 2i_R \tag{3.38}$$

$$i_{sm}^\sigma = -(s_1^{DQ})^T \cdot i_L^{DQ} + 2i_{am} = -s_1^D i_L^D - s_1^Q i_L^Q + 2i_{sm} \tag{3.39}$$

It is noted that the second harmonics are only canceled in the model. In the real system there is only one phase and therefore 2nd harmonics will be present. This implies that the voltage of the DC-link capacitor will not only be DC as it is assumed in the model. The model is neglecting the second harmonics by adding the capacitor currents. If (3.34) and (3.35) is interpreted physically through Kirchhoff's current law an interesting observation occurs: neglecting the second harmonics amounts to connecting the capacitor of the real phase together in parallel with the capacitor of the virtual phase. This in turn shows that the model of the real system is altered as seen in Figure 3.12. The model of the system must therefore deviate from the real system and, as described, this deviance is the exclusion of the second harmonics in the model.

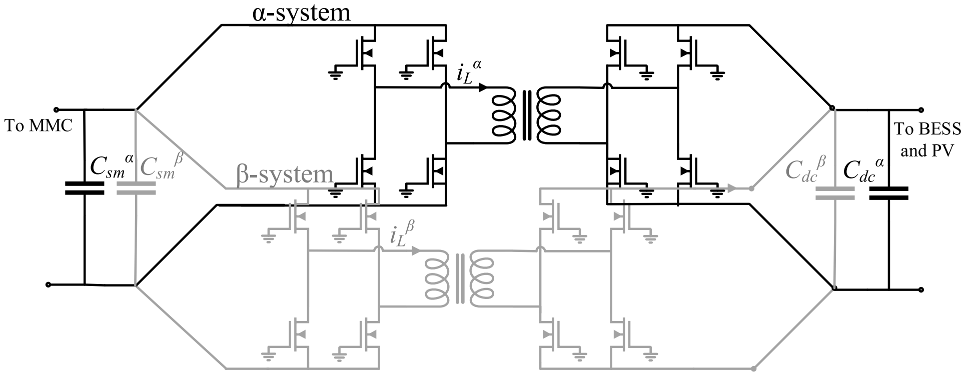

Figure 3.12: The resulting DAB topology when the second harmonics are neglected.

3.7 Control of Submodule Components

When the different parts of the module are put together they must be controlled produce the desired energy management of the module. There are in total two control objectives. The PV array must extract the maximum power and the battery must charge and discharge when needed. These objectives are governed by the DAB and boost converters respectively. Moreover, in this thesis, and in energy managements systems in general, only the steady-state operation will be studied. This chapter explains how the control objectives are accomplished in steady-state by the converters.

3.7.1 PV Power Control Using the DAB

One of the objectives in the submodule is to extract the maximum power from the PV array. As seen in Figure 3.4b in the modeling of the PV, for a given irradiance and temperature there exists a specific voltage and current for which the power produced is the maximum. This point, referred to as the maximum power point (MPP), must be set by a converter. However, since the irradiance might change so too does the MPP. As a consequence, the converter cannot rely on a point set in advance, but must be able to track the ever-changing MPP. This is done through what is known as a maximum power point tracking (MPPT) algorithm.

In this thesis the maximum power point tracking algorithm used is the perturb and observe (P&O) algorithm shown in Figure 3.13. The algorithm's working principle is that the power can be written as a function of a certain variable with only one global maximum. This variable is here denoted as the indicating variable. As seen in Figure 3.4b, the PV terminal voltage can be used as an indicating variable. In the submodule this voltage can be controlled by the DC link voltage through the DAB. The voltage is, therefore, chosen as the indicating variable and the reference determined by the P&O algorithm is sent to the DAB.

The P&O algorithm searches for the MPP by adjusting the indicating variable. The voltage has first an initial value, but are then perturbed to observe the resulting power. This power is computed by measuring the PV output current and voltage. For example, if a set of positive perturbation leads to a positive change in the power, then the algorithm should continue to give positive perturbations for the power to increase further. However, if the voltage exceeds the MPP or if the initial value of the voltage is too high, the power will decrease with the same perturbations. The perturbations should then be negative until the power starts decreasing again. After a certain amount of perturbations the algorithm will naturally tend to the MPP.

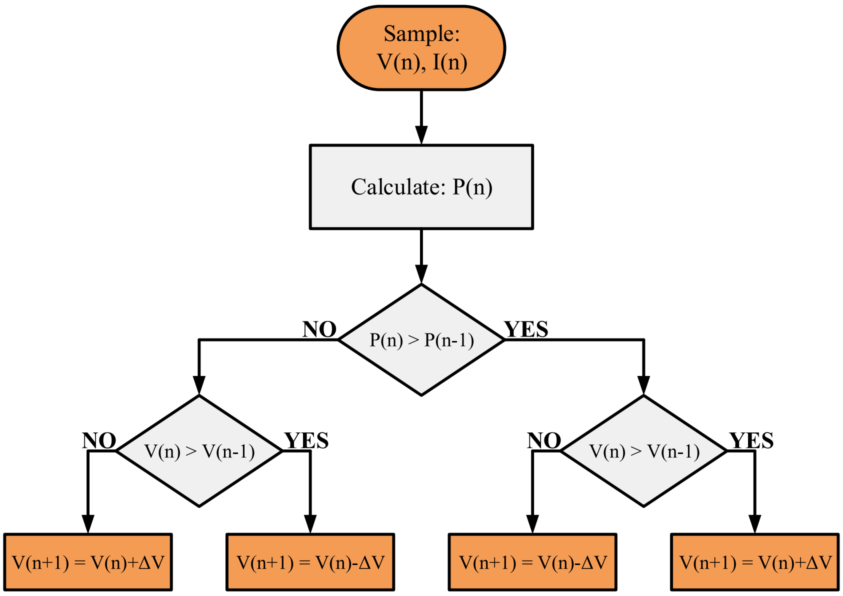

Figure 3.13: P&O algorithm with a voltage as the indicating variable.

The rest of the DAB variables can be deduced from the P&O reference. Initially the four dynamic equations of the DAB given by (3.31), (3.32), (3.38) and (3.39) have in total 7 degrees of freedom: s_1^D, s_1^Q, s_2^D, s_2^Q, i^D, i^Q and V_{dc}. V_{dc} is bounded by the P&O reference. The power factor can be specified to 1 by setting i^Q to zero. The transformer is then transferring as much of active power as possible. Finally, the modulation indexes s_1^D and s_1^Q of the full-bridge connected to the output capacitor can be specified. The submodule capacitor voltage is assumed constant and without power transfer limits. If the modulation indexes of the neighboring full-bridge are specified, the MMC-connected side of the DAB will have a slack bus behavior, that is, the MMC-connected side of the

DAB can define both its voltage magnitude and angle and can accept any amount of active or reactive power.

The remaining variables are then i^D, s_2^D and s_2^Q which can be solved for by setting the dynamic equations to zero. The equations form three second order equations with multiple parameters. They are therefore computed by the "solve" function in MATLAB using syms variables. The resulting equations are given by three MATLAB functions as shown in Appendix B.2, B.3 and B.4.

There are some possible drawbacks to the P&O algorithm. If the perturbations are too high, the algorithm will cause oscillations around the MPP. In addition, if the environmental conditions change fast during one perturbation, wrong MPPT decisions can be made [39]. As seen in Figure 3.14, when the algorithm is on point A and chooses to perturb to point B, the potential power output is decreased and the algorithm is moving away from the MPP. However, since the irradiance or temperature has changed, the power produced has increased. This leads to consecutive positive perturbations that take the algorithm first to point C and then potentially further away from the MMP as long as the environmental conditions change fast enough. It is therefore important that the perturbations are small and frequent enough so that the loss of power from fast changing conditions can be minimized.

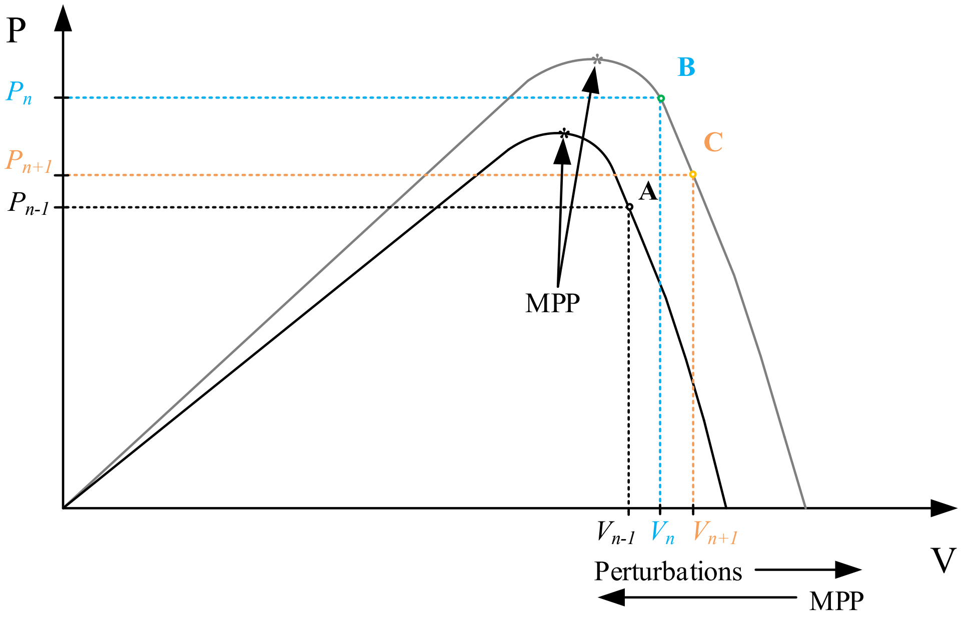

Figure 3.14: Drawback of the P&O algorithm for fast changing environmental conditions.

3.7.2 BESS Power Control Using the Boost

The BESS power flow can be independently controlled with the boost converter. The transient behavior in the boost converter is neglected which lets us assume that any given reference in the boost converter is produced instantly. For a given power reference

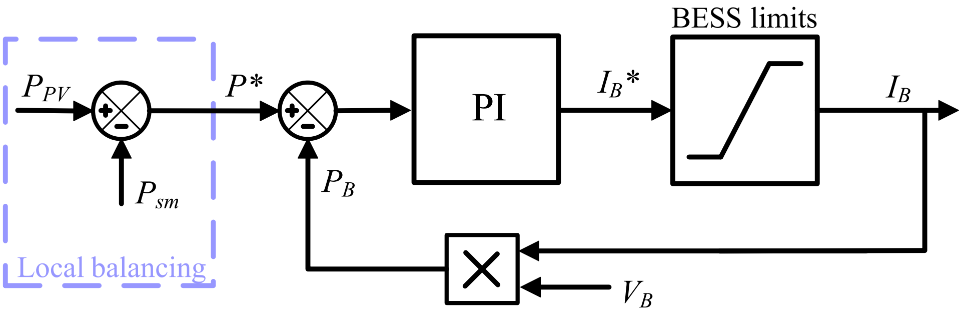

Figure 3.15: Power loop for forcing a BESS power reference

the BESS current can be calculated using the power balance relation of (3.18):

$$I_b = \frac{P_{in}}{V_b} \tag{3.40}$$

For a constant submodule power output a power loop as shown in Figure 3.15 can be implemented. A power flow P^* can be forced in the BESS by comparing it to the actual power flow P_b and sending the error to a PI block. The power flow reference can, for example, be used for local balancing by reducing the power difference between the produced PV power P_{PV} and a desired constant submodule power output P_{sm}. The PI block produces a battery current reference I_b^* that through BESS constrains are limited and becomes the battery current I_b.

The battery current is limited based on the limitations of the BESS. There are two constrains in the BESS: SOC limits and charging and discharging limits. When the SOC reaches the upper and lower limits of the allowable SOC the battery is considered disconnected. The upper limit is naturally set to 100 % while the lower limit is set to avoid deep discharges which can hurt the batteries. A lower limit of 15 % is chosen. The charge and discharge limits for the battery current depend on the battery type and the number of parallel connected batteries. The limit for charging and discharging is assumed to be the same. The limits are withheld by adding a switch to the current signal with a condition depending on the limit. If the condition fails, the switch changes from the original current signal to a saturated current signal of 0 A for the SOC limits and $N_{bp}I_{dis}$ for the discharging and charging limits.

3.8 Sizing of Submodule Components

The submodule sizing is based on the MMC ratings. These ratings set a submodule power rating of 700 W and a submodule capacitor voltage rating of 58.3 V. This, and the one-to-one conversion ratio in the DAB, let us size the PV array, BESS and converters.

3.8.1 Sizing of PV Array

The PV array is sized to provide rated power under STC. The PV panel type chosen is the poly-crystalline silicon PV panel Sharp ND-62RU1 [40] that has a maximum power at STC of 62 W. With this panel type 12 panels are necessary to deliver the 700 W submodule power output. At STC they can provide a total power of 744 W. Each panel has a voltage of 8.61 V and a current of 7.2 A at the MPP. The only common factors of 12 are 2, 3, 6 and 12, but 12 series connected panels exceed the rated submodule voltage. Therefore, 6 panels are series connected with 2 parallels giving in total 51.7 V and 14.4 A at the MPP under STC.

3.8.2 Sizing of BESS

The BESS is sized to provide the rated submodule power alone for about 2 hours. This criteria is considered sufficient to smooth most of the peaks and sags. At the same time, the BESS is small enough for issues related to the BESS limits to be investigated. The battery system is built by lithium-ion batteries similar to the lithium-ion type in the Simulink battery model. Each of the batteries is set to have a nominal voltage of 3.3 V and a rated capacity of 2.38 Ah in Simulink. Based on these values the Simulink model calculates the real battery parameters of the three points in Figure 3.7. In a real case, however, these values would be found in the data-sheet from the manufacturer. These parameters are then used to calculate the model parameters that determines the open-circuit voltage of the battery. A script for calculating the variables is shown in Appendix B and the calculation result is shown in Table 3.1.

Battery parameters			Model parameters		
V_{full}	[V]	3.8412	E_0	[V]	3.5784
V_{exp}	[V]	3.5653	K	$[\frac{V}{Ah}]$	0.010749
Q_{exp}	[V]	0.113	A	[V]	0.27712
V_{nom}	[V]	3.3	B	$[\frac{1}{Ah}]$	26.5487
Q_{nom}	[Ah]	2.08			
R_b	[Ω]	0.014348			
I_{dis}	[A]	1			
Q	[Ah]	2.38			

Table 3.1: An overview of the real and modeled battery parameters

Based on the parameters in Table 3.1 the battery system is designed. The PV voltage at STC is assumed to be boosted to twice its size on the battery side giving a total voltage of around 100 V. The number of series connected batteries giving the voltage closest to this value is 30 batteries with a total voltage of 99 V. Each battery has a maximum discharge current of 1 A and therefore the BESS must have 9 parallel connections in order to provide the rated submodule power alone. The system has then been completely specified. However the BESS must be checked if it can provide the necessary capacity of two hours with rated submodule power. The total needed capacity is $\frac{P_{bat} \cdot hours}{V_{dc}} = \frac{833 \cdot 2}{100} =$ 16.66 Ah. Since the available capacity of the designed BESS is $9 \cdot 2.38$ Ah= 21.42 Ah, the designed BESS satisfies the capacity criteria.

3.8.3 Sizing of Converters

Finally, the parameters for the converters are chosen. No values are needed for the boost converter as its dynamics are neglected and not affecting the steady-state values. The DAB converter, however, has passive circuit elements that affect the steady-state values; they are the leakage inductance and the winding resistance of the transformer. In the specialization project these elements were assigned appropriate values that where validated by simulations. These values were not the optimal ones and their valid operating regions were not investigated closer. For example, the frequency of the AC variables in the transformer were set to 50 Hz, but this frequency should normally be higher to allow for smaller and more efficient transformers. Since the DAB in the new submodule design is set to control the PV array and not the BESS, the DC link voltage is also expected to vary more. A short analysis of the operating regions is therefore done here. From this analysis more appropriate values can be selected and later validated by simulations of the DAB converter.

Selection of DAB Parameters

First, a parametric sweep is done to find possible parameter values for a high-frequency transformer. A frequency of 500 Hz is selected. The leakage inductance and winding resistance are sweeped with logarithmically spaced steps from 1 μH to 100 μH and from 1 $m\Omega$ to 1 Ω respectively. During the sweep the voltage and current from the PV is assumed to be the MPP STC values: 51.7 V and 14.4 A. The results are shown in Figure 3.16a, 3.16c and 3.16e which each shows the real value of i^D, s_2^D and s_2^Q for different values of R and L. The axes of the surface plot for s_2^D is reversed to better show the plot.

Figure 3.16a and 3.16e show that both i^D and s_2^D are independent of the leakage inductance, but strongly dependent on the winding resistance. Figure 3.16c, on the other hand, shows that s_2^Q only depends on the leakage inductance. All the figures show the same discontinuous behavior for a resistance slightly larger than 0.2 Ω. These discontinuities occur because the dynamic equations are second-order and produces imaginary solutions for $R > 0.2$ Ω; for $R \leq 0.2$ Ω there are two real solutions, but only one solution gives reasonable values.

The DAB parameters are chosen to give real DAB variables and modulation indexes below their limits. By the definition of the modulation indexes in (3.19), the indexes

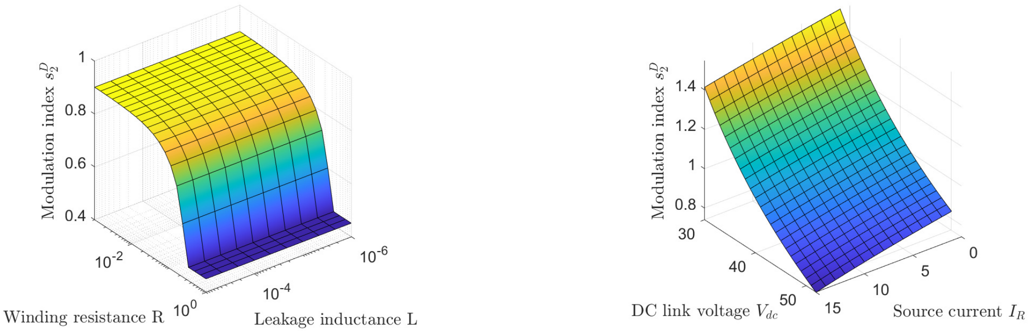

(a) s_2^D sweeped by R and L.

(b) s_2^D sweeped by I_R and V_{dc}.

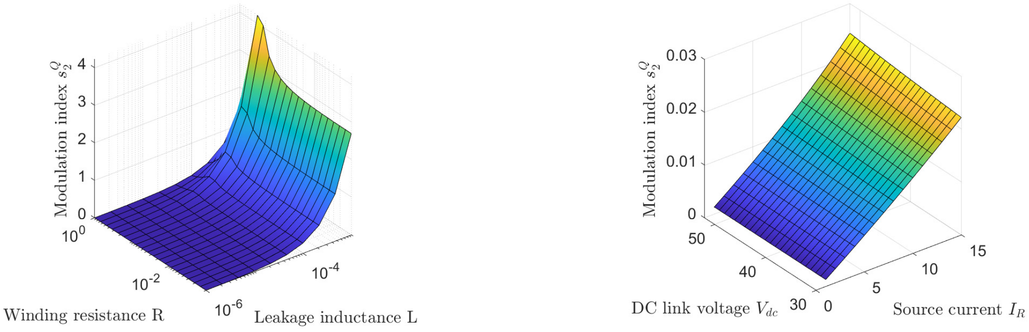

(c) s_2^Q sweeped by R and L.

(d) s_2^Q sweeped by I_R and V_{dc}.

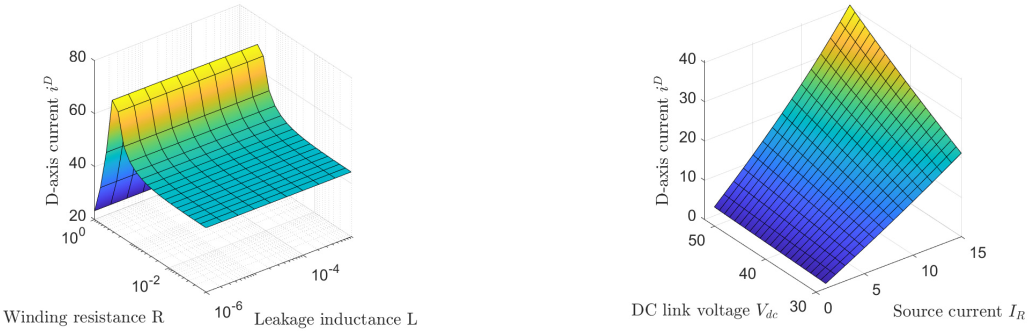

(e) i^D sweeped by R and L.

(f) i^D sweeped by I_R and V_{dc}.

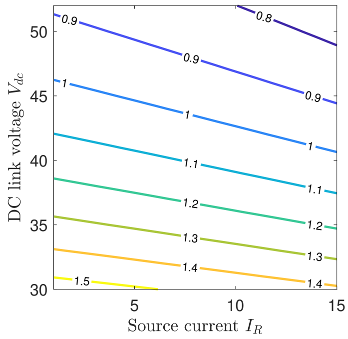

(g) Contour plot of the modulation index s_2^D sweeped by I_R and V_{dc}

Figure 3.16: Parametric sweeps of the DAB parameters and the DC link voltage and current.

cannot surpass values bigger than one. In DQ-space this amounts to the constraint:

$$(s_i^D)^2 + (s_i^Q)^2 \leq 1 \tag{3.41}$$

A leakage inductance of $L = 10\mu\text{H}$ is therefore chosen to minimize s_2^Q giving s_2^D a wider region to adapt to changing operating regions. As seen before, only $R \leq 0.2\ \Omega$ produce real values. A winding resistance of $R = 0.2\Omega$ is therefore selected.

Identification of DAB Operating Limits

The operating region for the DAB is found by sweeping the voltage and current at the DC link capacitor. The current was sweeped from 1 to 15 A while the DC link voltage was sweeped from 30 to 52 V. The resulting variable i^D, s_2^D and s_2^Q are shown in Figure 3.16b, 3.16d and 3.16f respectively. Again notice that the axes of the surface plot for s_2^D is reversed to better show the plot. A contour plot of Figure 3.16b shown in Figure 3.16g illustrates the operating region of the DAB converter. From Figure 3.16g it can be seen that in order to fulfill the constraint of (3.41), a voltage of less than 41 V cannot be sustained independent of the current size. In addition, the voltage must be at least 46 V for the converter to guarantee an existing steady-state value for all possible currents from the DERs. Since the DC link voltage is the MPPT-variable for the PV, 46 V is considered the lower limit for PV arrays. This limit is denoted V_{min}.

Figure 3.16d and 3.16f show that s_2^Q an i^D behave properly for all the operating region; s_2^Q has a negligible size and i^D show no discontinuities. i^D may seem to become higher than what seems reasonable, but it must be remember that i^D is the current that supports both the real and virtual DAB. The real DAB current is half of i^D.

Verification of the DAB Model

A simulation based on the derived parameters is done to validate both the analytic model and the existence of the derived steady-state values. The simulation model is shown in Appendix C.3. In the simulation the virtual phase is created by time delay blocks that delays the real phasors by 270°. This corresponds to a time delay T_D of:

$$T_D = \frac{0.75 \cdot 2\pi}{\omega} = 0.015s \tag{3.42}$$

The created signals are then leading the real phasors by 90° and can be set as the desired virtual phase.

The control consists of an inner current loop and an outer voltage loop as seen in Figure 3.17. The submodule capacitor is put in parallel with an ideal voltage source of the desired submodule voltage. PI blocks are used to force the desired variables since the dynamic equations of the DAB are time-invariant. To decouple the inductor equations and get rid of disturbances the inner control loop is compensated with feed-forward terms

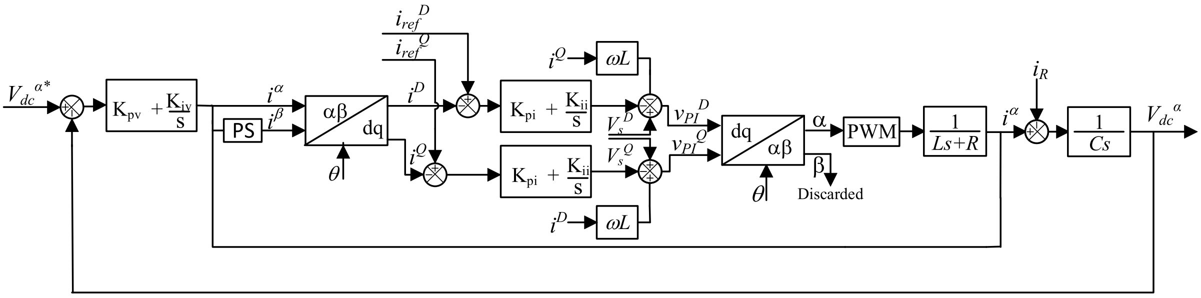

Figure 3.17: The controller of a DAB converter in DQ-space with a virtual phase generated by a phase shift (PS) of the real phase.

Converter parameters			Control parameters	
R	[mΩ]	20	K_{pi}	0.6
L	[μH]	10	K_{ii}	600
C_{dc}	[mF]	10	K_{pv}	5
C_{sm}	[mF]	15	K_{iv}	50
f	[Hz]	500		
V_{dc}	[V]	51.7		
V_{sm}	[V]	58.3		
i_R	[A]	14.4		
f_{sw}	[kHz]	50		

Table 3.2: The parameters used in the DAB simulation

$i^D L\omega$ and $i^Q L\omega$. The control parameters are found by trial and error and are given in Table 3.2.

All the predicted steady-state values are reached in the validating simulation. The waveforms for the inductor current, the DC link voltage, the modulation indexes, the inductor current in DQ-space and the submodule current are shown in Figure 3.2. All waveforms except the inductor current are filtered with a low-pass filter with a time constant of 0.005 second to filter the high-frequency noise in the signals. The DC link voltage is given an initial value of 50 V, but reaches the voltage reference of 51.7 V after approximately 0.6 seconds as shown in Figure 3.18b. The inductor current at this instant is seen to correlate with the predicted steady-state waveform highlighted with stippled red lines in Figure 3.18a. The modulation indexes and inductor current in DQ-space in Figure 3.18c and 3.18d reaches steady-state, but has a small deviance from their predicted values. The reference for the submodule current found by solving (3.39) matches the simulated current as seen in 3.18e. Overall, the analytic steady-state equations is verified by the simulations.

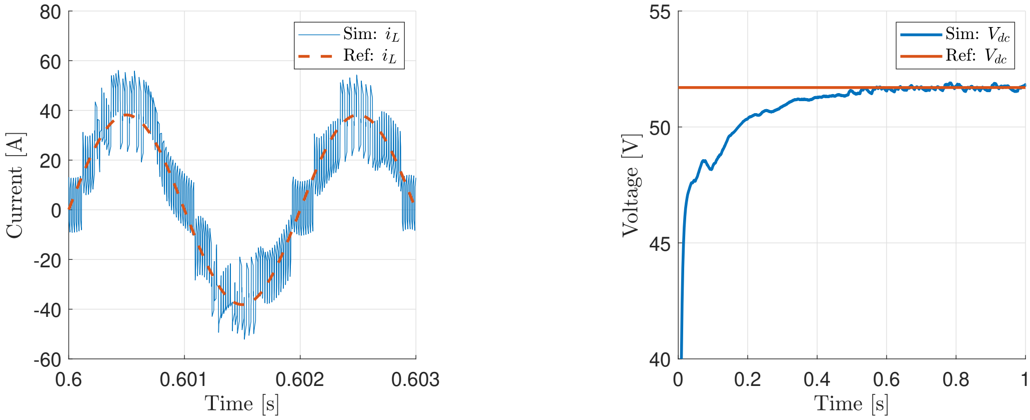

(a) The inductor current

(b) The filtered DC link voltage

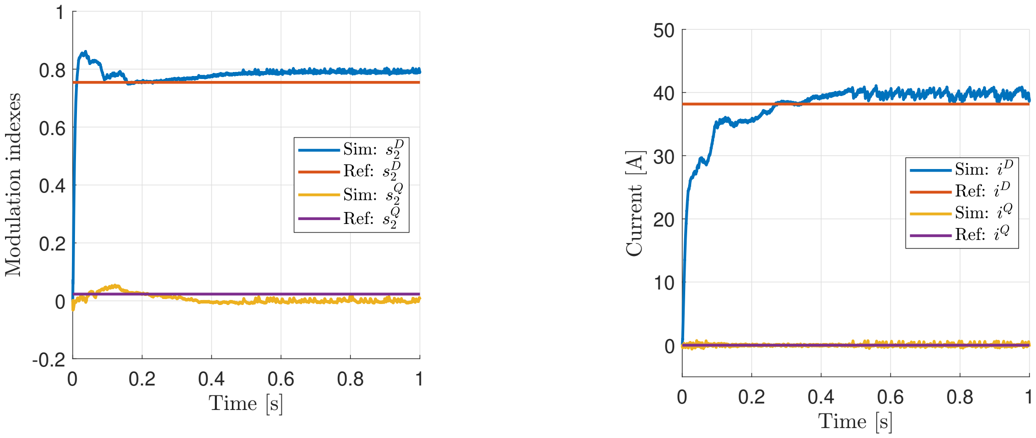

(c) The filtered modulation indexes in DQ-space

(d) The filtered inductor current in DQ-space

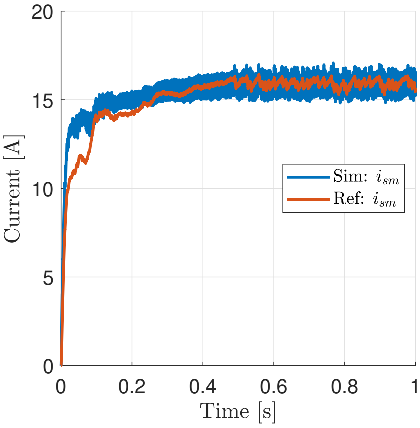

(e) The submodule current

Figure 3.18: Simulation results from the DAB model verification

Chapter 4

Performance Analysis of Grid-Connected DERs

In this chapter the MMC's ability to grid-connect uneven power from PV arrays and BESS is investigated. This is done by describing the submodule modes in a general EMS, doing a simulation for rated submodule power flows with an EMS for local balancing, and defining key performance indicators to properly assess and compare the MMC performance. Then, the different scenarios are defined. Finally, the scenarios are run and analyzed with the model developed in Chapter 2.

4.1 Introduction

One of the unique characteristics of the MMC is that the submodules can operate almost independently. When the submodules contain DERs that can either consume or produce power, totally independent power flows can come from all the submodules of the MMC. This enables the MMC to perform a wide range of energy management related actions besides producing the rated power to the grid. In theory, each submodule can be given a unique power flow reference from the energy management system (EMS) which optimizes either the submodule operation, the MMC, or the grid through ancillary services.

In practical applications, however, the MMC can only handle a certain size of imbalances before the MMC performance is unacceptable for the grid codes. As a consequence, not all combinations of power references from the EMS is sustainable for the MMC. The EMS must, therefore, make the optimizing decisions under certain power reference constraints. Consequently, before any specific EMS can be designed, an analysis mapping all the stable MMC configuration for different submodule power flows must be conducted. The ability to connect certain combinations submodule power flows is referred to as the connectivity of the DERs in this thesis and is the main research topic in this chapter.

The connectivity is best tested in the system level with rated submodule power flows. Only the submodule power flows are impacting the connectivity seen from the MMC side. The rest of the submodule operation can, therefore, be neglected when the connectivity is studied. These power flows should also be the rated ones to better test the limits of the connectivity. This is because the power mismatches are harder to compensate for larger mismatches, and the largest mismatches occurs when the submodules produce or consume the maximum power possible, that is, during their rated power flows. Additionally, zero submodule power flow is included in the analysis.

The implications of an EMS on the submodule modes must also be investigated. In the next section this is accomplished by proposing a general EMS for grid-connected PV and BESS. This general scheme is then used for the simplest possible MMC energy management: local balancing for constant power outputs in the submodules. This management is straightforward since each submodule can act independently. The local balancing is used so that rated power flows are achieved for most of the submodule modes.

To sum up, in this chapter an analysis of the MMC connectivity of DERs is carried out. First, all the possible submodule modes are formulated using a general EMS. Then examples of specific EMSs are detailed to illustrate possible EMS objectives and their resulting submodule power flows. A specific type of EMS, local balancing, is then used to illustrate how different types of maximum power references can occur with the submodules modes. The submodule modes are verified by simulations. After that, key performance indicators are formulated to assess the performance of the MMC. Finally, the MMC cases based on the rated submodule power flows are formulated, tested through simulations and analyzed.

4.2 Submodule Modes for General MMC EMSs

An energy management system is needed to communicate the submodule power commands necessary to fulfill the desired MMC objectives. These objectives can be to either improve the MMC operation or to provide ancillary services to the grid. These options are further elaborated in the next section.

Several design aspects must be addressed to create an effective EMS. These are:

- The most important submodule states must be measured to make sure the EMS decisions are feasible.
- The number of measurements should be reduced to minimize the cost of wiring and the complexity of the control system.
- It must be decided how the EMS should distribute the information to the submodules. Either a centralized or a decentralized control can be used depending on the EMS logic and the control functionality in the submodules.

There are two control possibilities when it comes to control of submodule power flows: the MPPT of the PV and the discharge current of the BESS. The MPPT can be used to adjust the power from the PV arrays. This is inefficient since it refrains the arrays from extracting the maximum power possible. On the other hand, BESSs can offer power flow flexibility without losing any power potential. Thus, the primary control of power lies in the battery power flow. Most of the EMS logic is, therefore, separated into what is referred to as the battery EMS (BEMS). Nevertheless, the MPPT is necessary as a secondary control to maintain a safe submodule operation.

4.2.1 General EMS

Based on the previous discussion, a general MMC EMS scheme for grid-connected PV arrays and BESSs is proposed in Figure 4.1. The EMS depend on the measurement of only three variables: V_{PV}, P_{PV} and the battery SOC. The control of the EMS is determined by the BEMS which performs the EMS logic based on the EMS objectives and the BESS limits. The BEMS creates three possible battery functions: charging, disconnection or discharging. However, depending on the power flow limits in the submodule, these functions results in 8 different modes with submodes as explained below.

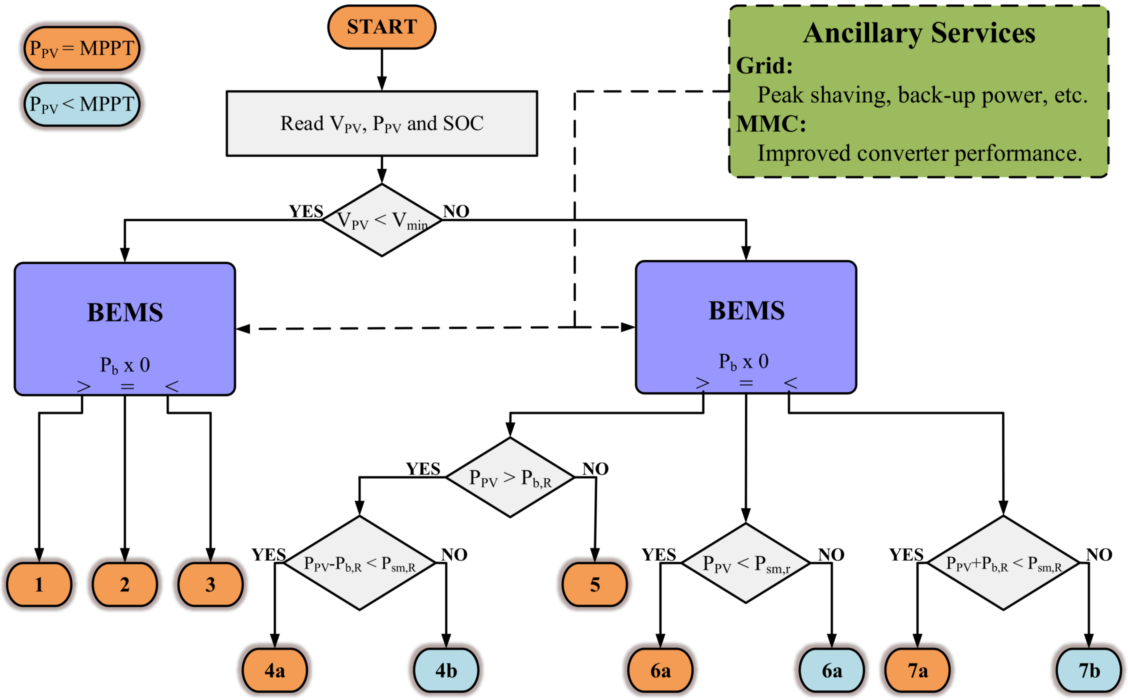

Figure 4.1: General EMS scheme and resulting submodule modes

Mode	P_{PV}	P_B	P_{sm}	Comments
Mode 1	MPPT	> 0	< 0	Disconnected PV, charging BESS, power from MMC
Mode 2	MPPT	0	0	Disconnected PV and BESS, no power to MMC
Mode 3	MPPT	< 0	> 0	Disconnected PV, discharging BESS, power into MMC
Mode 4a	MPPT	$P_{B,R}$	> 0	High PV power, rated charging of BESS, rest to MMC
Mode 4b	< MPPT	$P_{B,R}$	$P_{sm,R}$	Extremely high PV power, rated charging of BESS, adjusted MPPT for $P_{sm,R}$
Mode 5	MPPT	> 0	x	Normal PV power, charging of BESS, power to/from MMC depending on BESS power
Mode 6a	MPPT	0	MPPT	Normal PV power, BESS disconnected, PV power to MMC
Mode 6b	< MPPT	0	$P_{sm,R}$	High PV power, BESS disconnected, MPPT adjusted to $P_{sm,R}$
Mode 7a	MPPT	< 0	> 0	Small PV power, both PV and BESS power to MMC
Mode 7b	< MPPT	< 0	$P_{sm,R}$	Normal PV power, BESS discharging, MPPT adjusted to $P_{sm,R}$

Table 4.1: Description of the submodule modes.

There are three power flow limits in the EMS:

- The first limit is based on the minimum generation that can be sustained in the PV arrays. This limit splits the original 3 battery functions into at least 6 modes. In Chapter 3, it was discovered that the DAB could not support any voltages below $V_{min} = 46$ V independent of the current coming from the DERs. This was because it did not exist any real equilibrium points below this voltage that gave modulation indexes less than 1. A voltage of 46 V at room temperature is capable of producing only 36 W and so the power loss is not too significant. Therefore, the PV is disconnected if $V_{PV} < V_{min}$.
- The second limit is the battery charging and discharging limits $P_{b,R}$ which are assumed to be identical. In addition, they are assumed to be below the rated submodule power flow $P_{sm,R}$ to make sure that the battery power flow P_b in mode 3 cannot solely violate the submodule power limit. The battery power limit creates 1 more mode depending on the size of the PV produced. The battery charging

mode with the PV connected can therefore be divided in two: mode 4 or mode 5 depending on the PV power is less or more than $P_{b,R}$ respectively.

- The submodule power limit creates what is defined in this thesis as submodes. The submodes distinguish between when the PV power generation is the MPPT (submode a) and when it has to be reduced below the MPPT (submode b). Submode b is highlighted with a teal color in Figure 4.1. The submodes are not defined as independent modes to emphasize that the MMC are normally in submode a since submode b is generally undesired. Submode b occurs when the power from the DERs is more than $P_{sm,R}$. This is most likely to occur when the PV array is connected and the battery is discharging (submode 7b), but can also occur for high irradiance if the battery is disconnected (submode 6b) or when the power left from charging the battery is still more than the submodule power limit (submode 4b). Submode b is an essential part for a safe submodule operation, but PV power other than the MPPT is out of scope for this thesis.

The resulting modes are described in Table 4.1.

4.3 Battery Energy Management Systems

The battery energy management system is the system responsible for implementing the EMS objectives. The BEMS gets a power reference from an ancillary service system. With this information the BEMS must decide how it can reach the objective optimally by choosing the power references for each arm. Additionally, it must decide how the power should be distributed between the submodules of the arm without exceeding the BESS limits. These functions are addressed in this section through EMS objective examples.

4.3.1 Common EMS Objectives

First, two common EMS objectives for BESSs are presented. These objectives use the available power in the BESS to increase the MMC performance by reducing power mismatches and the fluctuations in the produced PV power. They also illustrate how any ancillary service could be provided by a BEMS.

Centralized EMS for Increased MMC Efficiency

One of the objectives the EMS can be used for is to improve the MMC efficiency. This is done in [15] by reducing the power mismatches in the converter with the BESSs. This reduces the necessary compensating circulating currents which reduces the losses in the arm resistances and increases the overall converter efficiency.

The power references for the BESSs in each arm are found by solving a linear system of two unknowns. The two unknowns are the arm-aggregated BESS power references, that is, the arm-equivalent of all the BESSs of one arm. First, an equation based on the horizontal balancing is formulated. Each leg should produce a power equal to the average leg power P_{av}:

$$P_{av} = \frac{1}{3} \sum_{k=a,b,c} P_{leg}^{k} \tag{4.1}$$

by forcing power to either the upper, $P_{bm}^{U,k*}$, or lower, $P_{bm}^{L,k*}$, arm-aggregated BESS:

$$P_{av} = P_leg^k + P_{bm}^{U,k*} + P_{bm}^{L,k*} \tag{4.2}$$

Secondly, an equation is formed for equalizing the produced upper, $P^{U,k}$, and lower, $P^{L,k}$, arm power, also using the aggregated BESS power flows:

$$P^{U,k} + P_{bm}^{U,k*} = P^{L,k} + P_{bm}^{L,k*} \tag{4.3}$$

From these equations the necessary arm-aggregated BESS power references are found to be:

$$P_{bm}^{U,k*} = \frac{P_{av}}{2} - P^{U,k} \tag{4.4}$$

$$P_{bm}^{L,k*} = \frac{P_{av}}{2} - P^{L,k} \tag{4.5}$$

Centralized EMS for Power Smoothing

The BESS in [15] is also used for smoothing of the PV. This is to counteract abrupt changes in the PV power which can cause frequency and voltage deviations in the grid. A simple moving average P_{ma} is defined for the total PV generated from the MMC:

$$P_{ma} = \frac{1}{m} \sum_{i=1}^{m} P_{PV}(i) \tag{4.6}$$

where m is the number of samples used to compute the average from the sampled vector of total PV power $P_{PV}(i)$. The smoothing power reference for each arm-aggregated BESS, P_{bs}, is simply the difference between the moving average and the actual total PV power produced:

$$P_{bs}^{U,k} = P_{bs}^{L,k} = \frac{P_{ma} - P_{PV}}{6} \tag{4.7}$$

All the arm-aggregated BESSs are given the same power smoothing reference and therefore they will not affect the power mismatches in the MMC. As a consequence, the power smoothing and the power mismatch mitigating references can be combined to a common upper, $P_{b}^{U,k*}$, and lower, $P_{b}^{L,k*}$, BESS power reference:

$$P_{b}^{U,k*} = P_{bm}^{U,k*} + P_{bs}^{U,k*} \tag{4.8}$$

$$P_{b}^{L,k*} = P_{bm}^{L,k*} + P_{bs}^{L,k*} \tag{4.9}$$

In general, the power smoothing reference could be any ancillary grid service such as peak shaving or black start aiding. In addition, it could be combined with power mismatch mitigating as long as the ancillary power references are evenly distributed between the aggregated BESSs.

4.3.2 Distribution of EMS Battery References

One of the benefits of a centralized EMSs is the added control of the system. In this thesis this control lies in the freedom of selecting which of the BESSs in an arm that should be used to serve the arm-aggregated BESS power references. The power references could be evenly distributed between the BESSs, but this would not utilize the optimal power potential. A system for selecting the optimal BESSs to serve the arm-aggregated BESS power references, a BESS-distributing energy management system (BDEMS), should therefore be implemented in the BEMS. Two BDEMS are included here.

Optimized Battery Health

One possible BDEMS could be a system to preserve and optimize the battery health. Besides from avoiding general detrimental battery operation such as too high discharge rates, excessive cell temperatures, and over- and undercharging [41], the state of the BESSs can be equalized to minimize cost. This is because maintenance costs can be reduced if all the BESSs are retired simultaneously. Equal states can be achieved by equalizing the SOC in the BESSs. This has been done in [42] by defining SOC differences between the SOC in each BESS and the average SOC. These are then fed to PI blocks to minimize the differences.

Despite equalized SOCs, the batteries might still retire differently due to complex reaction mechanisms. A more accurate BDEMS is then necessary which can be equalizing the batteries by using the battery state of health (SOH) directly. A BDEMS like this is done in [43] and a short summary of the procedure is outlined here. The battery SOH is defined as the ratio of the current maximum capacity to hold charges, Q_{max}, and the nominal capacity, Q, of a new battery:

$$SOH = \frac{Q_{max}}{Q} \tag{4.10}$$

Estimating the SOH is more complex, but is a more accurate indicator for the health of the battery since it considers the depth of discharge (DOD), the number of total life cycles and the temperature effects of the batteries. In a grid-connected BESS the space around the batteries can be assumed large enough to have temperature regulating apparatus. The effect of the temperature can, therefore, be neglected. The SOH can then be estimated by only the DOD, number of accumulated life cycles C_{acu} and some curve-fitting parameters a and b:

$$SOH(t) = SOH(0) - \frac{C_{acu}}{a \cdot DOD^{-b}} \tag{4.11}$$

The curve-fitting parameters can be found for each battery type and the values $a = 694$ and $b = 0.795$ is typically used for lithium-ion batteries. A sufficiently large number of C_{acu} is set to ensure equalized SOHs. The initial SOH, $SOH(0)$, can be found before the batteries are inserted. Then, by equalizing the SOH for BESS i with the SOH for BESS j, the necessary DOD for BESS i can be found to be:

$$DOD_i = \left(DOD_j^b - (SOH_j(0) - SOH_i(0)) \frac{a}{C_a cu} \right)^{\frac{1}{b}} \tag{4.12}$$

If j is selected as the the BESS with the largest capacity, it should be discharged the most and thus DOD_j is set to be the upper limit of DOD. After computing all the necessary DODs the arm-aggregated BESS power references can be distributed between the submodules to give individual submodule power references $P_{b,i}$:

$$P_{b,i}^* = P_b^* \frac{DOD_i}{\sum_{i=1}^{N} DOD_i} \tag{4.13}$$

Minimize Second Harmonic Injection

A BDEMS can also be used to facilitate for easier submodule balancing. The BESS can be used to equalize the power flow of the submodules by making a homogeneous submodule group that are easier to balance. This will require less second harmonic components to be injected which gives less arm losses and a higher overall MMC efficiency. This also highlights the benefit of hybrid submodules instead of dedicated submodule for BESSs since a reduction in a problematic submodule voltage is easier compensated by adjusting the power produced by that submodule than creating a more favorable arm current by BESSs elsewhere in the arm.

The power references for each submodule BESS can be found by calculating the optimal average power, $P_{op,i}$, for each submodule based on the produced submodule PV power, $P_{PV,i}$ and the aggregated BESS power reference:

$$P_{op,i} = \frac{1}{N} \left(\sum_{i=1}^{N} P_{PV,i} - P_b^* \right) \tag{4.14}$$

Each submodule BESS can then be regulated to ensure that the optimal average power is followed:

$$P_{b,i}^* = P_{PV,i} - P_{op,i} \tag{4.15}$$

4.3.3 Reference Assessment System

The BESS submodule power references are generated without considering the BESS limits. Consequently, before the references can be given, they must be assessed by a reference assessment system. This system must check the SOC and charging constraints according to the flowchart of Figure 4.2. If some of the constrains must be imposed, the excess power must be distributed between the remaining submodules. How this can be implemented, is not investigated in this thesis. The reference assessment system comes after the BDEMS, but could also be incorporated into the BDEMS. For example, linear programming could be used for minimizing the second harmonic injection by adding BESS constraints. However, a reference assessment system is kept separate here to keep the EMS general.

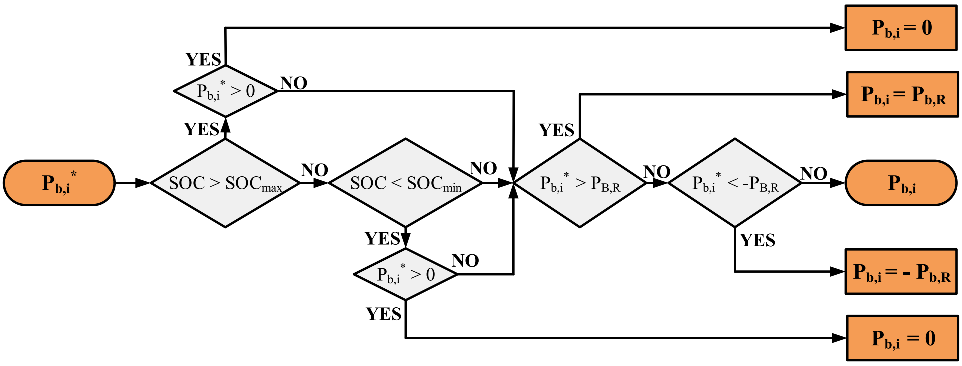

Figure 4.2: Reference assessment system conditions (adapted from [13])

4.3.4 BEMS Structure

A general BEMS for grid-connected DERs would therefore be as shown in Figure 4.3. The ancillary service system creates the necessary power reference for the EMS objective. The corresponding power reference for the arm-aggregated BESSs are then calculated. These references are then optimally distributed between the submodules of the arm by a BDEMS. Finally, the battery references are checked by a reference assessment system and given to the submodule BESSs.

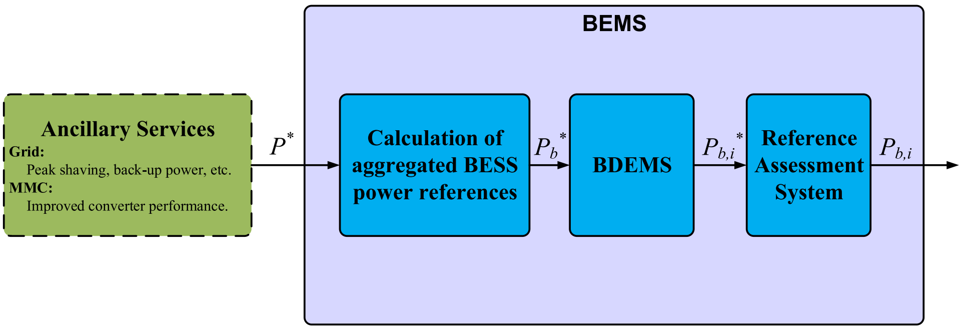

Figure 4.3: Structure of a BEMS.

4.4 EMS For Local Balancing

The proposed general EMS can be used to create rated power flows in the submodules. This can be accomplished by what is known as local balancing because the power flow is balanced locally within the submodule. As a result, the submodule power flows are rated as long as the BESS limits are fulfilled. These limits are either based on the SOC which makes $P_b = 0$ or the charging or discharging limits which makes $P_b = \pm P_{b,R}$. In these cases (possibly mode 2, 4 and 6) the submodule power flow P_{sm} is different from the $P_{sm,R}$ (but equal if the MPPT is adjusted). Beside from these special cases, the power to the MMC will be the rated power and the BESS power is $P_{PV} - P_{sm,R}$. The resulting submodule power flows in all the modes are highlighted in Figure 4.4. In the next section, which modes that are necessary to produce the rated power flows are identified and each mode is simulated.

It must be noted that local balancing can be used to specify any values in the submodule. The values used here are set to be the rated ones to test the connectivity. In most cases, however, the values would most likely be more moderate values which would be easier to generate for the submodule.

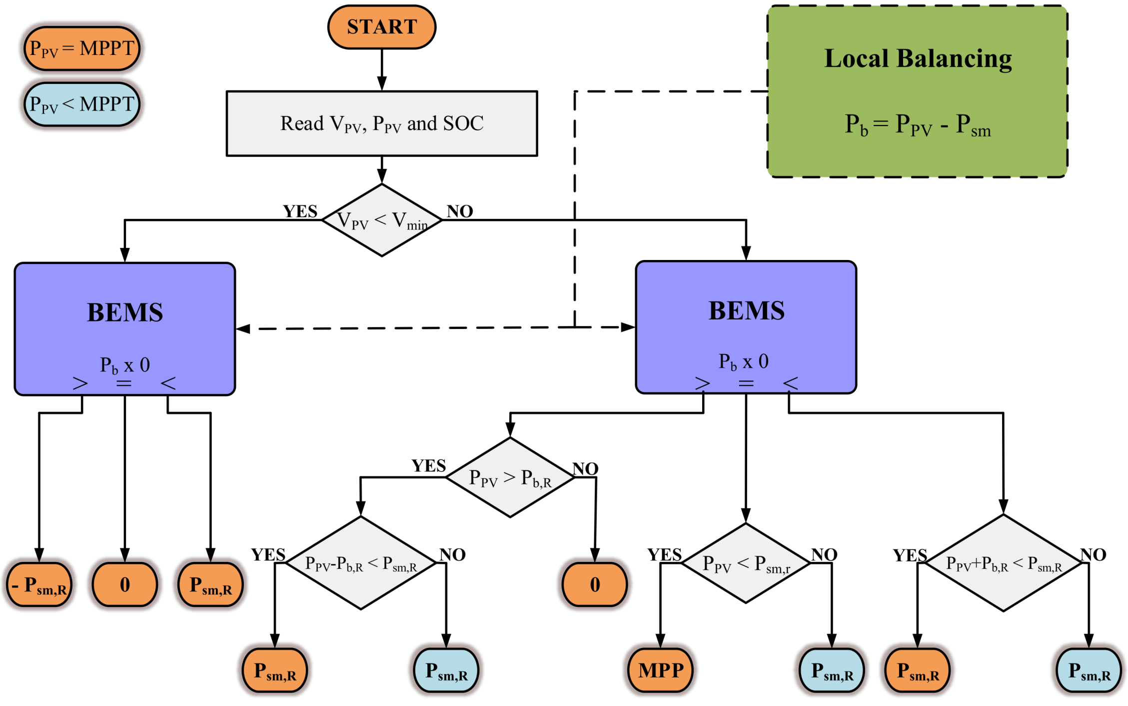

Figure 4.4: EMS scheme for local balancing and the resulting submodule power flows in all the modes.

4.4.1 Submodule States

The desired power flows that are created in the submodules can be sorted in three types of submodule states:

- **Source:** Rated power flowing from the submodule
- **Disconnected:** No power flow coming from the submodule
- **Load:** Rated power flowing to the submodule

In this section the submodules are analyzed to see how their states are maintained by the different submodule modes. Additionally, factors that can cause the modes to fail their states are identified. The operation for each of the submodule states are treated independently. The modes used for each submodule state are summarized in Table 4.2.

State	Power flow	Necessary modes	Modes deviating from objective
Source	1	3, 4 and 7	-
Disconnected	0	2 and 5	4 and 6
Load	-1	1	4 and 6

Table 4.2: Modes used to achieve the submodule states.

To display all the possible submodule modes, the submodules are analyzed during what can be assumed as a temporary shade or possible the dawn of the day. The irradiance profile describing the event is given in Figure 4.5. The irradiance is formed such that all relevant submodule modes can be displayed; the irradiance produce PV power that has a negligible size, is below rated battery power and is above rated battery power. Consequently, the irradiance profile in Figure 4.5 is sufficient to represent any possible events that can occur during a normal submodule operation. Situations with PV power below the MPPT are not considered.

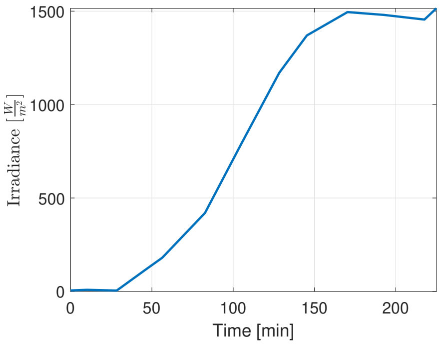

Figure 4.5: Irradiance used for simulating the submodule states.

4.4.2 State 1: Source Submodule

The first state that is investigated is denominated state 1: Source Submodule. This state represents the default submodule operation in a grid-connected MMC. The results of the simulation using the irradiance of Figure 4.5 is shown in Figure 4.6. The vertical lines in the figure indicate the borders between different submodule modes. In the simulation an initial SOC of 80 % has been assumed.

It can be seen in Figure 4.6a that the simulation of the Source state can require three different submodule modes. At the beginning of the irradiance profile the irradiance is so low that the the necessary MPPT is below the feasible capacitor voltage in the DAB. The PV is disconnected and the BESS has to discharge power to sustain a rated submodule power flow. The submodule is, therefore, in mode 3 as seen by the negative battery power and zero PV generated. This lasts until the irradiance is large enough to be sustained for PV generation at around 42 minutes. Once the PV is connected, the power produced is still below the rated submodule power flow and the BESS must continue to discharge. Thus, the submodule is in mode 7a. This continues until the PV power produced surpasses the rated power flow after 125 minutes. From this point the BESS must charge the excessive power as seen by the positive battery power flow. The submodule then works in mode 4a.

The submodule manages to fulfill the objective set by the EMS. This is because it is not prevented from doing so by either the SOC limits or the battery power flow limits. The SOC in Figure 4.6b is significantly reduced, but high enough to sustain the power output during the irradiance drop. The charging current in the same figure is seen to be well within the limits of 9 A. Figure 4.6b shows the importance of sizing the BESS correctly and having available SOC in case of a shading event. If the BESS is sufficiently sized and the power produced by the PV is not too low, the Source Submodule state is likely to be sustained.

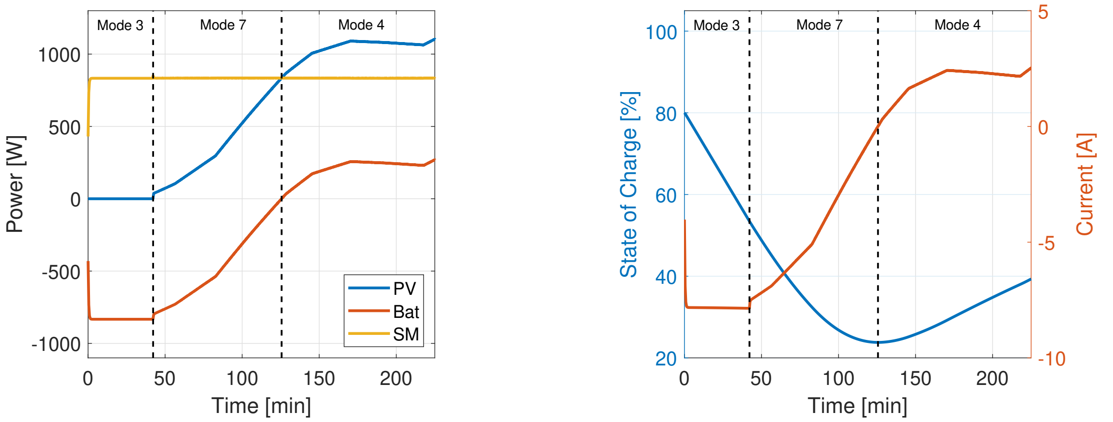

(a) Power flows in the submodule (b) The SOC and charge current of the BESS

Figure 4.6: Time-domain simulation of State 1: Source Submodule

4.4.3 State 2: Disconnected Submodule

The next submodule state that is investigated is state 2 called the Disconnected Submodule state. Its operation is shown in Figure 4.7. This state is simulated using an initial SOC of 20 %. From the three vertical lines in Figure 4.7a, the submodule is seen to operate in 4 modes. However, the state is only achieved in the two first modes as seen by the non-zero submodule power flow after 140 minutes. The failing modes are highlighted by coloring them in red. As before, the PV is disconnected in the first mode. The battery is however not discharging since no submodule power flow is desired. After 42 minutes the PV can be inserted to produce power. This power is consumed by the battery to preserve the zero submodule power flow. The submodule is then operating in mode 5.

After 140 minutes, however, the BESS limits make the submodule unable to maintain its state. The charge current in Figure 4.7b is seen to saturate at the limit of 9 A making the BESS unable to absorb all the power produced by the PV arrays. The submodule is then in mode 4 and the submodule power output is non-zero. Additionally, after 205 minutes the SOC of the BESS in Figure 4.7b is maxed out due to the consecutive charging. This lets no more power to flow to the BESS and the submodule power flow becomes equal to the generated PV power. The submodule is then in mode 6. It is seen that when BESS limits are imposed the submodule works in mode 4 and 6 which cannot not provide zero submodule power flow. These modes occur as a consequence of a too large PV power. This indicates that a low irradiance is necessary to maintain a Disconnected Submodule state unless the MPPT is to be reduced.

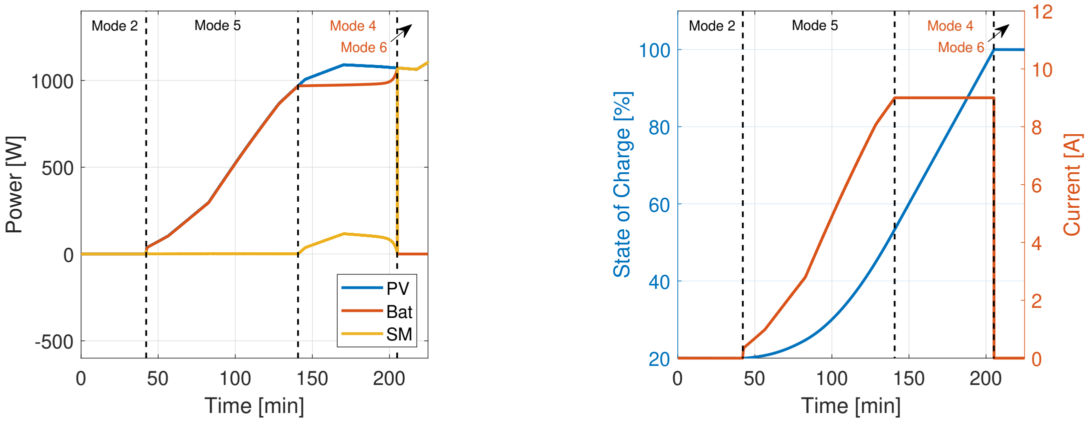

(a) Power flows in the submodule

(b) The SOC and charge current of the BESS

Figure 4.7: Time-domain simulation of State 2: Disconnected Submodule

4.4.4 State 3: Load Submodule

Finally state 3, called the Load Submodule state, is investigated in Figure 4.8. The simulation uses an initial SOC of 20 % which is to be expected for this state as it is likely to be used for BESS charging. Charging with rated power, however, is seen to be difficult in Figure 4.8a as only the two first modes manage to maintain a rated power flow into the submodule. In the first mode the PV is disconnected and the battery can discharge rated submodule power as in mode 1. When the PV is connected after 42 minutes the battery must be able to consume the PV power as well. The submodule is then in mode 5. This mode is possible for the Load Submodule state only because the BESS is sized slightly larger than the rated submodule power. The mode is, therefore, only sustained until the 61 minute mark which is when the irradiance has grown too high.

When the BESS is restricted by its limits as seen in Figure 4.8b, the Load Submodule state works in modes 4 and 6. After 61 minutes the charging limit of 9 A is met and the submodule must work in mode 4 since the submodule power inflow is reduced below the rated values. Eventually, after 117 minutes, the BESS is fully charged and the BESS power flow must be set to zero. The submodule is then in mode 6 with all the PV power produced flowing to the MMC. Evidently, the Load Submodule state with a BESS sized to the submodule power rating can only be sustained if the PV is disconnected.

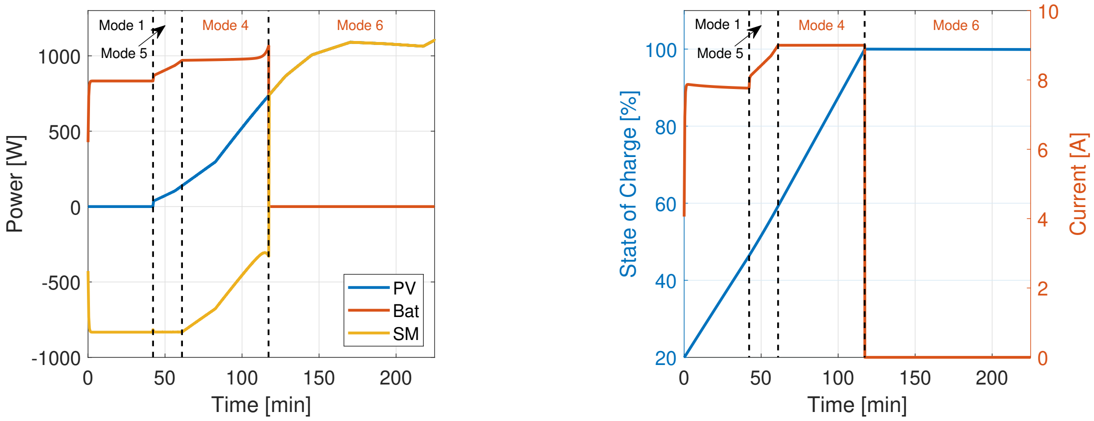

(a) Power flows in the submodule (b) The SOC and charge current of the BESS

Figure 4.8: Time-domain simulation of State 3: Load Submodule

4.5 Key Performance Indicators

To assess the performance of the MMC during its operation, three key performance indicators (KPI) have been chosen. They are important to provide a quantitative basis to rate the performance of the converter and to make sure that the converter complies with the grid codes. As a consequence, the KPIs must reflect the stability of the MMC and the quality of the power injected to the grid. Based on this, the three selected KPIs must be related to:

- The grid current phase balance
- The total harmonic distortion
- The submodule voltages

4.5.1 Grid Current Phase Balance

To the author's knowledge there are no standard limits for the imbalance in the current from a 3-phase inverter. The closest resemblance to guidelines that was found were the ones given by the NEMA MG-1 standard advising a maximum of 30 % of current imbalance in case of unbalanced voltage up to 3 % [44]. This limit, however, is considered too tolerant to suffice as a general current imbalance limit. On the other hand, there are strict limits on the voltage imbalance which indicate that voltage unbalances are prioritized more. The Norwegian voltage imbalance limit is set to 2 %, but other countries can have even stricter limits [45]. Despite no accepted standard limits for current imbalances, a current imbalance indicator is beneficial to quantitatively compare the grid currents of each case.

There are several suitable current imbalance indicators depending on which aspects of the imbalance that is to be evaluated. Imbalance in a set of phasors can come from several reasons: unsymmetrical phase shifts, dissimilar phasor magnitudes, and DC offsets. The imbalance indicator must be chosen based on what aspects of the imbalance that is to be investigated. Chicco et al. [46] defines several experimental current imbalance indicators. The most popular current imbalance indicator is the current unbalance indicator (CUF) which is defined as the ratio between the negative and positive sequence components, i_ω^n and i_ω^p, of the current's first harmonic component:

$$CUF = \frac{i_\omega^n}{i_\omega^p} \tag{4.16}$$

Chicco et al. uses this and other indicators to assess the current produced by a PV plant on the rooftops of an industrial building in Torino, Italy, where the CUF is to be below 3 %. This is reported to be below the technical thresholds. Assuming that the grid in this thesis' simulation can handle the same imbalances as the Italian one, a CUF limit of 3 % can be used to guarantee a safe operating limit for current imbalances. In addition, to reduce the impact of disturbances, a moving average of the CUF over the last fundamental period is used.

4.5.2 Total Harmonic Distortion

It is important to reduce the harmonic distortion in the grid to preserve the power quality. The most well-known harmonic content metric is the total harmonic distortion (THD), but the metric used in this thesis is the total rated-current distortion (TRD). They both indicate the quality of the current by assigning a value to the purity of the current, but they weigh the sizes of the distortions differently. The rated-current distortion of a current, similarly to THD, is the root mean squared sum of all non-fundamental components of the current. However, the TRD is divided by the rated current I_r at the "reference point of applicability" (RPA) instead of the true rms value I_{rms}, as seen in:

$$TRD = \frac{\sqrt{I_{rms}^2 - I_\omega^2}}{I_r} \tag{4.17}$$

Here the RPA is set to be the output of the MMC which makes I_r the rated current of the converter. I_ω denotes the rms value of the fundamental component of the grid current

Usually the THD increases while the TRD decreases for small currents which shows that the distortions tend to maintain their sizes irrespective of the ampere rating. In other words, the distortion increases in size relative to the total current for smaller currents. Since the maximum size of the harmonic content is more important for the grid quality, the TRD is a more convenient metric [47]. The IEEE 1547 standard [48] recommends the TRD to be less than 5 % for grid-connected DERs. These recommendations are adopted in this thesis and the TRD is also calculated with a moving average over the last fundamental period to reduce the impact of disturbances.

4.5.3 Submodule Voltages

During normal MMC operation the submodule voltages in the MMC oscillates around their rated values. These oscillations occur as a natural consequence of the arm current charging when the submodules are inserted to achieve the desired arm voltages. However, if the arm current is too small to support or compensate the submodule current flow or otherwise unable to flow due to undesired insertion, the submodule voltages will extend beyond the normal oscillating region. These voltages create instabilities and voltage spikes in the MMC and should be avoided. Therefore, a KPI for maximum voltage deviances from the rated submodule voltages is defined.

Safe limits for the oscillating region can be found by investigating the submodule voltages at the rated conditions. Since second harmonic injections of up to 0.45 p.u. can be necessary to operate the MMC, the limits in this thesis are set based on the regions at rated conditions with 0.45 p.u. second harmonic injections. This increases the acceptable region as seen in Figure 4.9a which compares the submodule voltages of the upper arm in phase *a* for rated conditions without injections and with a 0.45 p.u. injection. The wider region is necessary for the submodule voltages to satisfy the KPI for cases where second harmonic injection is needed. On the other hand, the region should not be too wide or else the region limits loses their value. Nevertheless, the relaxed limits based on injections are found to be sufficient because the oscillation in the virtual DC voltage is largely unaffected as seen in Figure 4.9b. The result is that the submodule voltage KPI is set to ±15% of the rated submodule voltage. This corresponds to voltages ranging from 49 to 67 V as seen in Figure 4.9a.

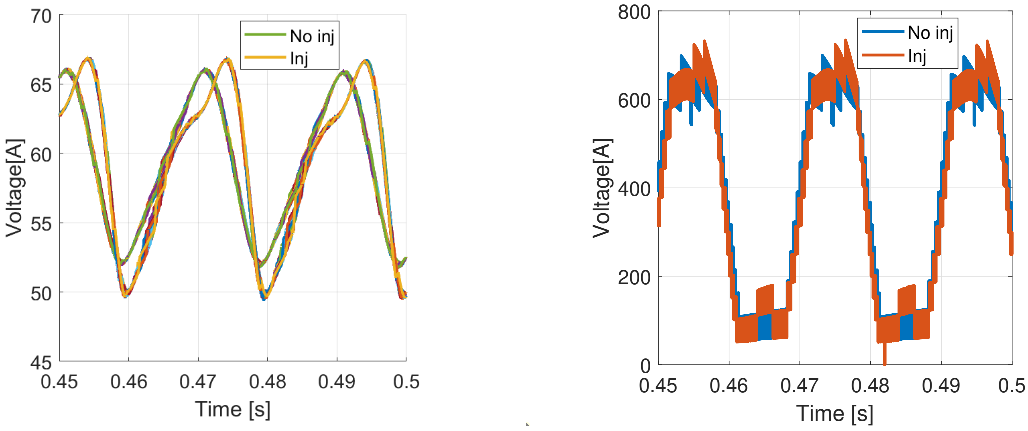

(a) Submodule voltages

(b) Arm voltages

Figure 4.9: Submodule and arm voltages in an MMC at rated conditions with and without a 0.45 p.u. second harmonic injection.

4.6 Simulation Setup For Connectivity Analysis

4.6.1 Submodule Representation

Ideally, the models described in Chapter 2 and 3 would be joined in a combined simulation model for a simulation of the complete system. The developed submodule model and MMC base model developed by SINTEF must, however, be run independently of each other to obtain fast results. First of all, due to the high number of submodules (72 in total), a full, independent model for each of the submodules would cause the MMC model to run slowly because of the computational burden. Additionally, the time scale difference between the models gives unnecessary computational time. The dynamics of the submodule are governed by the change in the environmental conditions and the SOC in the batteries which have a time scale of minutes and hours. The MMC base model, on the other hand, includes all the averaged dynamics of the converter occurring in time spans of milliseconds.

A possible solution to achieve results efficiently is to run the submodule model and sample interesting moments in the submodule operation. Compared to the submodule, the MMC dynamics are so fast that the submodule values are seen as constants. These sampled values could then be given to the MMC as constant values to find the corresponding MMC values. Consequently, the need for long MMC simulations to obtain the submodule dynamics is omitted while sufficient data can be obtained by interpolating the sampled data. The drawback is that many samples must be taken to achieve a high resolution of the MMC operation. This, combined with the high number of submodules, makes this procedure cumbersome.

The chosen solution is to neglect the submodule dynamics and to study the MMC on the system level. The submodules are represented as power references. The power references used are the rated power flows to limit-test the MMC. This implies that the submodules are assumed to be in one of the three submodule states derived in the previous section irrespective of the necessary submodule modes. The only assumption is that the states are not restrained by the BESS limits. This approach lets us efficiently test the connectivity.

4.6.2 Case Definitions

8 cases are defined to test the connectivity of the MMC. The first case is a simulation of the rated MMC operation and is done as a benchmark to the other simulations. Then the MMC operation for different power mismatch scenarios are investigated in case 2 to 4: phase imbalance in case 2, arm imbalance in case 3, and imbalances appearing simultaneously in case 4. Then a scenario that tests the submodule voltage balancing algorithm is done in case 5. In case 6 a scenario where the MMC is a load converter is done to investigate power flowing in the load direction. After the Load Submodule states have been investigated, they are combined with Source Submodules to create a mixed power flow between two arm in case 7. Finally, in case 8 the maximum mixed intra-arm power flow is investigated by inserting Load Submodules in an arm dominated by Source Submodules.

The cases are illustrated in Figure 4.10. In the figure each case is displayed by showing a simplified MMC circuit where each arm is lumped to one equivalent submodule. The color of the lumped submodules indicates which state the submodules are in. Convenient definitions for the MMC parts are also introduced in the figure. Each arm is given a name “PL” depending on the phase P and location of the arm L, for example AL refers to the lower arm of phase a. The submodule of an arm is also given a number as in AL12 being the last submodule of arm AL. AL in case 8 has a gradient color to indicate that different numbers of Load Submodules are tested.

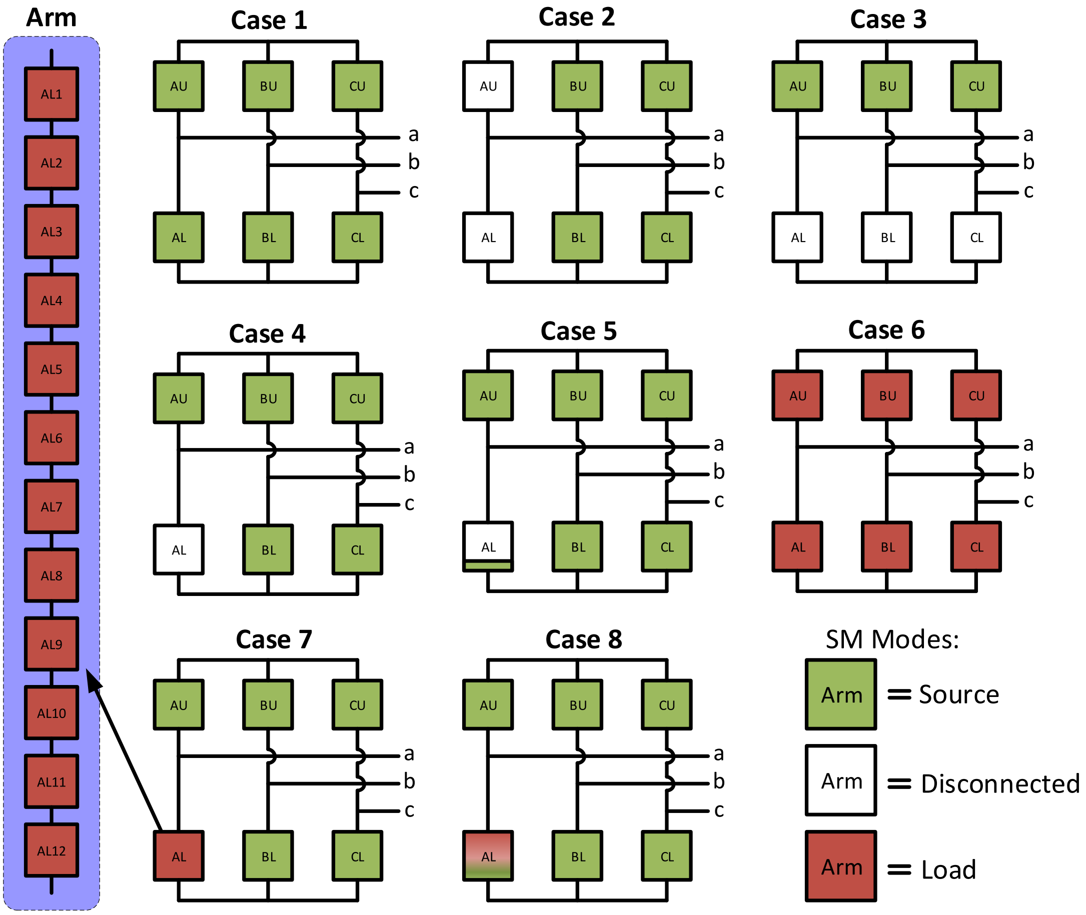

Figure 4.10: Visualization of the MMC simulation cases

4.7 Case Simulations

4.7.1 Case 1: Rated Generation

Case 1 is simulating a scenario with rated conditions to provide a reference basis. The case has only arms with Source Submodules. In other words, each BESS has an available SOC to locally balance the PV power to a constant submodule power output. Furthermore, the submodule voltages are easily balanced so no second-ordered harmonics are injected. This case is used to investigate the behavior of the MMC and find typical values for the MMC variables: the grid current, the arm currents and voltages, submodule power flows, and the submodule voltages. Figure 4.11 shows the results from the simulation of case 1.

First of all, from Figure 4.11a-4.11b, it can be observed that the MMC is capable of delivering balanced power with good grid quality. The grid currents in Figure 4.11a are balanced. They are also in phase with the grid voltages which demonstrates that power is delivered to the grid. The phase current and phase voltage amplitudes are measured to be 125 A and 326 V. This is calculated to produce a total of 61 kVA which is approximately the rated power of the converter. The power is found to satisfy the grid requirements in Figure 4.11b indicated by the red asterisks: the CUF is 0.03 % and the TRD is around 0.8 % for all phases. These values are small indicating the overall good performance of the converter.

Secondly, the internal oscillations can be explained by figures 4.11c-4.11f. The arm currents in Figure 4.11c are pure sinusoidal waveforms of the fundamental frequency as seen by the 0.20 ms period between two peaks. The arm currents have an amplitude of 62 A which shows that the grid current is evenly divided between the arms. Usually, when the MMC is used as a HVDC converter, the arm currents would contain a DC component as well, but this component is negligible as seen in the frequency spectrum of the circulating current in Figure 4.11d. This is because the DC power sources comes from the submodules instead of a common DC link.

Interestingly, the AC component in the arm currents makes the submodule voltages in Figure 4.11e to oscillate with a fundamental frequency component. The oscillations are well within the voltage limits having only a size of 7 V as seen in the submodule voltage frequency spectrum in Figure 4.11f. In HVDC and other applications with a common DC link, these voltages normally oscillate with a second harmonic component [26]. To find the reason for the different oscillations a frequency analysis of the dynamic capacitor equations is needed. This can be done with the Σ-Δ state-space representation by looking at the frequencies in the two components of the capacitor voltage: v_c^Σ and v_c^Δ. The governing equations for these components are repeated below with highlighted frequency groups:

$$C\frac{dv_c^\Sigma}{dt} = \overbrace{n^\Sigma i^\Sigma}^{\text{DC}+2\omega} + \frac{1}{2}\overbrace{n^\Delta i^\Delta}^{\text{DC}+2\omega} + \overbrace{i^\Sigma_{DER}}^{\text{DC}} \tag{4.18}$$

$$C\frac{dv_c^\Delta}{dt} = \overbrace{n^\Delta i^\Sigma}^{\omega+3\omega} + \frac{1}{2}\overbrace{n^\Sigma i^\Delta}^{\omega} + \overbrace{i^\Delta_{DER}}^{\text{DC}} \tag{4.19}$$

Here the frequency components due to the DC and second harmonic components in HVDC applications are highlighted with red. The modulation indexes n^Σ and n^Δ can be assumed to be approximately 1 and $cos(\omega t)$ respectively.

The fundamental frequency oscillations of the submodule voltages can be explained by the lack of a DC component in the arm currents. Since there is no DC component, no second harmonics in the circulating current are induced by the circular dependence either. Therefore, a significant contribution to the second harmonic in the capacitor voltages is omitted. It can be seen in (4.18) that a second harmonic is created in the capacitor voltage sum even for link-less MMCs. However, this component must be negligible compared to the second harmonic component created by the HVDC in the first term. From (4.19) the source of the sinusoidal component can be seen to come from the product of n^Σ and i^Δ.

Finally, the modulation procedure and modulation results are shown in Figure 4.11g-4.11h. Figure 4.11g shows the power flow of an arbitrary submodule in AU. The power flow is seen to be consistent with the arm current. When the current is positive the

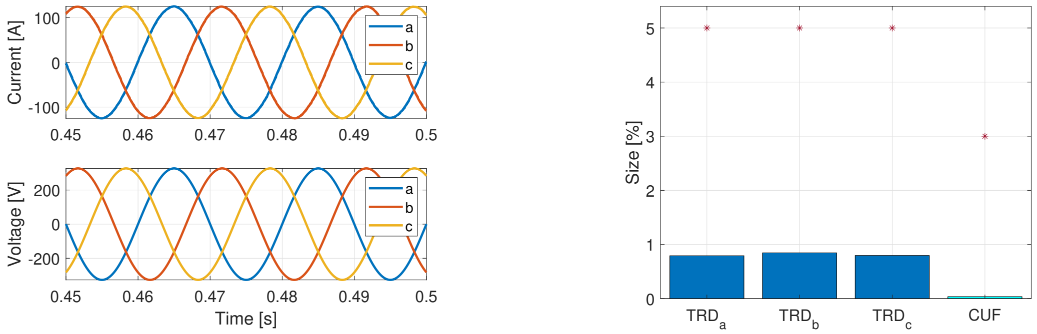

(a) Grid current and voltage (b) Grid indicators

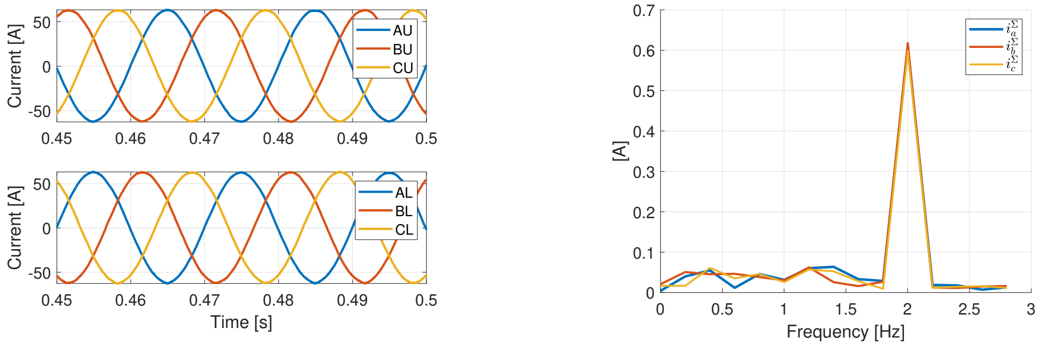

(c) Arm currents (d) Frequencies of circulating currents

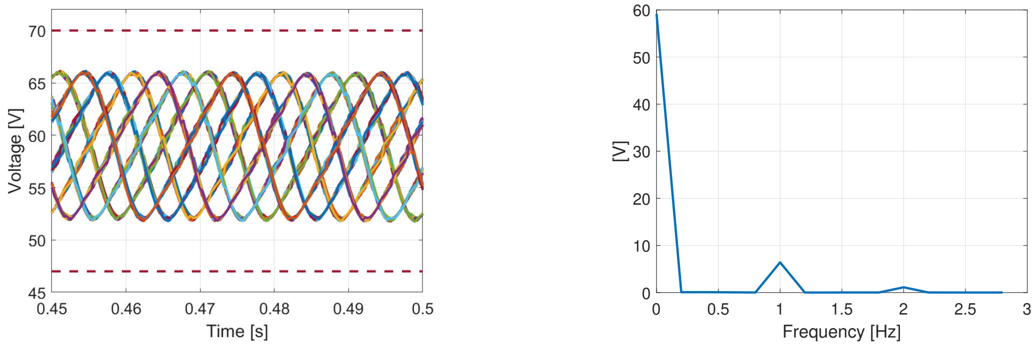

(e) Submodule voltages (f) Frequencies of submodule voltage

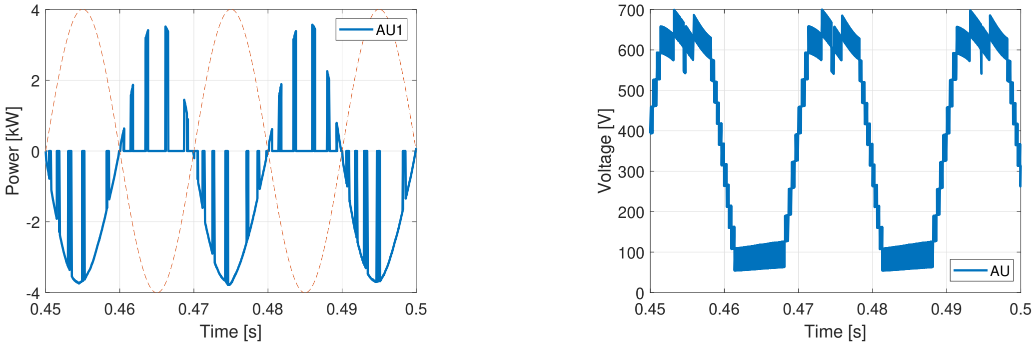

(g) Power into submodule (h) Upper arm voltage in phase a

Figure 4.11: Simulation results of case 1: rated generation

power flows into the submodule and when it is negative the power flows out. The power flow is also intermittently interrupted when the submodule is bypassed in the arm. This causes no power to flow in the submodules.

It can be seen that the submodule is inserted more for negative currents. This is because of the modulation of the upper arm voltage which can be seen in Figure 4.11h. The arm voltage reference is added to Figure 4.11g in stippled red lines as well to better visualize when the submodules are inserted. As a result of the modulation reference, more submodules need to be inserted when the arm current is negative. The result is that the submodule is discharged more than it is charged even though the current is balanced around the zero-current-axis. Keep in mind, this is not by chance, but occurs as a direct consequence of controlling the arm current to be in phase with the grid. Finally, it can be noted that the arm voltage in Figure 4.11h is slightly distorted due to the third harmonic components added to allow for overmodulation in the MMC.

4.7.2 Case 2: Phase imbalance

Case 2 is simulating the first type of imbalance to be studied: the phase imbalance. The imbalance is set to occur due to phase a having only Disconnected Submodules while the submodules of phase b and c are Source Submodules. This imbalance can occur when the irradiance received by phase a is reduced over longer periods depleting the batteries so the low PV power produced cannot be compensated. However, it can also occur simply because the batteries are disconnected to preserve their SOC. The results in Figure 4.12 demonstrates the behavior of the MMC during phase imbalances and how it compensates to balance the MMC internally to provide balanced power. The case is simulated with no second harmonic injection.

The MMC performance according to the KPIs is found to be satisfactory. The waveforms of the grid currents in Figure 4.12a are balanced and without distortions. The grid current at 81 A is reduced to two-thirds of the current in case 1. This corresponds with the loss of power compared to the MMC in case 1. There is a small increase in the TRD values in Figure 4.12b, but they are well within the limits. The CUF, however, experiences a significant increase compared to case 1 with a value of 1.2 %. The horizontal balancing has evidently a large impact on the CUF.

The controller is producing DC current components to tackle the phase imbalance. Phase a is constantly delivering power to the grid without getting any from its submodules and needs to be replenished by the other phases. As seen in Figure 4.12d, two equally sized DC currents is flowing to provide phase a with active power. This gives phase a a DC current of 20 A which is twice the size compared to the other phases. The arm currents in Figure 4.12c are therefore shifted. The DC components cause current offset deficiencies since the current is less able to discharge Source Submodules. However, there are only Disconnected Submodules in phase a so the submodule voltages (not shown) is found to oscillate with a fundamental frequency within their limits. It can also be noted that the grid current is seen to be equally distributed between the arms.

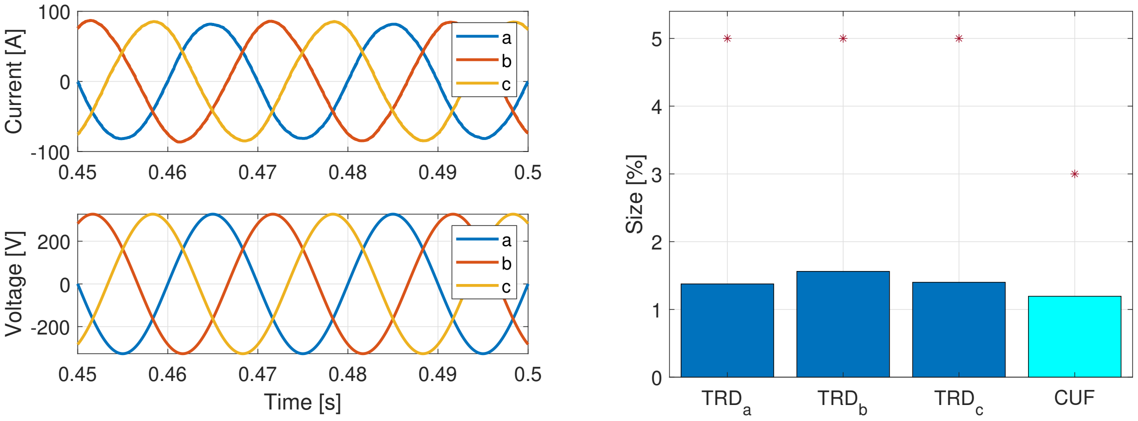

(a) Grid current and voltage (b) Grid indicators

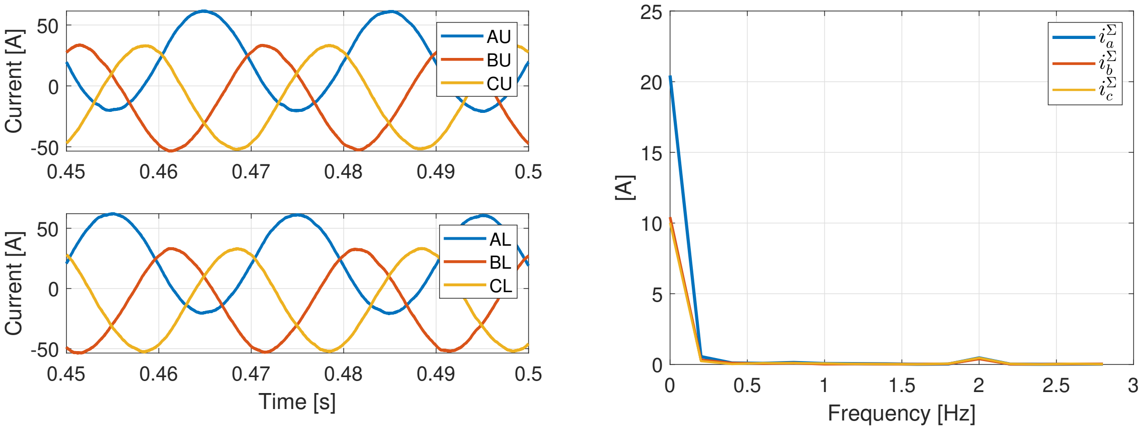

(c) Arm currents (d) Frequencies of circulating currents

Figure 4.12: Simulation results of case 2: phase imbalances.

4.7.3 Case 3: Arm Imbalance

Case 3 is investigating the second type of imbalance: the arm imbalance. A scenario is created where the upper arm submodules are set as Source Submodules while the lower arm submodules are set as Disconnected Submodules. The cause of the imbalances can be the same as in case 2, but now they have occurred other places in the MMC compared to case 2. The results of the simulation of case 3 in Figure 4.13 aims to show the impact of the vertical imbalances and how the MMC behaves to compensate them. No second harmonic injection is used.

The MMC performance is similar to the performance in case 2 except its more balanced. The grid current in Figure 4.13a has a pure sinusoidal shape which is confirmed by the low TRD values in Figure 4.13b: all phases have a TRD around 1.7 %. The slightly higher TRDs are reasonably since an odd-ordered component, the fundamental frequency component, is forced into the circulating current. This introduces odd-ordered harmonics in the Σ-variables. The CUF, however, is reduced to a negligible size of 0.1 %. Evidently,

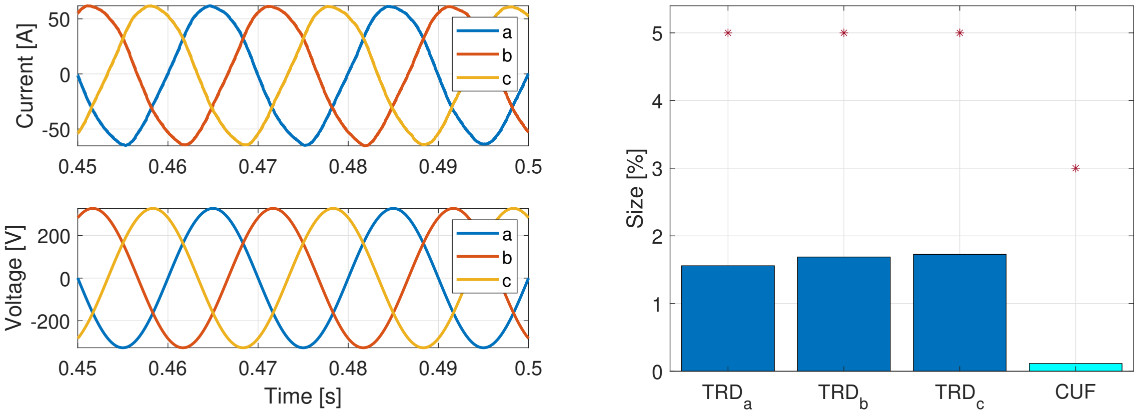

(a) Grid current and voltage (b) Grid indicators

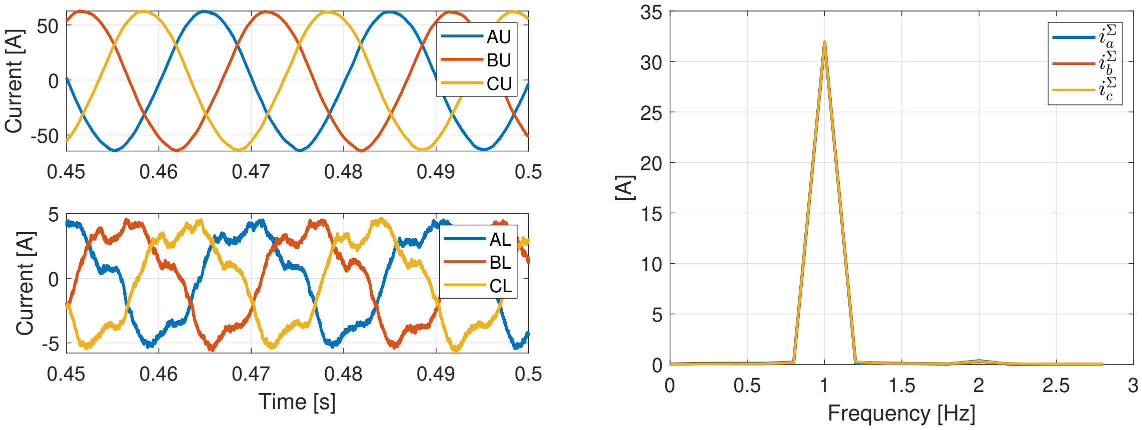

(c) Arm currents (d) Frequencies of circulating currents

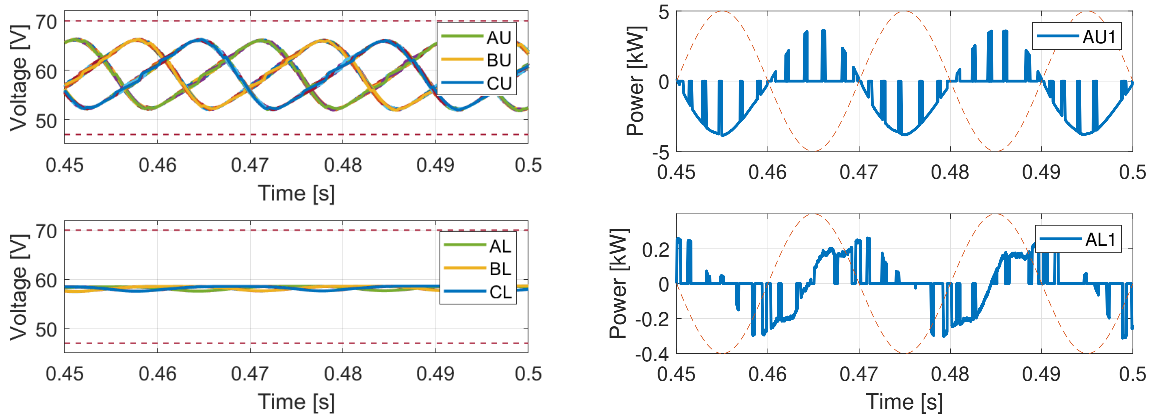

(e) Submodule voltages (f) Power into submodule

Figure 4.13: Simulation results of case 3: arm imbalance

the CUF is not influenced by vertical balancing which is natural since the generated power in the phases are balanced. The grid currents have a peak of 62 A because only half of the rated power is produced.

The circulating current has a fundamental frequency component to compensate for the power deficit in the lower arms. This component is seen in Figure 4.13d to have a necessary size of 32 A for all phases. It is seen to affect the distribution of the grid currents in the arms as seen in Figure 4.13c. The compensating current is seen to match the phase of the upper arm currents, or in other words, in opposite phase of the lower arm currents. As a consequence, the grid current and the compensating circulating current equalize each other in the lower arms. Moreover, the upper arm currents are increased in magnitude and must support the grid currents alone. The resulting current in the lower arms are seen to have only a negligible size of 4 A, phase-shifted and with visible distortions. However, it is found through fast Fourier transforms that the magnitudes of the distortions are the same in the upper and lower arms, but appear larger in the lower arms relative to the small current size.

The reduced current magnitude in the lower arms can lead to current magnitude deficiency in the submodule voltage balancing. The power flow in AL1 in Figure 4.13f is seen to support only power flows up to 200 W. However, in this case the arms with the reduced arm currents have only Disconnected Submodules. The voltage balancing is therefore successful in this case as seen for the submodule voltages in Figure 4.13e. They are all found to be within their limits. Moreover, the lower arm submodules are observed to have very little oscillations which highlights the oscillations' dependency on the arm current sizes.

4.7.4 Case 4: Phase and Arm Imbalance

Previously, two of the possible imbalance types have been investigated. This time, in case 4, the imbalances are set to occur simultaneously. This is to investigate if the behavior of the MMC can be regarded as a superposition of the behaviors of case 2 and 3 or if they somehow resonate with each other causing unforeseen issues. A scenario where all arms except AL have Source Submodules is investigated. AL has only Disconnected Submodules. Still, no second harmonic components are injected in the arm current.

The MMC is capable of handling both imbalances simultaneously. The grid currents are balanced and in phase with the grid voltages as seen in Figure 4.14a. The grid current peaks at 100 A which correlates with the reduction of power due to the missing generation. Figure 4.14b shows that the TRDs are kept below 1.5 %. The highest TRD is in phase *a* which is the source of the imbalance. The CUF value of 0.5 % is in between the values of case 2 and 3.

The arm currents in case 4 are more complex, but is only a superposition of the components that occurs in case 2 and 3. Figure 4.14c shows that the AU arm current stand out having both higher amplitudes and a more significant DC component. Figure 4.11d

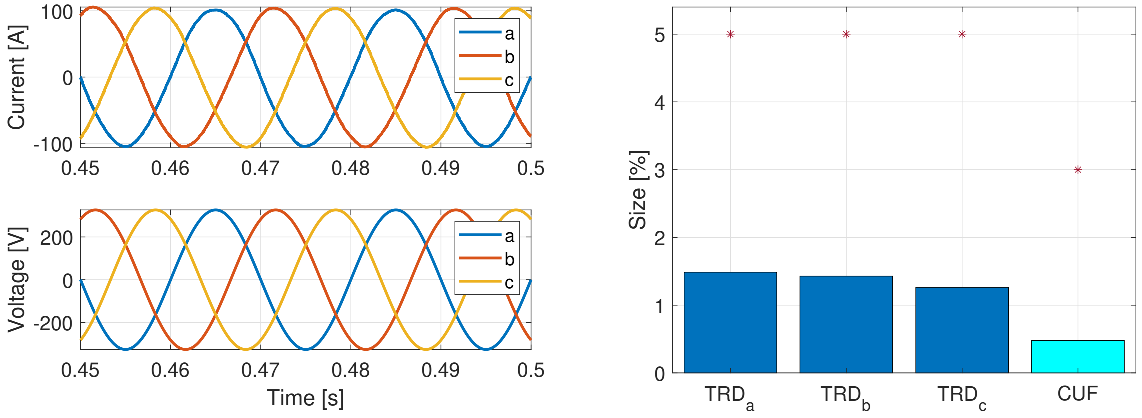

(a) Grid current and voltage (b) Grid indicators

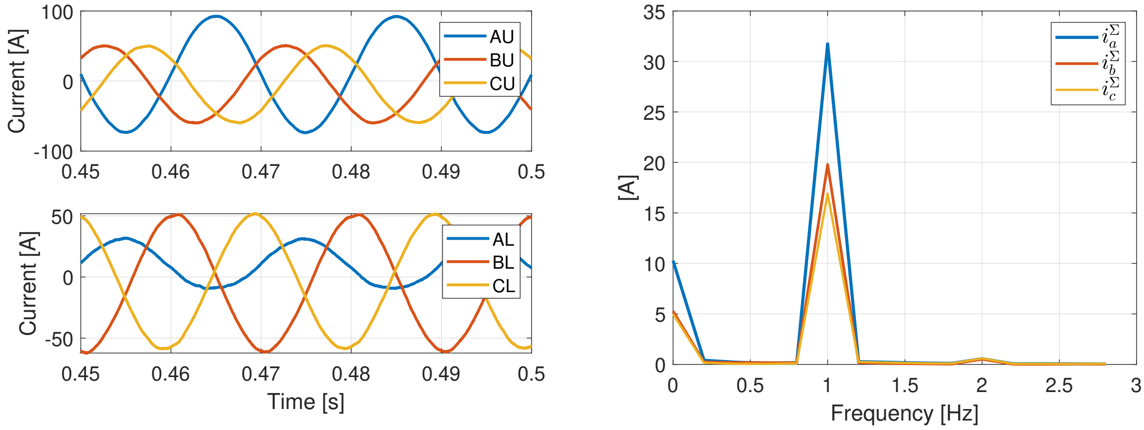

(c) Arm currents (d) Frequencies of circulating currents

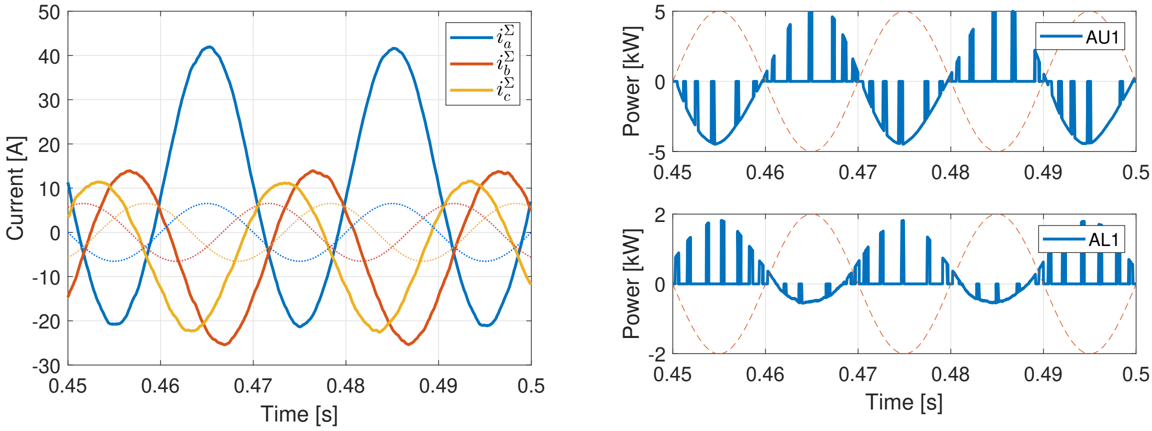

(e) Circulating currents (f) Power into submodule

Figure 4.14: Simulation results of case 4: phase and arm imbalance

confirms that the circulating current in phase a consists of a higher DC and fundamental harmonic components than the other phases. The components correspond to the power mismatches; the fundamental frequency component at 31 A is the same as in case 3, but the DC component is halved to 10 A compared to case 2. It is observed fundamental frequency components in phase b and phase c even do these phases have no arm mismatches. These components are purely reactive as seen by their phase shift relative to the stippled arm voltages in Figure 4.14e. The result is that these harmonic components transfer no active power in the balanced phases, but the sum of the fundamental harmonic components is forced to zero.

All the submodule voltages (not shown) are balanced and within their regions despite the unbalanced generation. All the arms with Source Submodules have submodules voltages with the characteristic fundamental frequency component while arm AL has submodule voltages with barely any oscillations as observed for the lower arms in case 3. Despite the balanced submodule voltages, it can be seen from Figure 4.14f that the balancing is reaching a critical point because of arm current magnitude and offset deficiencies. The power flow is barely negative because of the DC term from the horizontal balancing and the reduced arm current magnitude because of the vertical balancing. The AL arm current has only amplitudes of 25 A. However, it has no effect on the submodules in AL since they only are Disconnected Submodules.

4.7.5 Case 5: Submodule Imbalance

Case 5 builds upon case 4 by adding uneven power generation between the submodules within arm AL. The scenario in case 4 does not only have the smallest imbalances so far, but showed also to be the hardest to balance. This was because the power mismatch compensation techniques weakened the arm current for submodule voltage balancing. It is, therefore, interesting to examine uneven generation within an arm in the worst-case scenario provided by case 4.

Case 5 has all arms except AL with only Source Submodules. AL, on the other hand, has only Disconnected Submodules except for the last submodule in AL, AL12, which is set as a Source Submodule. This enables the submodule imbalances to be investigated while the case is approximately similar to case 4. AL12 has to be discharged substantially more than the other submodules due to the added submodule current inflow. The weak arm current is expected to struggle with the balancing. However, the case was first simulated without a second harmonic injection to observe the MMC performance.

Case 5 With No Harmonic Injection

Only the grid performance of the MMC is unaffected compared to case 4. The grid currents are found to be balanced and the indicators are the same as in case 4. Moreover, the arm currents have approximately the same waveforms with the same harmonic components: a DC and a fundamental harmonic component. Figure 4.15a, however, shows that AL12, showed in green, is outside the KPI limits. The other submodules, however, are within the limits, but just barely above the lower limit. As anticipated, submodule AL12 in Figure 4.15b is always discharging when possible, but it is not sufficient causing the capacitor to be charged unbounded by the submodule current. This causes the other submodules voltages in AL to be reduced below the rated values to make sure the sum is equal to the rated arm voltage. This scenario shows the importance of the submodule voltage KPI since balanced power can be delivered to the grid even if the internals of the MMC are uncontrolled.

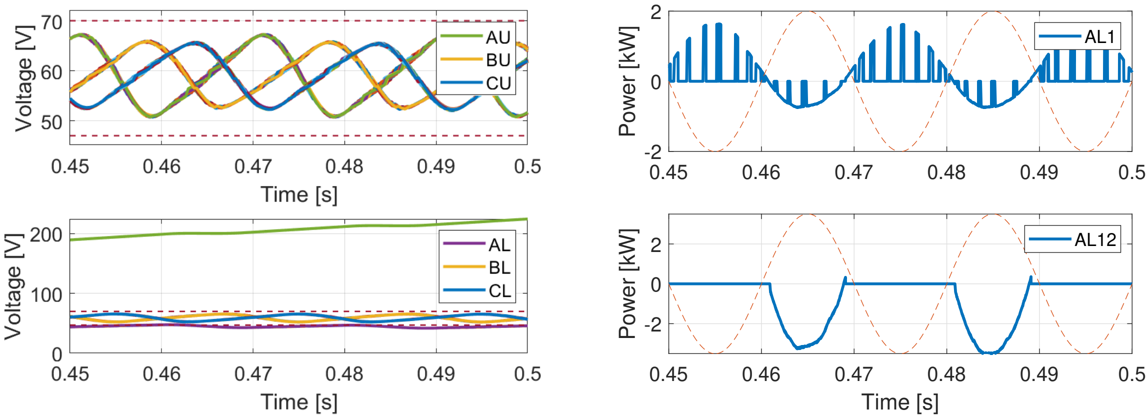

(a) Submodule voltages

(b) Power into submodule

Figure 4.15: Simulation results of case 5: submodule imbalance without second harmonic injections

Case 5 With 0.45 p.u. Harmonic Injection

A second harmonic is injected to balance arm AL in case 5. Several injections were tested and it was found that an injection of 0.45 p.u. was necessary to balance the submodule voltages. This causes the submodule voltages in Figure 4.16e to be within their limits. The balancing is operating at its maximum capacity as is seen by the green voltage of AL12 not fully managing to follow the other submodule voltages of AL. In addition, the injection causes all the submodule voltages to oscillate with a second harmonic component in addition to the fundamental frequency component.

The harmonic injection makes the arm current more suited for the submodule balancing algorithm. This is because the second harmonic injection of 56 A as seen in Figure 4.16d is significantly larger than the original arm current. This makes the arm current in Figure 4.16c large enough to discharge AL12. The power flows in Figure 4.16f is seen to reach 4 kW. In addition, the second harmonic component brings more negative parts in the arm currents that the source submodule can discharge of.

The harmonic injections, however, are disadvantageous for the grid performance of the MMC. The currents in Figure 4.16a are balanced and visibly pure from harmonics. The

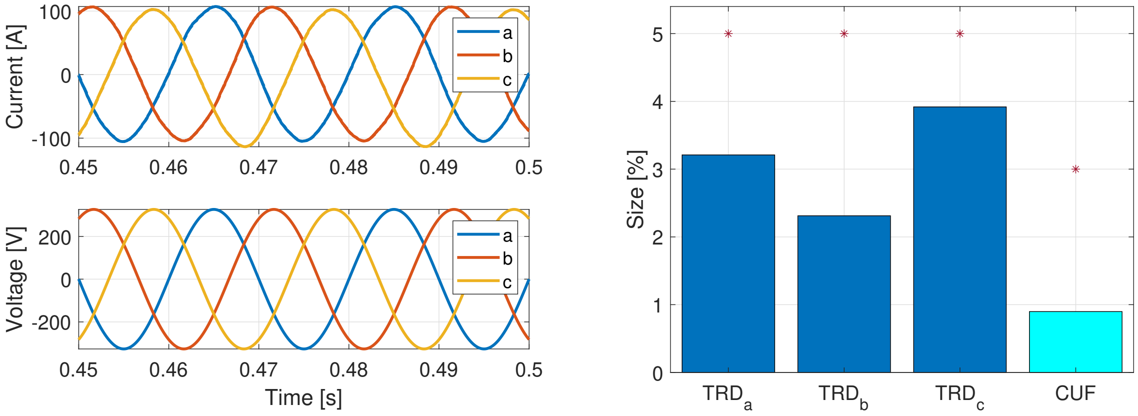

(a) Grid current and voltage (b) Grid indicators

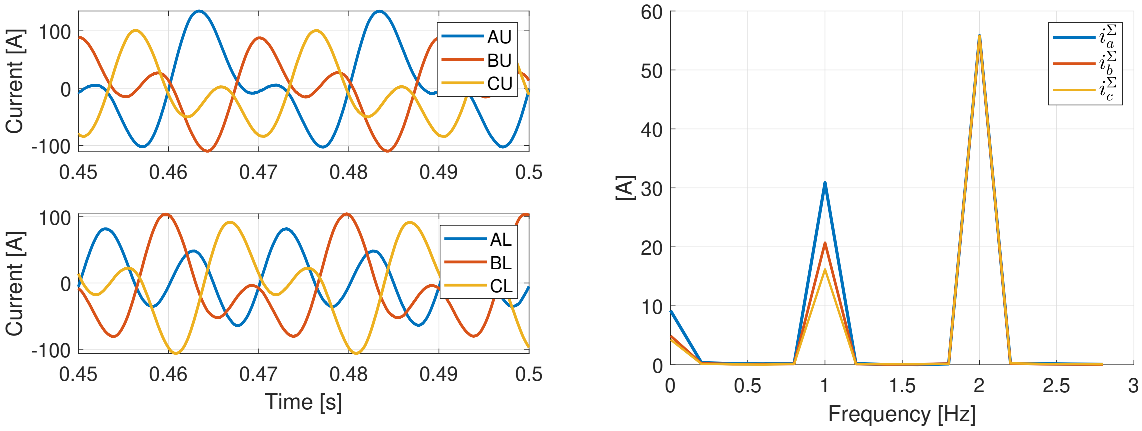

(c) Arm currents (d) Frequencies of circulating currents

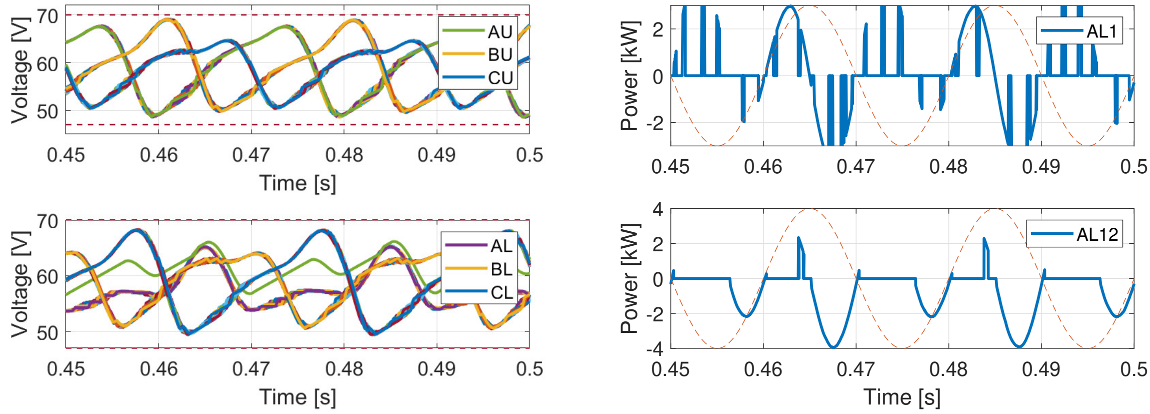

(e) Submodule voltages (f) Power into submodule

Figure 4.16: Simulation results of case 5: submodule imbalance with 0.45 p.u. second harmonic injections

CUF of 0.9 % in Figure 4.16b is still relatively low, but the TRDs are significantly higher. The TRDs are as high as 3.9 %, but still within the TRD limits. The distortion is also seen to distribute unevenly between the phases. Surprisingly, phase *c* is the phase with the most distortions.

4.7.6 Case 6: Rated Loading

So far no submodules have been set as Load Submodules. Load Submodules can, however, become both necessary and useful for the operation of the MMC. They are an essential part of the BEMS which can provide ancillary services or improve the MMC efficiency. To better understand the MMC during loading conditions, case 6 is examining the MMC with only Load Submodules. The case is run without a second harmonic injection.

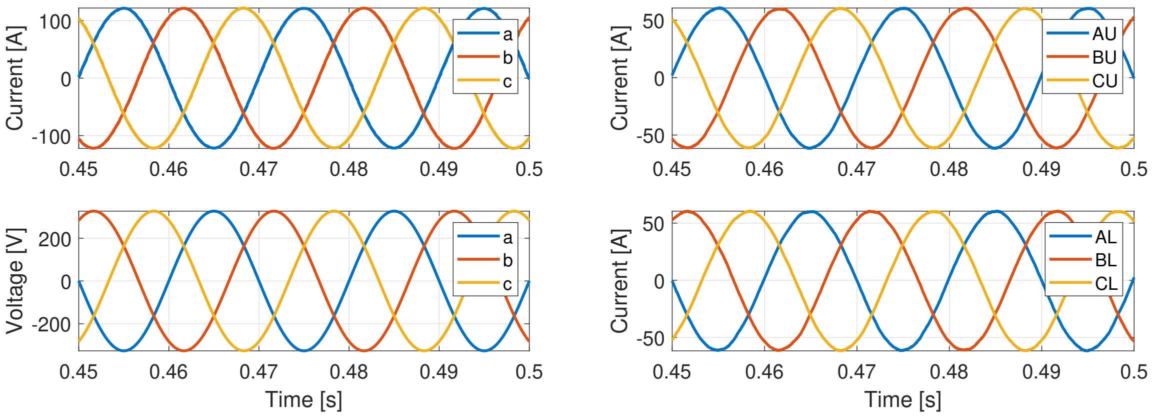

(a) Grid current and voltage

(b) Arm currents

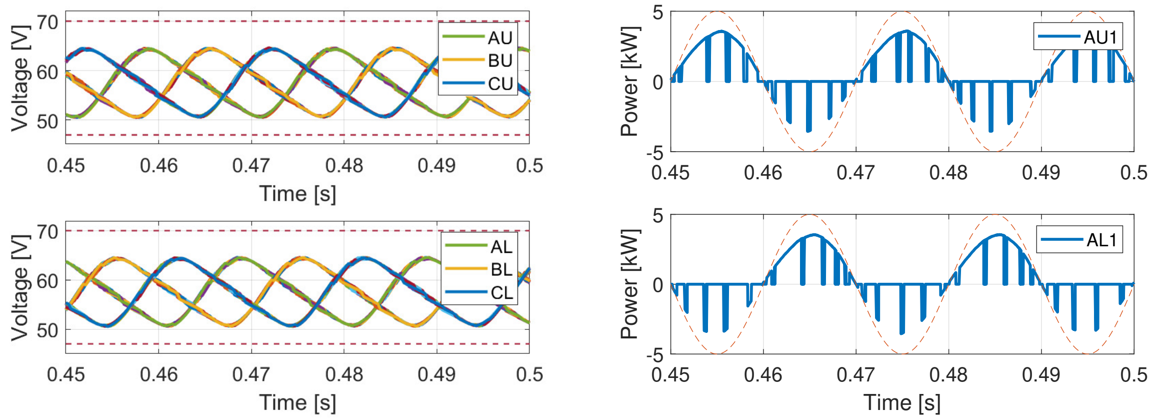

(c) Submodule voltages

(d) Power into submodule

Figure 4.17: Simulation results of case 6: rated loading

The grid is found to be very little affected by the MMC operating as a load. The grid in Figure 4.17a is purely sinusoidal and the indicators (not shown) are the lowest recorded of all the cases. The CUF is negligible with only 0.1 % while all the TRDs are 0.7 %. The grid current is seen to be in opposite phase of the grid voltage indicating that power is flowing to the MMC. The grid current is evenly distributed between the arms with an amplitude of 60 A.

The MMC behaves as anticipated. The submodule voltages in Figure 4.17c are within the specified KPI limits. They oscillate with the familiar fundamental frequency components characteristic for the sinusoidal arm currents (not shown). The phase shift in the arm currents causes more power to flow into the submodules; the average power flows for both upper and lower arms in Figure 4.17d are positive since the positive part of the arm current is in phase with the positive modulation peaks.

4.7.7 Case 7: Mixed Arm Power Flows

So far Source Submodules and Load Submodules have never been tested simultaneously. This, however, is now included in case 7. In this case the submodules of AU are set as Source Submodules and the submodules of AL is set as Load Submodules. No intra-arm mixed power flows are present. This lets us focus on only the vertical and horizontal balancing during the mixed power flows.

The case can describe several real scenarios. In general it resembles a scenario where arm AL is receiving reduced irradiance and the BESS is set to absorb power. The power absorption can come from a need to perform voltage support or peak shaving for the grid. What is more, the scenario shows how an entire arm can be used to perform online battery specific services. One such task can be online estimation of battery parameters such as SOH [49]. It can also be used for a soft reset of the BESS while the MMC is still operating, that is, charge the batteries to equalize or increase the SOC for future demands.

The case is seen to create an acceptable MMC operation. The grid current in Figure 4.18a are balanced with an amplitude of 87 A. The indicators in Figure 4.18b are relatively high, but within the limits. The submodule voltages in Figure 4.18e are also within the limits. The scenario can therefore by supported according to the grid standards.

The arm currents are severely affected by the power mismatches. Since the net produced power in phase a is zero, the phase a DC compensating current in Figure 4.18d is 20 A as in case 2. Additionally, due to the large vertical power imbalance of 2 p.u., a fundamental frequency component of 63 A is created. It is twice the size as in case 3 where the vertical power imbalance only was 1 p.u.. The fundamental frequency current is so large that the AL arm current in Figure 4.18c becomes a load current with amplitudes of 20 A, that is, it is in phase with the lower arm voltage as in case 6. On the other hand, the AU arm current becomes significantly larger. Its amplitude of 107 A is sufficient to solely support the grid and compensate the load current of AL. Together with the DC component the AU arm current reaches peaks of 127 A. Additionally, the AL arm current is never negative since the DC offset is the same size as its amplitude.

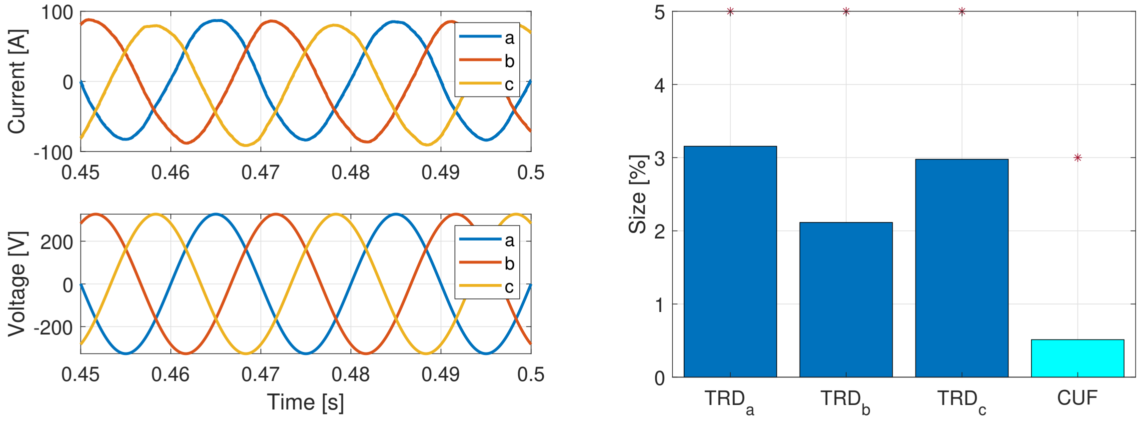

(a) Grid current and voltage (b) Grid indicators

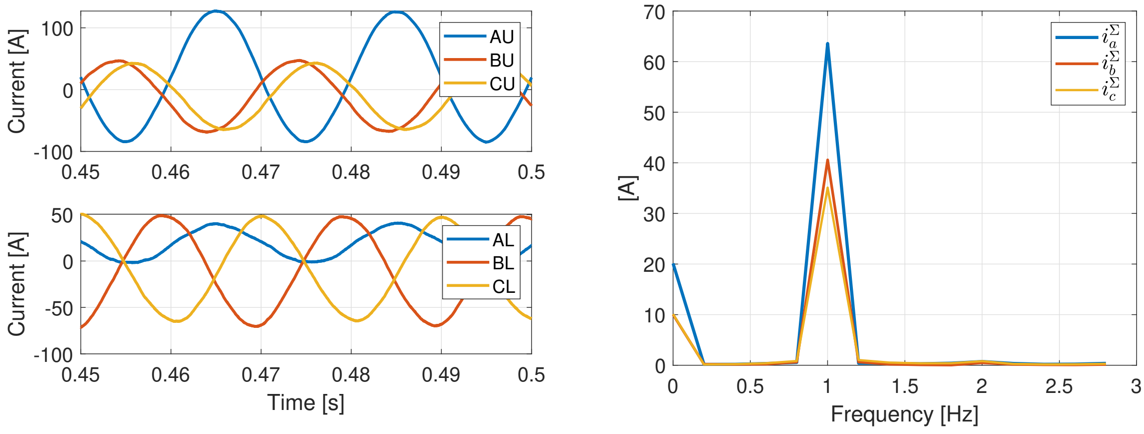

(c) Arm currents (d) Frequencies of circulating currents

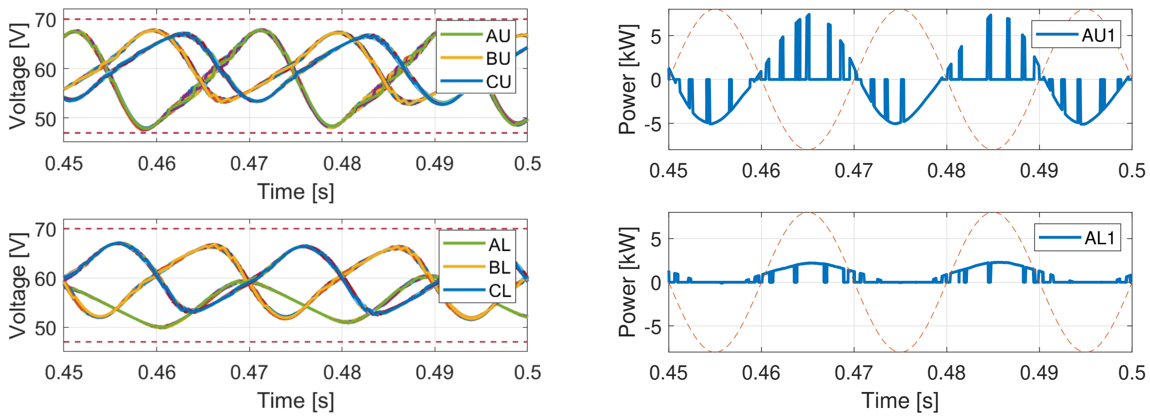

(e) Submodule voltages (f) Power into submodule

Figure 4.18: Simulation results of case 7: mixed arm power flows

The arm current shape affect the submodule power flows as seen in Figure 4.18f. The AU submodules have high power flows due to the large AU arm current. This makes the submodules in AU easier to balance. The AL submodules, however, has both a small amplitude and a large DC offset. In fact, the AL arm current is never negative making it unfit for balancing of Source Submodules. However, there are only Load Submodules in AL and consequently the submodules should be balanced. This is confirmed by Figure 4.18e where all submodule voltages are seen to be balanced. It can be seen that the phase a submodule voltages oscillate less in AL and more in AU than compared to the other submodule voltages. This corresponds to the arm current sizes of AL and AU.

4.7.8 Case 8: Maximum Mixed Intra-Arm Power Flow

Case 7 introduced mixed arm power flows in the MMC. It was discovered that the arm currents were severely affected which could impact the submodule balancing. Both mechanisms for current magnitude and offset deficiency was observed. However, mixed intra-arm power flows were not present in case 7 and, therefore, the converter did not struggle with the submodule balancing. Mixed intra-arm power flows is now investigated closer in case 8. In addition to the observed deficiencies, the submodule balancing is anticipated to struggle with current phase deficiencies as well. Therefore, not all combinations of mixed intra-arm power flows are anticipated to be stable.

Case 8 tries to investigate what combination of mixed intra-arm power flows are sustainable and to identify the maximum number of Load Submodules than can be inserted. Since the converter is considered to struggle, the maximum allowable second harmonic component is injected. Through testing this is found to be around 0.75 p.u. Beyond this value the arm currents are so large that the submodule voltages are oscillating more than the acceptable submodule voltage KPI limits.

The identification of the maximum mixed intra-arm power flows are important to properly set the BDEMS limits in the EMS. There might be scenarios that would cause or benefit from mixed intra-arm power flows. If the irradiance is unevenly spread across the submodules of one arm, the power generated from the submodules might differ significantly. If the BESSs are set to absorb a power that is in-between the range of the submodules producing the least and the submodule producing the most, the arm will experience a mixed intra-arm power flow. It is then important to know how much mixed power flow the arm can handle or if it needs to prioritize the charging of some submodules more than other to handle it. In general, the case is also interesting to identify what mechanisms is causing improper submodule balancing.

Location of Maximum Mixed Intra-Arm Power Flows

The maximum mixed intra-arm power flows is found by doing a sweep of the number of Load Submodules. An arm originally dominated by Source Submodules is simulated with increasing number of Load Submodules and the KPIs and arm current components of each case are noted. The results are shown in Figure 4.19. It must also be mentioned that Load Submodules with power flows below the rated power have been investigated. It was found that if the load power reference was reduced to 0.2 p.u., any combination of mixed power flow could be sustained for stable MMC operation.

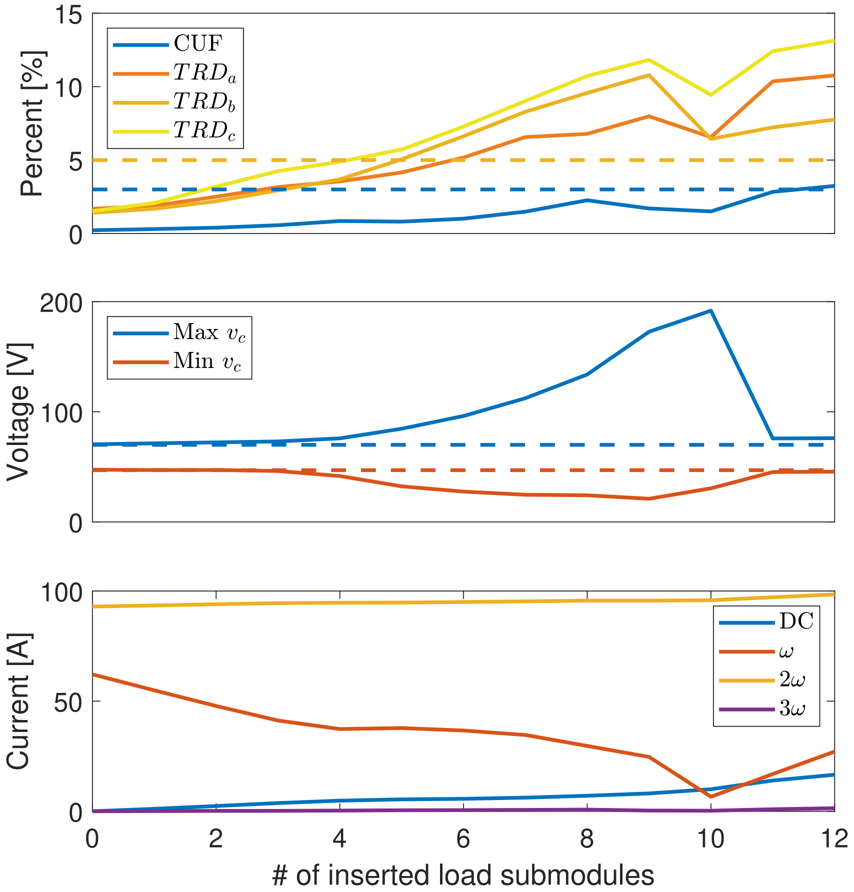

Figure 4.19: Sweep of mixed intra-arm power flows with 0.75 p.u. second harmonic injection

The KPI indicators are seen to steadily increase with the number of inserted Load Submodules in the upper figure of Figure 4.19. It is seen that only 4 Load Submodules can acceptably be grid-connected before the TRDs are exceeding the recommended grid specifications. Even beyond 4 Load Submodules the TRDs are increasing at a steady rate. The only exception is at 10 Load Submodules where all the TRDs experience a significant drop. The CUF is also steadily increasing, but is never beyond its limit. Overall, the indicators increase with higher power mismatches.

However, the most severe influence is seen in the maximum and minimum of all the submodule capacitor voltages in the middle figure of Figure 4.19. It is seen that only 3 Load Submodules can be sustained before one of the submodule voltages exceeds the voltage limits. Both minimum and maximum limits are exceeded, but the largest deviances are found in the maximum values. The highest maximum is 191 V for the scenario where 10 Load Submodules are inserted. Both the maximum and minimum voltages deviations increases until this point. Beyond, however, for 11 Load Submodules, the arm is finally able to balance the capacitor voltages again.

The submodule balancing issues can be understood by investigating the arm current components in the lower figure of Figure 4.19. The second harmonic component is seen to have almost a constant magnitude and can not be the cause for the unbalanced submodules. Higher frequency components such as the third harmonic components are negligible. The balancing issues must, therefore, be caused by the change in the DC or the fundamental frequency components. These components must range between the values found for no Load Submodule as in case 1 and for only Load Submodules as in case 7.

The submodule balancing is strained already from the first present Load Submodule. When an MMC is producing a net positive power, the grid currents are going to be in phase with the grid voltage. This means that the arm currents will be in opposite phase of the arm voltages which prioritizes discharging of the submodules. If then one or a few Load Submodules are present, they will experience current phase deficiency. This has not been present in the cases so far, but is a characteristic feature of mixed intra-arm power flows.

However, the effect of this deficiency is reduced as more Load Submodules are inserted. With more Load Submodules, the power mismatch increases, more compensating currents are created and the arm current becomes more favorable for the Load Submodules. More Load Submodules increases the horizontal imbalance and as seen in the lower figure in Figure 4.19 this gives a higher DC component. This component makes the arm current more positive which is good for charging of the Load Submodules. More Load Submodules increases the vertical imbalance as well and a fundamental frequency component is injected to balanced it. This component reduces the arm current magnitude in AL as seen for the fundamental frequency component in the lower figure of Figure 4.19.

Despite the more favorable load conditions, the submodule voltages becomes uncontrolled for more than 3 Load Submodules. This could be a consequence of the duality in mixed intra-arm power flow balancing. If the conditions for Load Submodules are improved, the conditions for Source Submodules are worsened. As the Source Submodules becomes the minority in the arm and the conditions worsen for the Source Submodules, the maximum voltages are increasing, reaching a maximum at 10 Load Submodules. At 10 Load Submodules the fundamental frequency component in the arm current has been almost entirely compensated by the circulating current and the current is at its lowest. On the other hand, the low current seems to have a good influence on the grid since the number coincides with the drop in the grid indicators. For more than 10 Load Submodule the circulating current compensation is larger than the original arm current and the current increases in size, but as a load current such as in case 7. This is beneficial for all the Load Submodules, but creates a current phase deficiency for the last Source Submodule. Nevertheless, the submodules are managed to be balanced with 11 Load Submodules.

Simulation of Maximum Mixed Intra-Arm Power Flows

The maximum mixed intra-arm power flows are plotted in Figure 4.20. This is both to better show the behavior of the MMC for maximum mixed power flow, but also to investigate the reason that 4 Load Submodules cannot be sustained. The maximum mixed power flow was found to be with 3 Load Submodules (AL10, AL11 and AL12).

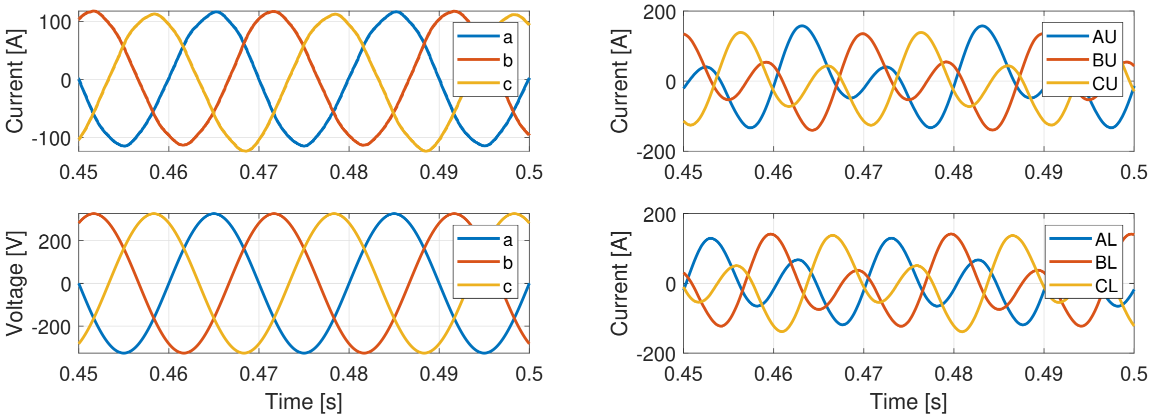

(a) Grid current and voltage (b) Arm currents

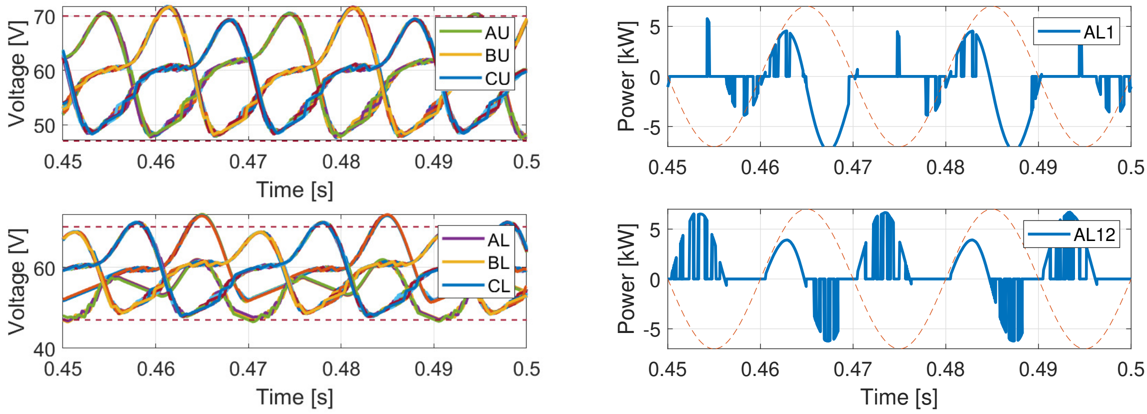

(c) Submodule voltages (d) Power into submodule

Figure 4.20: Simulation results of case 8: maximum mixed intra-arm power flows

The grid performance of the MMC is within the limits. The grid currents in Figure 4.20a are looking pure, balanced and in phase with the grid voltages. The grid indicators (not shown) are similar to the ones of case 5 with second-ordered harmonic injection: TRDs between 2 and 4 % and a CUF of 0.6 %. The components of the circulating current in phase a are found to be: a 4 A DC component, a 16 A fundamental frequency component and a 93 A second-ordered harmonic component. The components have the expected sizes considering the unbalanced generation. The AL arm current in Figure 4.20b is seen to be dominated by the second harmonic injection.

The internal states are found to operate at the maximum capacity. The submodule voltages in Figure 4.20c have large oscillations due to the high arm currents. The submodule voltages are seen to sometimes exceed the limits. The power flows of the submodules of AL in Figure 4.20d are large enough and have both polarities for high arm voltages. This reduces current deficiencies. However, the Source Submodule AL1 is seen to be inserted almost whenever the arm current is negative. The same goes for the Load Submodule AL12 when the arm current is positive. Evidently, not only the Load Submodules, but also the Source Submodules are seen to struggle even though the conditions are favorable for discharging. The voltage balancing for higher number of Load Submodules might therefore fail because of the Source Submodules as well. Nevertheless, it is evident that no more Load Submodules can be present for an MMC operation within the KPI limits.

4.7.9 Summary of Cases

Through cases 1 to 8 the connectivity of the MMC has been investigated and assessed. Cases 1 and 6 investigated the rated MMC operation as a source and a load respectively. The arm currents were found to be determined based on the net MMC power flow and they were found to have only a fundamental frequency component during normal operation. This caused fundamental frequency oscillations in the submodule voltages. Case 2 to 5 investigated non-mixed power mismatches and the compensating methods were found to be successful. In addition, they were observed to have the following effects on the arm current related to the submodule balancing: (I) the DC component caused current offset deficiencies, (II) the fundamental frequency component reduced the arm current size causing current magnitude deficiencies, and (III) the second harmonic injections boosted the current and were found necessary for submodule imbalances.

In case 7 mixed arm power mismatches were found to be sustainable demonstrating that the success of the DER connectivity only depends on the success of the submodule balancing. The submodule balancing was then investigated in case 8. The maximum number of Load Submodules was found to be 3, constrained by the submodule voltage KPI. Additional inserted Load Submodules could not be balanced. The exact reason was hard to identify as several factors influenced the balancing. That being said, the most significant impact seemed to come from current magnitude deficiencies caused by the vertical balancing.

The KPIs from all the cases are shown in Table 4.3. In general, the KPIs showed that the MMC could handle all power mismatch cases except for some mixed intra-arm power flows investigated in case 8. The CUF is found to be the highest for horizontal imbalances as in case 2 with a value of 1.2 %, but is never the constraining limit, that is, the CUF is never the only limit that prevent the MMC for satisfying the KPIs. The

TRDs are found to increase slightly with higher power mismatches, but mostly to higher arm current magnitudes. The largest average TRD is therefore found in case 8 where the second harmonic injections were the highest. The TRDs are found to be similar when no components are injected, but varies more between each other for larger injections. Finally, the submodule voltage KPI for stable cases are found to correlate with the arm current magnitude and is, therefore, the highest in case 8. In short, the best performance is achieved if the submodules can be balanced with minimal arm currents.

	CUF [%]	TRD [%]			Submodule voltage region [%]
		a	*b*	*c*	
Case 1	0.03	0.79	0.85	0.80	11.9
Case 2	1.20	1.40	1.63	1.43	10.2
Case 3	0.18	1.57	1.57	1.68	11.7
Case 4	0.48	1.49	1.43	1.26	14.05
Case 5b	0.90	3.21	2.31	3.92	16.0
Case 6	0.08	0.73	0.76	0.81	12.0
Case 7	0.51	3.16	2.12	2.98	17.1
Case 8	0.62	2.92	2.73	3.92	21.2

Table 4.3: Summary of the case simulation results

From this summary some recommending guidelines can be formulated for EMSs of grid-connected DERs:

- The MMC can guarantee an acceptable operation, even for mixed arm power flows, as long as mixed intra-arm power flows are not present.
- Second harmonic injections are not needed if submodule power mismatches are not present.
- The best MMC performance is achieved if submodule balancing is done with minimized arm currents, that is, the least possible second harmonic injection.
- The submodule voltage KPI is the constraining limit, but is shortly followed by the TRD limits because of the second harmonic injections.
- Mixed intra-arm power flows should be avoided, but can be sustained for small power flows or only a few submodules at the cost of high second harmonic injections.

Chapter 5

Conclusions and Future Work

This chapter concludes the thesis by summarizing the modeling procedure and the main conclusions from the connectivity analysis of Chapter 4. In addition, it provides relevant research topics for the future development of a general EMS for grid-connected DERs.

5.1 Conclusions

In this thesis the necessary foundation for an EMS with grid-connected DERs has been made. Specifically, the thesis has been focused on finding the MMC's ability to support mixed power flows, that is, an MMC where there are both generating and consuming submodules simultaneously. The MMC was evaluated by investigating scenarios with different power mismatches. To simulate the scenarios an MMC has been modeled, its submodules have been designed for grid-connection of PV and BESS, and the possible submodule modes have been identified through the description of a general EMS.

5.1.1 MMC Modeling

The thesis started with the modeling of an MMC. The fundamental MMC features were described and an MMC state-space representation based on an arm averaged model was made. This representation was formulated using the Σ-Δ notation and relevant analytical tools for this notation were derived:

- The Σ and Δ variables represent the inner and outer dynamic of the MMC respectively. This enables the variables to be separated into two groups that can be interpreted as electrical circuits with driving voltages.

- The necessary arm current component in a balanced MMC without a DC-link is only an AC fundamental frequency component.
- A circular dependence exists between the harmonic content in the currents and their driving voltages.
- As long as only the necessary current components are present in the MMC, the Σ variables will only have even-ordered components while the Δ variables will only have odd-ordered components.

The possible power mismatches in the MMC and the compensating procedures to minimize them were described. The power imbalance types were defined: the phase imbalance, the arm imbalance and the submodule imbalance. The imbalances were found to be compensated by different circulating current components. A DC component was used to compensate the phase imbalance. A fundamental frequency component could compensate the arm imbalance, but it had to be found using symmetrical components. This was to make sure that the current components summed to zero. Three reasons for submodule balancing deficiencies were identified; the arm current could cause problems in the balancing if it had improper magnitude, DC offset or phase. A second harmonic component was found to mitigate these effects.

5.1.2 Submodule Modeling

The MMC submodule was designed to interface a PV array and a BESS. The necessary conditions for the submodule design were that it had to provide a galvanic isolation to the rest of the MMC and be able to control the power of the DERs. The BESS was modeled as a voltage source in series with a resistance. Polarization effects were included by varying the voltage source according to the SOC in the BESS. The parameters for the batteries was extracted using experimental equations fitted to a standard discharge curve. The power flow of the BESS was controlled with a bidirectional boost converter. A simple control loop with a PI block was made to force the BESS power references.

The PV array was modeled as a current source in parallel with a diode and a simple resistance network. The maximum power out of the arrays was set to be extracted by a P&O algorithm implemented in a DAB. The DAB was selected for its high controllability and galvanic isolation. The MPPT control and the resulting impact on the DAB was found through a steady-state state-space representation. This representation was made time-invariant by adding a phase-shifted virtual phase and expressing the converter in a synchronous reference frame. The DAB parameters were found by parametric sweeps of the winding inductance and resistance in the DAB transformer. The lower limit of the capacitor voltage in the DAB was found to be 46 V using similar sweeps of the DC-link voltage and current. The lower limit became the disconnection limit for the PV arrays during insufficient irradiances.

5.1.3 EMS Guidelines For Grid-Connected DERs

A general EMS for grid-connected PV arrays and BESSs was outlined. The EMS logic was separated into a battery energy management system (BEMS) and all the possible submodule modes were described. The BEMS structure was divided in three. The first part of the system implemented the desired services by computing the corresponding arm-aggregated power references for the BESSs. The next part was a BESS-distributing EMS (BDEMS) which could optimally distribute the arm-aggregated power reference between the submodules. Finally, the last part of the BEMS was a reference assessment system. This system evaluated the individual power references according to the BESS limits to make sure the references were acceptable. Some specific EMSs were also included. One EMS could compensate power mismatches in the MMC using the BESSs to reduce the necessary compensating currents. Another EMS was used for power smoothing of generated PV power for less fluctuating generation. In addition, two BDEMS was detailed which could equalize the BESS SOH or minimize the submodule imbalances.

Finally, the MMC connectivity using the existing compensation techniques was evaluated with different power mismatches scenarios. The scenarios were done in the system level by representing the submodules as power references. Only rated submodule power flows were used to limit-test the connectivity. The rated power flows were also simulated in the submodules to investigate the submodule operation. Without reducing the MPPT, a Source Submodule could be sustained as long as the PV power did not deviated from the power reference too long. A Disconnected or Load Submodule were found to be feasible only if the irradiance was low.

Three key performance indicators were formulated to evaluated the MMC performance:

- The current unbalance factor CUF. It is defined as the ratio between the negative and positive sequence components and is used to assess the grid current imbalance.
- The total rated-current distortion TRD. It is defined as the ratio between the grid current harmonic components and the rated grid current and is used to assess the total distortion in the grid current.
- The maximum submodule voltage regions. They are defined as the deviance from the rated capacitor value and is used to assess the balancing of the capacitor voltages.

The limits of the indicators were set to be 3 %, 5 % and ±15% respectively.

The results of the scenarios provided general guidelines for EMSs in MMCs used for grid-connected DERs. The compensation techniques for horizontal and vertical imbalances were found to compensate the power mismatches successfully. Any arm power mismatches in an MMC can therefore be sustained. Additionally, submodule power imbalances could also be sustained with the right second-ordered harmonic injection as long as the submodules of the arm did not have mixed intra-arm power flows, that is, as long as there did not exist both charging and discharging submodules in one arm. Moreover, the vertical and horizontal compensating currents were found to negatively impact the submodule balancing. Only 3 rated load submodules could be sustained for proper submodule voltage balancing.

5.2 Future Work

In this thesis research work has been presented which describes and investigates the consequences of grid-connected DERs with mixed power flows. The failing balancing algorithm for the capacitor voltages was found to prevent the MMC from safely interfacing DERs with mixed power flows. A better method to stabilize the submodule voltages is therefore needed. Or, if the second harmonic injections are to be used in future EMSs, the injections should be analyzed closer to provide necessary conditions for mixed power flows. In addition, an MMC model better suited for energy management analysis should be developed. These issues are addressed here.

5.2.1 Submodule Voltage Balancing

It has been identified through the analysis in this thesis that the submodule voltage regions are the constraining limits for acceptable operation of a MMC for grid-connected DERs with mixed power flows. This was because the maximum voltage regions was the first KPI that could not be withheld for the maximum mixed intra-arm power flow in Case 8. New ways to handle the submodule imbalances should therefore be the first objective for improving the MMC operation.

The easiest solution is to investigate if the submodule voltage regions can be expanded. In this thesis the region limits are set based on the operating limits at the rated conditions. However, an analysis should be conducted to examine what the highest acceptable limits are and the consequences of increasing them. Increased submodule voltages are likely to increase losses and instabilities.

A second solutions is to incorporate the existing submodule balancing capability into the EMS through power flow limits. This is one of the objectives that is proposed for the BDEMS in Chapter 4. It was found in this thesis that for an arm dominated by a certain power type, any combinations of 0.2 p.u. mixed power flows of the non-dominant power type is sustainable. A limit like this could be used to ensure submodule balancing. The limit is found experimentally in this thesis and an MMC analysis should be done to find such a limit analytically. Finding this limit would likely involve calculating the necessary injections for a given power mismatch and mixed power flow.

Calculation of the optimal size and phase of the second harmonic injection would also be necessary for maximizing converter efficiency. A sufficient condition for non-mixed power flows was given in Section 2.6. A similar condition, however, should be developed for mixed power flows as well. A prerequisite for calculating the necessary injections is to be able to estimate the arm currents for any imbalances. This can be achieved be a steady-state model capable of describing MMC power mismatches.

5.2.2 Steady-State Time-Invariant MMC Model

If methods that can guarantee submodule balancing for mixed power flows are developed, the next step should be to implement an MMC model more suited for energy management analysis. The model should have the possibility to simulate the MMC efficiently for longer durations such as minutes and hours in order to assess the dynamics related to the battery SOC in the submodules. Such a model could be a steady-state MMC model because the neglected transient dynamics would make the model fast to simulate. As mentioned, this will also make calculation of arm currents easier which is a prerequisite for calculating the necessary second harmonic injections.

A promising steady-state MMC model is the steady-state model by [22] which the modeling of the MMC in this thesis is based on. This model is even time-invariant which makes for even faster simulations. The method in [22] uses a Park transform of the Σ-Δ variables. As discussed, these variables only contain odd or even harmonics when the necessary components defined in Section 2.5 are produced. Reference [22] assumes that components higher than the third harmonics can be neglected. In addition, the DC and 3ω terms of the variables in [22] are assumed common for all three phases. The frequency components of the Σ and Δ variables can, therefore, be extracted using a Park transform of -2ω and ω respectively where the DC and 3ω terms are captured by the zero-sequence component.

However, the model is not fit for capturing the necessary current components for mitigating the power mismatches. This is because the horizontal balancing forces DC terms that are sized differently and the vertical balancing forces a new frequency component in the Σ variables. These components unable the dynamics to be captured using a single, time-invariant synchronous reference frame. Consequently, new ways to model steady-state time-invariant MMCs with power mismatches are needed.

Appendices

Appendix A

Direct-Quadrature-Zero Transform

The direct-quadrature-zero (DQZ) transform consists of two intermediate transformation steps: the Clarke transform and a rotational transform. The Clarke transform transforms the phases from the *abc* reference frame into the $\alpha\beta\gamma$ reference frame. The goal of the transform is to isolate the zero component γ of the phases, i.e. the common part, so that the remaining balanced three phases can be projected from the three dimensional sphere onto an $\alpha\beta$-plane. This plane let us formulate the three phases by the two stationary axes α and β as shown in Figure A.1a.

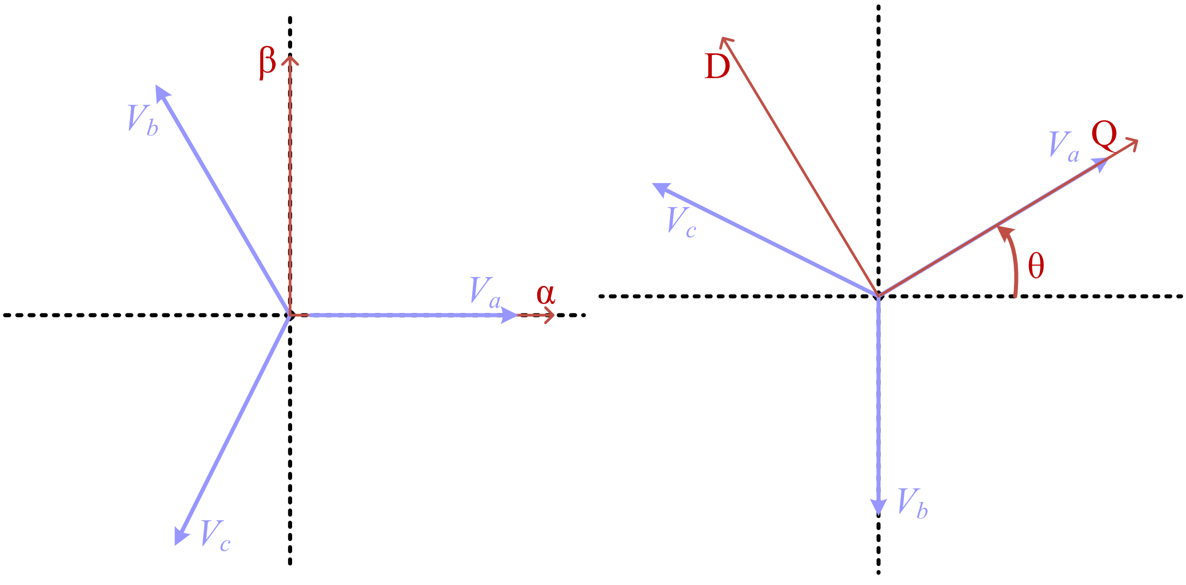

(a) Clarke Transformation

(b) Rotational Transformation

Figure A.1: DQZ transformation illustrated in two steps.

The rotational transform can then be applied to the new axes. The rotation is set to match the speed of the phases, removing the relative motion between the phase variables and the axes as shown in Figure A.1b. The final result of the total transform is therefore three constant values corresponding to the phasors of a three-phase system as shown for the balanced phasors in Figure A.2. The figure shows also the result of the intermediate Clarke transformation.

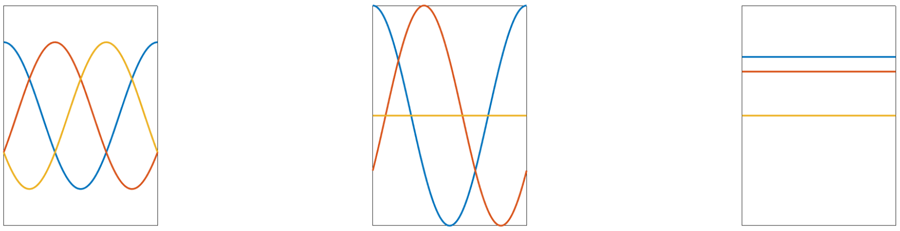

(a) abc-reference frame (b) $\alpha\beta\gamma$-reference frame (c) DQZ-reference frame

Figure A.2: DQZ transformation of a balanced three-phase system.

Appendix B

MATLAB Files

B.1 Battery Model Parameters

```
syms A E0 K Vfull Vexp Qexp Vnom Qnom Rb i Q
% Vfull= 3.8412; Vexp=3.5653; Qexp = 0.113; Vnom = 3.3; Qnom = 2.08; ...
    Rb=0.001435; i=1; Q=2.38;
Vfull= 3.8412; Vexp=3.5653; Qexp = 0.11693; Vnom = 3.3; Qnom = ...
    2.1523; Rb=0.013866; i=1.0348; Q=2.38;

B=3/Qexp;
eq1=Vfull-E0+i*Rb-A;
eq2=E0-K*Q*(Qexp+i)/(Q-Qexp)-Rb*i+A*exp(-3)-Vexp;   %Obs: added ...
    -i*Rb compared to spec. proj
eq3=(Q-Qnom)*(E0-Vnom-i*Rb+A*exp(-B*Qnom))/(Qnom*Q+i*Q)-K;

SOLV=solve(eq1,eq2,eq3,A,E0,K)
display(double(SOLV.A))
display(double(SOLV.E0))
display(double(SOLV.K))
```

B.2 Steady-State Equation for i^D

```
function out1 = idCalculate(Ir,L,R,iq,s1d,s1q,v1,v2,w)
%#codegen

%    This function was generated by the Symbolic Math Toolbox ...
    version 8.4.
%    09-Dec-2019 08:50:38

t2 = R.*iq;
```

```
t3 = s1q.*v1;
t4 = R.^2;
t5 = iq.^2;
t6 = s1d.^2;
t7 = v1.^2;
t8 = 1.0./L;
t9 = 1.0./R;
t10 = 1.0./w;
t11 = L.*s1d.*v1.*w;
t15 = Ir.*R.*v2.*8.0;
t12 = -t3;
t13 = R.*t3.*2.0;
t14 = t2.*t3.*4.0;
t16 = R.*t2.*2.0;
t17 = t6.*t7;
t18 = -t15;
t19 = t2.^2.*4.0;
t20 = t2+t12;
t21 = -t19;
t22 = t8.*t10.*t20;
t23 = t14+t17+t18+t21;
t24 = sqrt(t23);
t25 = L.*t24.*w;
out1 = [t22+(t8.*t9.*t10.*(t11+t13-t16+t25)) ...
    ./2.0;t22+(t8.*t9.*t10.*(t11+t13-t16-t25))./2.0];
end
```

B.3 Steady-State Equation for s_2^D

```
function out1 = s2dCalculate(Ir,L,R,iq,s1d,s1q,v1,v2,w)
%#codegen

%    This function was generated by the Symbolic Math Toolbox ...
    version 8.4.
%    09-Dec-2019 08:52:46

t2 = L.^2;
t3 = R.^2;
t4 = iq.^2;
t5 = s1d.^2;
t6 = v1.^2;
t7 = w.^2;
t8 = R.*s1q.*v1;
t9 = 1.0./L;
t10 = 1.0./v2;
t11 = 1.0./w;
t12 = L.*s1d.*v1.*w;
t16 = Ir.*R.*v2.*8.0;
t13 = iq.*t3;
t14 = t8.*2.0;
```

```
t15 = iq.*t8.*4.0;
t18 = -t8;
t19 = t5.*t6;
t20 = -t12;
t21 = -t16;
t22 = iq.*t2.*t7;
t23 = t3.*t4.*4.0;
t17 = t13.*2.0;
t24 = -t23;
t25 = t13+t18+t20+t22;
t29 = -t9.*t10.*t11.*(t8+t12-t13-t22);
t30 = t9.*t10.*t11.*(t8+t12-t13-t22);
t26 = t15+t19+t21+t24;
t27 = sqrt(t26);
t28 = L.*t27.*w;
out1 = [t30-(t9.*t10.*t11.*(t12+t14-t17+t28)) ...
    ./2.0;t30-(t9.*t10.*t11.*(t12+t14-t17-t28))./2.0];
```

B.4 Steady-State Equation for s_2^Q

```
function out1 = s2qCalculate(Ir,L,R,iq,s1d,s1q,v1,v2,w)
%#codegen

%    This function was generated by the Symbolic Math Toolbox ...
    version 8.4.
%    09-Dec-2019 08:52:59

t2 = R.^2;
t3 = iq.^2;
t4 = s1d.^2;
t5 = v1.^2;
t6 = 1.0./R;
t7 = 1.0./v2;
t8 = L.*s1d.*v1.*w;
t9 = R.*s1q.*v1.*2.0;
t10 = R.*iq.*s1q.*v1.*4.0;
t11 = Ir.*R.*v2.*8.0;
t12 = iq.*t2.*2.0;
t13 = t4.*t5;
t14 = -t11;
t15 = t2.*t3.*4.0;
t16 = -t15;
t17 = t10+t13+t14+t16;
t18 = sqrt(t17);
t19 = L.*t18.*w;
out1 = [(t6.*t7.*(t8+t9-t12+t19)) ./2.0;(t6.*t7.*(t8+t9-t12-t19))./2.0];
```

Appendix C

Simulink Models

C.1 Submodule System

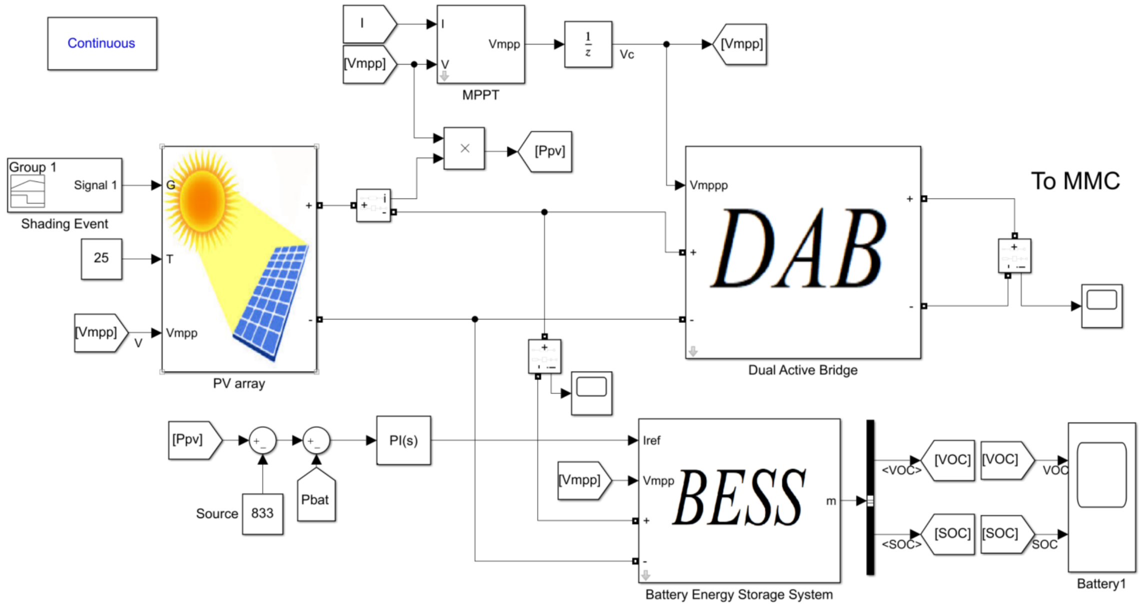

Figure C.1: Simulink model of the MMC submodule

C.2 BESS And Boost Subsystem

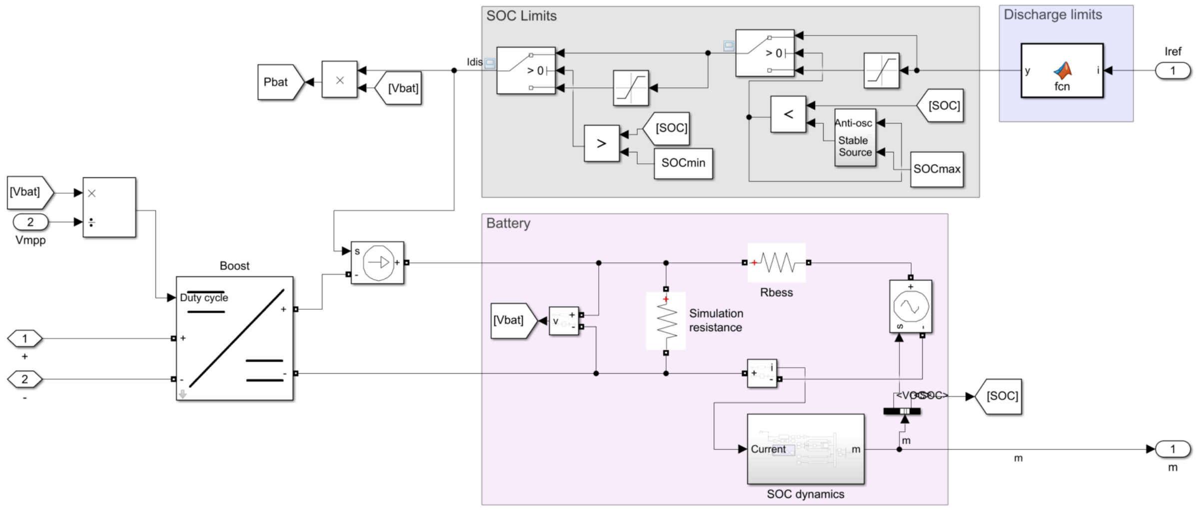

Figure C.2: Simulink model of BESS and boost subsystem

C.3 Dual Active Bridge

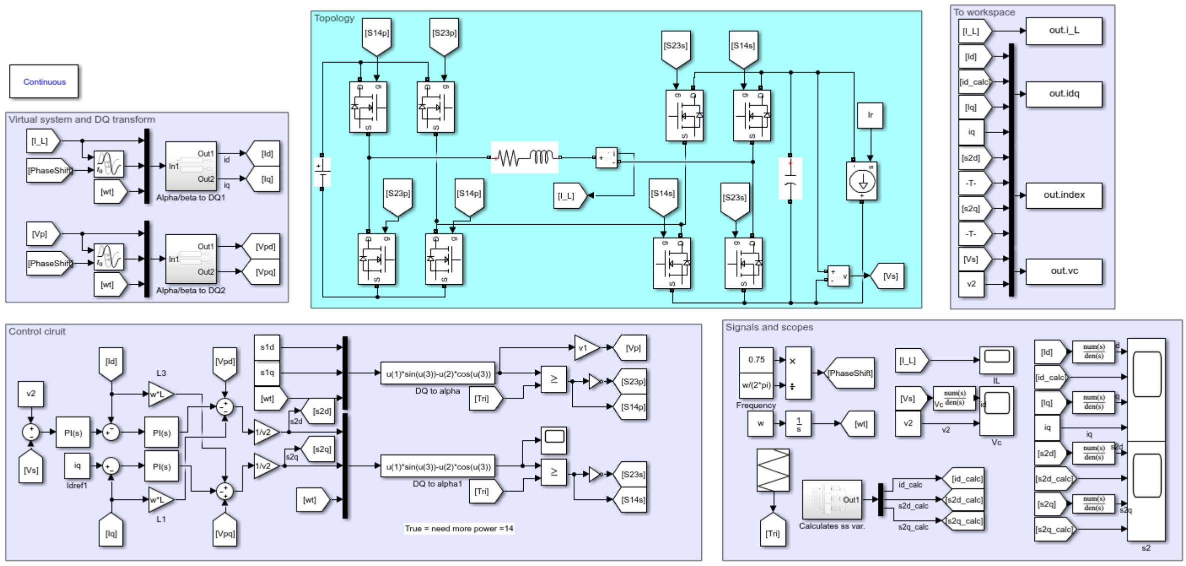

Figure C.3: Simulink model of the DAB converter.

Bibliography

[1] E. Viken, “Energy management of a modular multilevel converter module with pv and battery energy storage system,” Dec. 2019.

[2] “Renewables 2019 global status report,” tech. rep., REN21, Paris, 2019.

[3] A. Reinhold, *California Hourly Load vs load less solar and wind (Duck Curve) for October 22, 2016*. Oct 2016.

[4] J. Jana, H. Saha, and K. D. Bhattacharya, “A review of inverter topologies for single-phase grid-connected photovoltaic systems,” *Renewable and Sustainable Energy Reviews*, vol. 72, pp. 1256 – 1270, 2017.

[5] M. Rabiul Islam, A. M. Mahfuz-Ur-Rahman, K. M. Muttaqi, and D. Sutanto, “State-of-the-art of the medium-voltage power converter technologies for grid integration of solar photovoltaic power plants,” *IEEE Transactions on Energy Conversion*, vol. 34, no. 1, pp. 372–384, 2019.

[6] L. Zhang, Z. Zhang, J. Qin, D. Shi, and Z. Wang, “Design and performance evaluation of the modular multilevel converter (mmc)-based grid-tied pv-battery conversion system,” in *2018 IEEE Energy Conversion Congress and Exposition (ECCE)*, pp. 2649–2654, 2018.

[7] S. Lu, K. Sun, H. Shi, S. Jiang, and Y. W. Li, “Comparison of high power dc-dc converters for photovoltaic generation integrated into medium voltage dc grids,” in *2018 IEEE International Power Electronics and Application Conference and Exposition (PEAC)*, pp. 1–6, 2018.

[8] A. Marzoughi, R. Burgos, D. Boroyevich, and Y. Xue, “Investigation and comparison of cascaded h-bridge and modular multilevel converter topologies for medium-voltage drive application,” in *IECON 2014 - 40th Annual Conference of the IEEE Industrial Electronics Society*, pp. 1562–1568, 2014.

[9] F. Rong, X. Gong, and S. Huang, “A novel grid-connected pv system based on mmc to get the maximum power under partial shading conditions,” *IEEE Transactions on Power Electronics*, vol. 32, no. 6, pp. 4320–4333, 2017.

[10] R. Mishra and V. Agarwal, "Novel voltage balancing techniques for modular multilevel pv inverters," in *2018 IEEE Industry Applications Society Annual Meeting (IAS)*, pp. 1–8, 2018.

[11] S. Rivera, B. Wu, R. Lizana, S. Kouro, M. Perez, and J. Rodriguez, "Modular multilevel converter for large-scale multistring photovoltaic energy conversion system," in *2013 IEEE Energy Conversion Congress and Exposition*, pp. 1941–1946, 2013.

[12] T. Soong and P. W. Lehn, "Internal power flow of a modular multilevel converter with distributed energy resources," *IEEE Journal of Emerging and Selected Topics in Power Electronics*, vol. 2, no. 4, pp. 1127–1138, 2014.

[13] H. Bayat and A. Yazdani, "A power mismatch elimination strategy for an mmc-based photovoltaic system," *IEEE Transactions on Energy Conversion*, vol. 33, no. 3, pp. 1519–1528, 2018.

[14] U. Sohail, H. Nademi, and L. E. Norum, "A reliable modular based pv-battery hybrid system with peak shaving capability," in *2018 IEEE 19th Workshop on Control and Modeling for Power Electronics (COMPEL)*, pp. 1–6, 2018.

[15] H. Bayat and A. Yazdani, "A hybrid mmc-based photovoltaic and battery energy storage system," *IEEE Power and Energy Technology Systems Journal*, vol. 6, no. 1, pp. 32–40, 2019.

[16] G. Guidi, S. D'Arco, J. A. Suul, R. Iso, and J. Itoh, "A modular multilevel interface for transformerless grid integration of large-scale infrastructure for wireless electric vehicle charging," in *2019 10th International Conference on Power Electronics and ECCE Asia (ICPE 2019 - ECCE Asia)*, pp. 2059–2066, 2019.

[17] A. Lesnicar and R. Marquardt, "An innovative modular multilevel converter topology suitable for a wide power range," in *2003 IEEE Bologna Power Tech Conference Proceedings,*, vol. 3, pp. 6 pp. Vol.3–, June 2003.

[18] S. Debnath, J. Qin, B. Bahrani, M. Saeedifard, and P. Barbosa, "Operation, control, and applications of the modular multilevel converter: A review," *IEEE Transactions on Power Electronics*, vol. 30, no. 1, pp. 37–53, 2015.

[19] H. Akagi, "Classification, terminology, and application of the modular multilevel cascade converter (mmcc)," in *The 2010 International Power Electronics Conference - ECCE ASIA -*, pp. 508–515, June 2010.

[20] Q. Tu, Z. Xu, and L. Xu, "Reduced switching-frequency modulation and circulating current suppression for modular multilevel converters," *IEEE Transactions on Power Delivery*, vol. 26, pp. 2009–2017, July 2011.

[21] G. Bergna Diaz, J. A. Suul, and S. D'Arco, "Small-signal state-space modeling of modular multilevel converters for system stability analysis," in *2015 IEEE Energy Conversion Congress and Exposition (ECCE)*, pp. 5822–5829, 2015.

[22] G. Bergna-Diaz, J. Freytes, X. Guillaud, S. D'Arco, and J. A. Suul, "Generalized voltage-based state-space modeling of modular multilevel converters with constant equilibrium in steady state," *IEEE Journal of Emerging and Selected Topics in Power Electronics*, vol. 6, no. 2, pp. 707–725, 2018.

[23] K. Ilves, A. Antonopoulos, S. Norrga, and H. Nee, "A new modulation method for the modular multilevel converter allowing fundamental switching frequency," *IEEE Transactions on Power Electronics*, vol. 27, pp. 3482–3494, Aug 2012.

[24] D. Wu and L. Peng, "Analysis and suppressing method for the output voltage harmonics of modular multilevel converter," *IEEE Transactions on Power Electronics*, vol. 31, pp. 4755–4765, July 2016.

[25] F. Zhao, G. Xiao, and T. Zhao, "Accurate steady-state mathematical models of arm and line harmonic characteristics for modular multilevel converter," *IEEE Transactions on Power Delivery*, vol. 33, pp. 1308–1318, June 2018.

[26] A. Antonopoulos, L. Angquist, and H. Nee, "On dynamics and voltage control of the modular multilevel converter," in *2009 13th European Conference on Power Electronics and Applications*, pp. 1–10, Sep. 2009.

[27] Q. Song, W. Liu, X. Li, H. Rao, S. Xu, and L. Li, "A steady-state analysis method for a modular multilevel converter," *IEEE Transactions on Power Electronics*, vol. 28, pp. 3702–3713, Aug 2013.

[28] J. Peralta, H. Saad, S. Dennetiere, J. Mahseredjian, and S. Nguefeu, "Detailed and averaged models for a 401-level mmc–hvdc system," *IEEE Transactions on Power Delivery*, vol. 27, no. 3, pp. 1501–1508, 2012.

[29] Z. Salam, K. Ishaque, and H. Taheri, "An improved two-diode photovoltaic (pv) model for pv system," in *2010 Joint International Conference on Power Electronics, Drives and Energy Systems 2010 Power India*, pp. 1–5, Dec 2010.

[30] J. A. Gow and C. D. Manning, "Development of a photovoltaic array model for use in power-electronics simulation studies," *IEE Proceedings - Electric Power Applications*, vol. 146, pp. 193–200, March 1999.

[31] N. M. A. Alrahim Shannan, N. Z. Yahaya, and B. Singh, "Single-diode model and two-diode model of pv modules: A comparison," in *2013 IEEE International Conference on Control System, Computing and Engineering*, pp. 210–214, Nov 2013.

[32] M. Chen and G. A. Rincon-Mora, "Accurate electrical battery model capable of predicting runtime and i-v performance," *IEEE Transactions on Energy Conversion*, vol. 21, pp. 504–511, June 2006.

[33] D. W. Dees, V. S. Battaglia, and A. Bélanger, "Electrochemical modeling of lithium polymer batteries," *Journal of Power Sources*, vol. 110, no. 2, pp. 310 – 320, 2002.

[34] "Generic battery model - Simulink - MathWorks Nordic."

[35] O. Tremblay and L.-A. Dessaint, “Experimental Validation of a Battery Dynamic Model for EV Applications,” *World Electric Vehicle Journal*, vol. 3, pp. 289–298, June 2009.

[36] H. Ahmed and A. Bhattacharya, “Pmsg based constant power delivery standalone wecs using sst with bidirectional buck-boost bess,” in *2016 IEEE 7th Power India International Conference (PIICON)*, pp. 1–6, Nov 2016.

[37] K.-H. Chao, M.-C. Tseng, C.-H. Huang, Y.-G. Liu, and L.-C. Huang, “Design and Implementation of a Bidirectional DC-DC Converter for Stand-Alone Photovoltaic Systems,” *International Journal of Computer, Consumer and Control (IJ3C)*, vol. 2, p. 12, 2013.

[38] N. Mohan, *Power electronics: a first course.* Wiley, 2012.

[39] P. S. Khalane, D. A. Patil, and C. Remadevi, “Literature survey of various maximum power point tracking techniques for photovoltaic systems,” in *2017 International Conference on Intelligent Computing, Instrumentation and Control Technologies (ICICICT)*, pp. 836–840, 2017.

[40] S. Electronics, *Poly-crystalline silicon photovoltaic roof module with 62 W maximum power.* ND-62RU1, 2005.

[41] M. T. Lawder, B. Suthar, P. W. C. Northrop, S. De, C. M. Hoff, O. Leitermann, M. L. Crow, S. Santhanagopalan, and V. R. Subramanian, “Battery energy storage system (bess) and battery management system (bms) for grid-scale applications,” *Proceedings of the IEEE*, vol. 102, no. 6, pp. 1014–1030, 2014.

[42] F. Gao, L. Zhang, Q. Zhou, M. Chen, T. Xu, and S. Hu, “State-of-charge balancing control strategy of battery energy storage system based on modular multilevel converter,” in *2014 IEEE Energy Conversion Congress and Exposition (ECCE)*, pp. 2567–2574, 2014.

[43] N. Li, F. Gao, T. Hao, Z. Ma, and C. Zhang, “Soh balancing control method for the mmc battery energy storage system,” *IEEE Transactions on Industrial Electronics*, vol. 65, no. 8, pp. 6581–6591, 2018.

[44] H. Arghavani and M. Peyravi, “Unbalanced current-based tariff,” *CIRED - Open Access Proceedings Journal*, vol. 2017, no. 1, pp. 883–887, 2017.

[45] T. C. of European Energy Regulations (CEER), “6th ceer benchmarking report on the quality of elictricity and gas supply,” vol. 6, 2016.

[46] G. Chicco, F. Corona, R. Porumb, and F. Spertino, “Experimental indicators of current unbalance in building-integrated photovoltaic systems,” *IEEE Journal of Photovoltaics*, vol. 4, no. 3, pp. 924–934, 2014.

[47] S. Vlahinic, D. Brnobic, and N. Stojkovic, “Indices for harmonic distortion monitoring of power distribution systems,” in *2008 IEEE Instrumentation and Measurement Technology Conference*, pp. 421–425, 2008.

[48] "Ieee standard for interconnection and interoperability of distributed energy resources with associated electric power systems interfaces," 2018.

[49] Z. Ma, F. Gao, X. Gu, N. Li, and D. Niu, "An online soh testing method of mmc battery energy storage system," in *2018 IEEE 19th Workshop on Control and Modeling for Power Electronics (COMPEL)*, pp. 1–7, 2018.

Egil Viken

Towards Energy Management of an MMC With PV and BESS

NTNU
Norwegian University of
Science and Technology